Magnetic anisotropy and coercivity of tetragonally distorted spinel ferrite particles via the Jahn-Teller distortion and magnetoelastic coupling

HAWA ALIMA BINTI ABDUL LATIFF

February 2019

Magnetic anisotropy and coercivity of tetragonally distorted
spinel ferrite particles via the Jahn-Teller distortion and
magnetoelastic coupling

HAWA ALIMA BINTI ABDUL LATIFF
Doctoral Program in Applied Physics

Submitted to the Graduate School of
Pure and Applied Sciences
in Partial Fulfillment of the Requirements
for the Degree of Doctor of Philosophy in
Engineering

at the
University of Tsukuba

ACKNOWLEDGMENTS

ABSTRACT

This thesis concerned a study of tetragonal ferrites for their potential use as magnets. To this end, we synthesized tetragonally distorted (Cu,Co)-ferrite particles and systematically characterized their structural and magnetic properties. The intrinsic and extrinsic factors contributing to coercivity were investigated. We demonstrated a coupling of the Jahn-Teller (JT) effect and the magnetoelastic (ME) effect, using a phenomenological approach. From the magnetoelastic model analysis, we demonstrated a linear dependence of the magnetic anisotropy using the tetragonality parameter obtained from the JT distortion. The magnetoelastic coefficient values for Cu (B_{1Cu} = 1.5 MJ/m^3) and Co (B_{1Co} = 40 MJ/m^3) deduced from our experimental data were in relatively good agreement with the value calculated for bulk copper ferrite ($B_{1Cu\ bulk}$= 4 MJ/m^3) and cobalt ferrite ($B_{1Co\ bulk}$= 55 MJ/m^3). These results suggest that the source of magnetic anisotropy can be attributed to the coupling of the JT distortion with the magnetoelastic effect of Co. Instead of a continual increase with the Co content x, the magnetic anisotropy K_u tends to reach a saturation value due to competition between the magnetoelastic effect of Co and the JT effect of Cu. Comparing tetragonal and cubic samples, the intrinsic magnetic anisotropy constant K_u varies less than the coercivity and the anisotropy fields. The reduction of the anisotropy field above x = 0.1 is attributed to an increase in the spontaneous magnetization. We also analyzed the coercivity of representative samples within the framework of the micro-magnetic and global models of coercivity. While linear fits of the temperature dependence of magnetic properties were achieved within the micro-magnetic model, a divergence is found in the low temperature data analyzed within the global model. This is tentatively attributed to thermal activation mediated by exchange-coupling between neighboring grains.

CONTENTS

1. General introduction

This thesis deals with the preparation and study of tetragonal spinel ferrites, which could potentially be used as permanent magnets (PM). The development of high-performance rare-earth transition metal (RE-TM) permanent magnets has enabled the advancement of modern technology requiring powerful magnets (e.g. hybrid electric vehicles, wind turbines...). For applications which require less powerful magnets (e.g. motors of hand-held tools and domestic appliances), ferrite magnets are particularly interesting due to the low cost and high abundance of the raw materials relative to RE-TM magnets. In the early 1930s, Kato and Takei invented the so-called O.P. magnets (oxide permanent magnet /Ookayama permanent magnet) based on cobalt-iron spinel ferrites which exhibit remarkable magnetic properties through magnetic annealing. Later, anisotropic hexagonal ferrites (Ba-ferrite and Sr-ferrite) with superior magnetic properties were developed, and they are today's most commonly used PM materials. In general, hexagonal ferrites exhibit relatively high magnetocrystalline anisotropy compared to cubic spinel ferrites, which are highly symmetrical. In this thesis, we propose that spinel ferrites can also be of major interest as PM materials if they can be fabricated to have a distorted crystal structure, using an up-scalable production technique.

While coercivity is one of the most crucial properties of PM materials, it is also one of the most difficult properties to optimize due to a complex relation between intrinsic and extrinsic factors. The extrinsic factors contributing to coercivity include lattice defects and grain shape, the latter of which would affect dipolar interactions. The intrinsic property related to coercivity is the magnetocrystalline anisotropy, due to spin-orbit interactions or LS coupling. Although most $3d$ atoms including those in the spinel ferrites have relatively weak spin-orbit interactions, high magnetic anisotropy may be realized by reducing the lattice symmetry, as explained within the phenomenological magnetoelastic model [1][2]. Niizeki et al. demonstrated extraordinarily large perpendicular magnetic anisotropy (PMA) in epitaxially strained cobalt ferrite (CFO) thin films with an estimated K_u value of 1.5 MJ/m^3, measured using the torque method [3]. Further analyses attributed the large PMA of the epitaxial CFO thin films to the high magnetostriction constant of cobalt ferrites and to the epitaxial strain induced by the lattice mismatch between the substrate and the thin film [4][5]. The anisotropy field reported by Niizeki was 5 T, which is comparable to that of the Nd$_2$Fe$_{14}$B phase (7 T), suggesting that tetragonally distorted spinel ferrites may be a possible candidate for permanent magnet materials. For these so-called tetragonal ferrites to be used in bulk magnets, they must be mass-producible. To achieve this, the control of lattice distortion and magnetoelastic coupling in powders is crucial since epitaxial strain can only apply to thin films. This brings us to the main motivation of this thesis, which is to establish a method of coupling lattice strain with the magnetoelastic effect in cobalt ferrite particles.

Lattice distortion can be introduced to nanoparticles either externally by applying tensile/compressive strains, or internally by spontaneous lattice distortion. The former would involve applying large stress (force) on bulk materials. Since the magnetoelastic model was predicted with the assumption of very small strain, internal lattice distortion is preferable. An example of spontaneous lattice strain is the Jahn-Teller (JT) effect, which refers to the spontaneous distortion which occurs in a system with a single electron in a degenerate level (nonlinear molecular system). The act of reducing the crystal symmetry helps to lower the overall energy of the system. Among the $3d$ cations, this effect is particularly strong for the $3d^4$ and the $3d^9$ (Mn^{3+} and Cu^{2+}) ions in the octahedral symmetry. To simplify the problem of valency control in the spinel structure, we focus on the JT effect of stable divalent Cu^{2+}. By incorporating the JT ion (Cu^{2+}) into the spinel ferrite, we aim to induce lattice strain and to control the magnetic anisotropy via magnetoelastic coupling with Co^{2+} of the tetragonally distorted structure.

For a cubic lattice, the magnetostrictive (stress) anisotropy energy K^{ms} is expressed as $K^{ms} = -\frac{3}{2}\lambda_s \sigma_{ij}$, where λ_s is the saturation magnetostriction constant, and σ_{ij} is the stress tensor, which can be expressed in terms of the elastic modulus C and strain ε_{ij} as $\sigma_{ij} = C\varepsilon_{ij}$ [6]. Since stress and strain are second rank tensors, it can be complicated to solve for K^{ms} due to the non-linear terms. To solve this problem, one assumes sufficiently small and single-dimensional strain to linearize the equation, such as that applied for the epitaxial strain [1].

In epitaxial CFO thin films, Tainosho et al. applied the phenomenological magnetoelastic theory to model the large PMA with respect to the magnitude of lattice strain, using the expression $K_u = B_1 \chi$, where K_u is the uniaxial magnetic anisotropy energy determined from torque measurements and B_1 is the magnetoelastic coupling coefficient, expressed using the magnetostriction constant λ_{100} and elastic moduli C_{ij} as [4] $B_1 = -\frac{3}{2}\lambda_{100}(C_{11} - C_{12})$. The tetragonality is represented as χ, which is defined by the lattice parameters c and a as, $\chi = c/a - 1$. Since the JT distortion is a one-dimensional distortion involving the extension/distortion of the c-axis, we attempt to apply the same magnetoelastic model to obtain large magnetic anisotropy in tetragonally distorted ferrite particles.

From a fundamental standpoint, this study seeks to demonstrate a model which couples the two independent physical phenomena. The results will also allow a re-evaluation of spinel ferrites as PM materials, since the original development of O.P. magnets. To realize the idea of the so-called tetragonal ferrite magnets, this study is divided into two main parts, focusing on investigating the intrinsic property (magnetic anisotropy) and the extrinsic property (coercivity) of the material. First, we demonstrate a model of the Jahn-Teller (JT) effect and the magnetoelastic (ME) coupling in tetragonally distorted (Cu,Co)-ferrite particles. Then, we performed coercivity analysis within two models [7][8] of coercivity on two representative samples. As we will see in the following seven chapters, the combination of two physical phenomena – the Jahn-teller effect coupled with the magnetoelastic effect – may induce a high magnetic anisotropy due to the spontaneous lattice distortion and the magnetoelasticity of the material. The in-depth study of tetragonal spinel ferrite particles will be presented in this thesis as follows:

This first chapter introduced the general context of this thesis. The background, motivation, approach and objectives of this thesis were introduced, followed by the structure of this thesis manuscript.

The theoretical background to the study and state-of-art are described in Chapter 2. The characteristics of spinel ferrites are presented. Then, physical descriptions of magnetic anisotropy, the JT and magnetoelastic effects are described. The state-of-art regarding cobalt-iron spinel ferrite is briefly reviewed.

Coercivity is introduced in Chapter 3. The classical coherent rotation model is explained; and more importantly, why real materials do not follow coherent rotation. The models used to characterize coercivity in real materials are described and the premises that sustain them are given.

Particle synthesis and other experimental techniques used in the context of this work are presented in Chapter 4. The principles of basic structural analysis techniques and magnetic measurements are recalled. Detailed descriptions of specialized analysis including Mössbauer spectroscopy and rotational hysteresis loss are given. The protocols used for coercivity analysis are described.

Chapter 5 is concerned with the basic characterization of (Cu,Co)-ferrite particles prepared via the coprecipitation and flux methods. First, the annealing temperature was optimized to produce tetragonal $CuFe_2O_4$. Then the Co and Cu contents were varied simultaneously, and the structural and magnetic properties were systematically investigated.

Chapter 6 is concerned with the analysis of magnetoelastic anisotropy in tetragonally distorted particles. An important aspect has been to try to express the JT effect of Cu^{2+} with Co^{2+} within the phenomenological understanding of the magnetoelastic model. To do this, the magnetic anisotropy (MA) energy was first analyzed by using torque measurements. Then the MA energy is related to the expression of JT distortion and ME effect.

Chapter 7 focuses on coercivity analysis of tetragonally distorted particles and non-distorted particles. An important aspect has been to try to understand the meaning of the values of the parameters and their implications on the physics of the reversal mechanism. The temperature dependent coercivity was analyzed within two general models of coercivity; the micromagnetic model which relates coercivity directly to the anisotropy field, and (ii) the global model in which coercivity is related to the activation volume of a single magnetization reversal process due to thermal activation.

The main results of this work are recalled in the final chapter. New directions of research are suggested to progress further in the understanding of the proposed tetragonal spinel ferrite as hard magnetic materials.

2. Theoretical background and State-of-the-Art

This chapter reviews the theoretical background and state-of-the-art regarding the proposed cobalt-based tetragonally distorted spinel ferrites. First, the main characteristics of spinel ferrites including the crystal structure and their magnetism are presented. Next, the state-of-the-art regarding cobalt-iron spinel-based hard ferrites are reviewed, focusing on the origin of magnetic anisotropy described within the one-ion model and within the theory of directional ordering. As described in the previous chapter, the aim is to exploit the Jahn-Teller effect to introduce tetragonal distortion in the cobalt-based spinel ferrites. In section 2.3, the Jahn-Teller effect induced by Cu^{2+} ions in tetragonal copper ferrites is reviewed, focusing on the physical description and the origin of the JT distortion. By introducing tetragonal distortion in cobalt ferrite, the final aim is to induce magnetic anisotropy via coupling of the JT effect and the magnetoelastic effect. In the final section, a physical description of magnetostriction is presented and the magnetoelastic anisotropy of tetragonal cobalt ferrite thin films is reviewed.

2.1. General description of spinel ferrites

The crystal structures of spinel ferrites including cobalt ferrites and copper ferrites are represented by the general formula $M^{2+}Fe^{3+}_2O_4$, (M^{2+} = Mn, Fe, Co, Ni, Cu, Mg, etc.). There are two kinds of interstitial sites occupied by the M^{2+} and Fe^{3+} cations; the $8a$ or A site is surrounded tetrahedrally by four O^{2-} ions; the $16d$ or B site is surrounded octahedrally by six O^{2-} ions. The crystal structure, shown in **Fig. 2.1**, is that of the highly symmetrical face-centered cubic lattice. A single unit cell contains a total of 56 ions, consisting of 32 O^{2-} ions, 8 cations in the tetrahedral A sites and 16 cations in the octahedral B sites. In order to minimize the electrostatic energy, the M^{2+} and Fe^{3+} cations will occupy the A and B sites in certain configurations so that the net electrical charge, summation of the cations and the O^{2-} ions is zero. Given that the A and B sites are written as (A)[B], the two main configurations of the spinel ferrites are

Normal spinel: $(M^{2+})_A[Fe^{3+}, Fe^{3+}]_BO_4$

Inverse spinel: $(Fe^{3+})_A[M^{2+}, Fe^{3+}]_BO_4.$
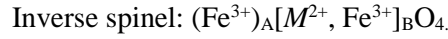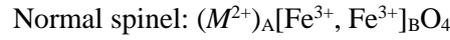
Except for zinc and manganese ferrites, most spinel ferrites crystalize in the inverse spinel configuration. Zinc ferrites crystallize in the normal spinel configuration, whereas Mn ferrites are 80% normal; meaning that 80% of Mn resides in the A sites while the other 20% occupy the B sites. Depending on the preparation methods and routes, inverse spinel ferrites other than Mn ferrites may also include a mixture of the normal and inverse spinel.

The magnetism of spinel ferrite is categorized as that of uncompensated antiferromagnetism. Consider the kind of superexchange interactions expected in this crystal structure. In general, the angle A-O-B is closer to 180° than the angles B-O-B or A-O-A. Therefore, one can expect the AB pair to have a stronger negative interaction than the AA or BB pairs. This negative superexchange interaction between the cations in the A and B sites results in a spontaneous magnetization. Néel proposed the arrangement of magnetic cations in inverse spinel ferrites using the model of colinear spins [9]. Considering this model, the cations in the A and B sites can be expressed as having the following magnetic arrangement:

$$(Fe^{3+}) \downarrow [M^{2+}Fe^{3+}] \uparrow O_4^{2-}$$
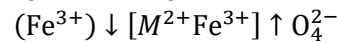
Since most spinel ferrites have the inverse spinel structure, the magnetic moments of Fe^{3+} ions in the A sites couple antiparallel to those of Fe^{3+} and M^{2+} in the B sites. Therefore, only the magnetic moments of M^{2+} ions contribute to the net spontaneous magnetization. From an experimental standpoint, Gorter has demonstrated the variation of saturation magnetization of spinel ferrites by varying the concentration of M^{2+} and Fe^{3+} cations in various M^{2+} doped spinel ferrites [10].

Consider the case of cobalt ferrite with a fully inverse spinel configuration. The formula unit is

$$(Fe^{3+}) \downarrow [Co^{2+}Fe^{3+}] \uparrow O_4^{2-}$$
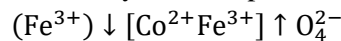
The magnetic moments for Fe^{3+} and Co^{2+} ions are 5 μ_B and 3 μ_B, respectively. From these values, the theoretical magnetic moment per formula unit of cobalt ferrite can be calculated as follows,

$$M = \{(3 + 5) - 5\} = 3\,\mu_B$$

Experimentally, the measured value of M of cobalt ferrites have been reported to be approximately 3.3 μ_B [11]. The deviation is attributed to the unquenched orbital moment of Co^{2+} ion caused by the trigonal crystalline field which causes cobalt ferrite to have large magnetocrystalline anisotropy (see Section 2.2.2). Furthermore, experimental results also suggest that cobalt ferrite is neither fully normal spinel nor fully inverse spinel as the Co^{2+} ions may be distributed among both the A sites and the B sites [12][13]. Moreover, Yafet and Kittel proposed that the directions of the magnetic moments in A and B sites may be canted [14], as opposed to being completely antiparallel as proposed by Néel. One way to investigate the canting of spins in A and B sites is by performing in-field Mössbauer spectroscopy. Specific details regarding Mössbauer experiments will be discussed in Section 4.4.
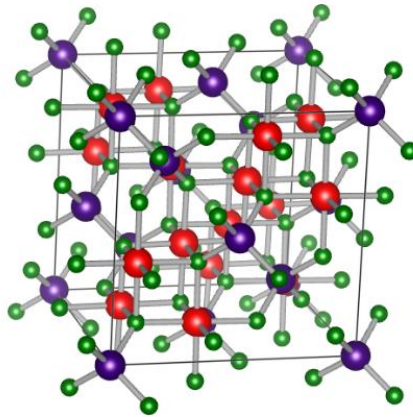
Fig. 2.1 Crystal structure of a typical inverse spinel ferrite. The red spheres represent cations in the B sites, blue represent cations in the A sites, and green represent oxygen ions.

2.2. Cobalt-iron spinel-based hard ferrites

Cobalt ferrites and/or cobalt-iron spinel ferrites have long been focused on for their hard-magnetic properties. One of the reasons is their large magnetocrystalline anisotropy. Another reason is due to the magnetoelastic properties of cobalt ferrite which enables directional ordering of octahedral Co^{2+} in response to thermal and/or mechanical stress. The former is referred to as the intrinsic anisotropy, whereas the latter corresponds to the extrinsic/induced anisotropy. In this section, we will first present the phenomenology of magnetocrystalline anisotropy. Then, we will review the mechanisms of both the intrinsic and extrinsic mechanisms of magnetic anisotropy in cobalt-based spinel ferrites.

2.2.1. Phenomenology of magnetocrystalline anisotropy

The magnetic anisotropy energy density governs the directional dependence of certain magnetic properties. There are several kinds of anisotropy: e.g. shape anisotropy, magnetocrystalline anisotropy, and magnetoelastic anisotropy. The magnetization vector (**M**) will lie along the crystallographic easy axis unless a torque due to shape, strain, field etc. is applied to **M** to move it from that direction.

Magnetocrystalline anisotropy refers to the magnetic anisotropy energy term which has the same symmetry as the crystal structure of the material [6][15], and the energy term E_a may be expressed as a function of the cosine directions of the magnetization vector **M**, with respect to the crystallographic axes (α_1, α_2, α_3). The magnetocrystalline anisotropy can be thought of as a torque which tends to align the magnetization along a certain direction within the crystal. In a single crystal magnetic material, the preferred direction for magnetization is called the easy axis. For a polycrystalline sample in which all constituent grains are randomly oriented, the individual anisotropies may be averaged over the entire sample so that the system as a whole will not exhibit any crystal anisotropy. In some polycrystalline bodies, the crystals have a preferred orientation,

called texture. In such a case, the aggregate body will have an anisotropy subject to the dominant crystalline orientation.

In the case of a uniaxial easy axis, the associated anisotropy energy density can be expressed in a series of powers of $\sin^2\theta$ and approximated to the first order as

$$E_a = K_1 sin^2\theta$$

(2.1)

where K_1 is the uniaxial anisotropy constant and θ is the angle between the magnetization direction and the crystallographic easy axis.

For crystals with cubic symmetry, such as spinel ferrites, the associated magnetocrystalline anisotropy energy density E_a, is given by

$$E_a = K_0 + K_1(\alpha_1^2\alpha_2^2 + \alpha_2^2\alpha_3^2 + \alpha_3^2\alpha_1^2) + K_2\alpha_1^2\alpha_1^2\alpha_1^2 + \cdots$$

(2.2)

where K_1, K_2, … are the magnetic anisotropy energy constants and (α_1, α_2, α_3) are the cosine directions between the magnetization vector and the crystallographic cubic axes.

The anisotropy constant K_1 for several types of spinel ferrites are summarized in **Table 2.1**. One sees that only the K_1 value for the cobalt ferrite has a positive value. This positive K_1 in cobalt ferrite is said to originate from the octahedral Co^{2+} and it can be explained using the one-ion model.

Table 2.1 K_1 of several spinel ferrites at room temperature (cubic symmetry)

Substance	K_1 (kJ/m^3)	References
$Mn_{0.98}Fe_{1.86}O_4$	-2.8	[16]
Fe_3O_4	-11	[17]
$Co_{1.01}Fe_2O_{3.62}$	$+200$	[18]

2.2.2. One-ion model anisotropy

In ferrimagnetic oxides such as the spinel ferrites, the magnetic atoms in the two interstitial A and B sites are separated by large negative ions. The one-ion model explains the mechanism of magnetocrystalline anisotropy from the behavior of the non-spherical magnetic atoms in the crystalline field produced by the surrounding ions. The one-ion model for cobalt substituted magnetite was explained by Slonczewski [19] . Consider cobalt ferrites which have the composition $Co^{2+}Fe^{3+}_2O_4$. For simplicity, we assume a fully inverse spinel configuration, where one Fe^{3+} occupies the tetrahedral site, while the other Fe^{3+} ions and the Co^{2+} ions occupy two octahedral sites. Although, strictly speaking, the site occupation for Fe^{3+} and Co^{2+} ions vary with the synthesis processes [12][13] .

The schematic diagram of the splitting of the energy levels by crystal fields is shown in **Fig. 2.2**; in the free ion state, a cubic crystal field; and a trigonal crystal field. Each Co^{2+} ion has 7 d-electrons (d^7), and the energy levels of the d-electrons which are fully degenerate in the free ion state are split into doubly degenerate dγ levels and triply degenerate dε levels in a cubic crystal field. In a trigonal crystal field, the second nearest neighbor metal ions surrounding an octahedral site are arranged symmetrically about the trigonal axis, which causes the three dε states to recombine to form three new orbitals compatible with trigonal symmetry. Consequently, the triply degenerate dε levels are split into an isolated lower single level, which corresponds to the wave function being concentrated along the trigonal axis and the doubly degenerate higher levels which correspond to the wave functions stretching perpendicular to the trigonal axis. According to Hund's rule, 5 out of the 7 electrons will fill up the (+) spin levels, while the remaining 2 electrons occupy the (−) spin levels . The last electron which occupies the doubly degenerate levels can alternate between the two possible wave functions, thus producing a circulating orbit. This orbital magnetic moment, L interacts with the total spin, S of Co^{2+}.

Such spin orbit coupling is expressed as

$$w = \lambda L \cdot S.$$

5

Since the number of electrons in a Co^{2+} ion is more than half the number required for a filled shell, L is parallel to S, and $\lambda < 0$. When S has a positive component parallel to the trigonal axis, L points in the $+$ direction of this axis. When S is rotated so that it has a negative component, L is reversed. In this case, the interaction energy is given by

$$w = \lambda LS|\cos\theta|.$$

In general, there are four <111> axes in cubic crystals. If Co^{2+} ions are distributed equally in the octahedral sites with different <111> axes among the four <111> axes in the cubic crystals, the anisotropy energy produced by (2.4) becomes

$$E_a = \frac{1}{4}N\lambda LS(|\cos\theta_1| + |\cos\theta_2| + |\cos\theta_3| + |\cos\theta_4|),$$

Where $\theta_1, \theta_2, \theta_3$, and θ_4 are the angles between S and the four <111> axes. By Fourier expansion, $|\cos\theta|$ is reduced, finally (2.5) becomes

$$E_a = -\frac{32\pi}{135}N\lambda LS\,(\alpha_1{}^2\alpha_2{}^2 + \alpha_2{}^2\alpha_3{}^2 + \alpha_3{}^2\alpha_1{}^2).$$

Comparing this term with the cubic anisotropy term in eq. (2.2), one sees that the first order anisotropy constant K_1 is related to λ. In cobalt ferrites, the anisotropy constant in eq. (2.6) is positive because $\lambda < 0$. Due to this reason, the anisotropy constant K_1 of spinel ferrites can be increased by adding Co^{2+} in the spinel ferrite structure, as the values of K_1 in most spinel ferrites are negative [20][21].
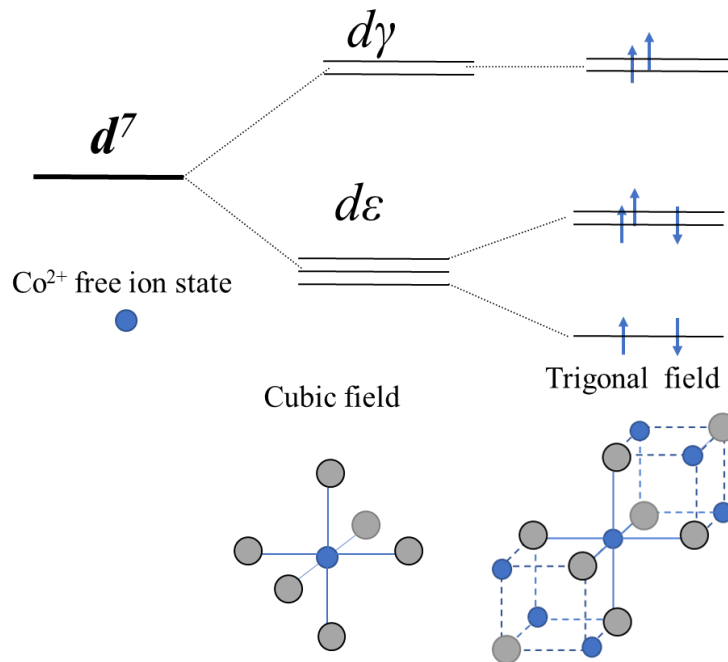
Fig. 2.2 Schematic diagram illustrating the splitting of energy levels of $3d$ electrons by crystal fields with different symmetry (arrows represent spins of a Co^{2+} ion).

2.2.3. Magnetic annealing and directional ordering of Co^{2+}

Another type of anisotropy in cobalt ferrites is the induced magnetic anisotropy obtained via magnetic annealing. The intrinsic property related to this induced anisotropy is magnetostriction and it will be further discussed in Section 2.4. Here, we will discuss the induced anisotropy in cobalt-iron ferrites and cobalt ferrites obtained via magnetic annealing. Magnetic annealing is a procedure in which mixed solid solutions are quenched from an elevated temperature under an applied magnetic field. The procedure has been found to improve the energy product, $(BH)_{max}$ parameter which measures the quality of a permanent magnet material, of the O.P. magnets made of cobalt-iron spinel ferrites.

Such induced uniaxial anisotropy can be explained using the theory of directional ordering proposed by Néel [22][23]. According to this theory, the local atomic configuration became anisotropic under a certain anisotropic treatment, leading to the stabilization of the magnetization direction along the additional uniaxial magnetic anisotropy axis. The term directional ordering refers to the macroscopic anisotropy induced in the local atomic configuration. In the case of cobalt-iron spinel ferrites, or cobalt added magnetites, there are two different divalent ions, e.g. Fe^{2+} and Co^{2+} occupying the octahedral B sites. When the B sites are equally populated by the Fe^{2+} and Co^{2+} ions, the mean local configuration is isotropic. However, given an anisotropic treatment such as magnetic annealing, the local configuration may become anisotropic as the two ions would distribute unevenly upon heating in an external magnetic field.

Slonczewski also explained this behavior in terms of the one-ion anisotropy model of the octahedral Co^{2+} ion [19]. The energy levels are split as shown in **Fig. 2.2**, where the doublet produced gives rise to a uniaxial anisotropy with its axis parallel to <111>. If all the Co^{2+} ions are distributed equally along the four equivalent <111> axes, the uniaxial anisotropies cancel out because of the cubic symmetry. When this ferrite is cooled in a magnetic field, the Co^{2+} ions tend to occupy the octahedral sites of which the <111> axis is nearest to the magnetic field, to lower the anisotropy energy. After cooling, this unbalanced distribution of Co^{2+} ions result in an induced anisotropy. Theoretically, this one-ion induced anisotropy should be proportional to the available number of Co^{2+} ions.

Bozorth et al. investigated the magnetic anisotropy and magnetostriction of several cobalt-based spinel ferrites [24]. They found that compared to the off-stoichiometric cobalt ferrites with Co:Fe ratio of 1:3, the nearly stoichiometric cobalt ferrite with Co:Fe ratio of 1:2 did not respond to magnetic annealing. Although the behavior may also be explained using the theory of directional ordering, the preparation of the off-stoichiometric cobalt ferrite involved the mixture of cobalt ferrite and magnetite, therefore the contribution of Fe^{2+} to anisotropy makes it difficult to distinguish the origin of the anisotropy due to octahedral Co^{2+} in the material.

Iida et al. measured the induced anisotropy for Co-ferrites [25] and discovered that the magnetic annealing effect is sensitive to the partial pressure of oxygen during cooling. It was found that the material responds to magnetic annealing only when it is more or less oxidized. In other words, the magnetic annealing effect is effective in the presence of lattice vacancies and/or when the spinel structure is slightly off-stoichiometric. The lattice vacancies are assumed to speed the diffusion of ions, thus promoting directional ordering of the Co^{2+} - Co^{2+} pairs.

To conclude this section, the intrinsic anisotropy of cobalt ferrite originates from the low symmetry of the trigonal field created by the octahedral Co^{2+} ions. The induced anisotropy from magnetic annealing proves to be effective due to the sensitive response of cobalt ferrites to anisotropic treatments. Indirectly, it also is related to the trigonal field of the octahedral Co^{2+} ions as explained by Slonczewski [19].

2.3. The Jahn-Teller effect of Cu^{2+} in tetragonal copper ferrites

Considering the directional ordering theory, another type of anisotropic treatment which can be performed to obtain macroscopic anisotropy is by applying uniaxial stress or strain. In spinel ferrites, one type of internal lattice strain which can be spontaneously realized is via the Jahn-Teller effect. In this section, we first review the Jahn-Teller effect. Then, we will review the cooperative JT effect in spinel copper ferrites, a phenomenon which leads to the cubic-tetragonal phase transition of the crystal.

2.3.1. Phenomenology of the Jahn-Teller effect

The **Jahn–Teller (JT) effect**, also referred to as **Jahn–Teller distortion**, describes the spontaneous geometrical distortion of molecules and ions associated with certain electronic configurations. **Fig. 2.3** shows the electronic configurations of representative $3d$ cations which exhibit a strong Jahn-Teller effect. The cations are placed in the octahedral coordination which corresponds to the B site of the spinel structure. When the energy level is occupied in an asymmetric manner, a degenerate state exists for that coordination environment. The **Jahn-Teller theorem** states that the coordination environment must distort in order to lower the symmetry and remove the degeneracy (Dunitz and Orgel, 1957) [26].
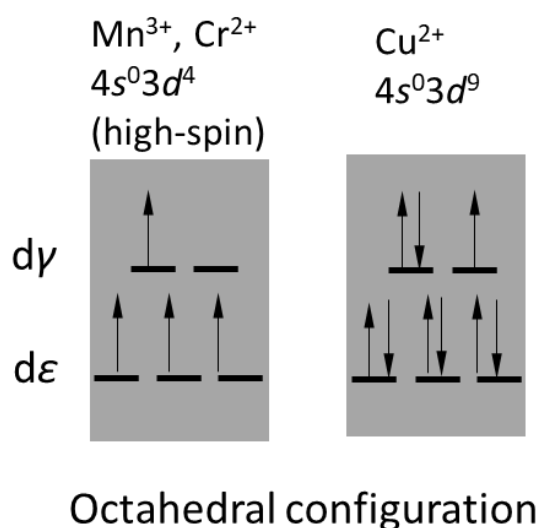
Fig. 2.3 The electronic configurations of representative $3d$ cations in octahedral coordination which show strong tendencies of Jahn-Teller effect.

2.3.2. Cooperative Jahn-Teller effect and the phase transition in spinel $CuFe_2O_4$

Generally, the JT effect is associated with localized degeneracies such as those occurring in a small molecule and/or in an isolated transition metal complex. However, in many periodic high-symmetry solid-state systems, like that in the spinel structure, the interstitial crystalline sites (A and B sites) may also become JT activated centers which allow for electronic degeneracy of the lattice. Under adequate compositions of these JT activated sites, a cooperative JT effect is produced, where global distortions of the crystal occur due to the local degeneracies. The adequate composition of the JT ions (i.e. Cu^{2+}, Mn^{3+}, etc.) is the key element to establish long-range order distortions in the lattice, which leads to a structural phase transition. Because the metal-ligand overlap is strongest for the dγ orbitals of an octahedral complex, the JT effect is much more significant for $3d^4$ and $3d^9$ electronic configurations in high spin states (e.g., Mn^{3+}, Cr^{2+}, Cu^{2+} [26]). As these JT ions occupy the B sites of the spinel structure, a tetragonal phase may occur as a result of the cooperative Jahn-Teller distortion around the coordination environments. **Table 2.2** summarizes the $3d$ cations with the respective JT effects when placed in the tetrahedral A site or in the octahedral B site (After Ohnishi and Teranishi 1964) [27].

One classical representative of the cooperative JT effect is that observed in the cubic-tetragonal spinel copper ferrite system [28][29][30]. As described in section 2.1, most spinel ferrites crystallize in cubic symmetry. One exception is copper ferrite ($CuFe_2O_4$), which is known to exist in both cubic and tetragonal symmetries. Like many spinel ferrites, copper ferrite mainly crystalizes in the inverse spinel configuration, where most of the Cu^{2+} ions reside in the octahedral B sites. The cubic-tetragonal phase transition thus occurs due to the JT effect of the octahedral Cu^{2+} ions. **Fig. 2.4** shows the crystal field splitting of energy levels of the octahedral Cu^{2+} ions due to JT distortion. Cu^{2+} ion has $9d$ electrons with a configuration of $(d\varepsilon)^6 (d\gamma)^3$. When the energy level is raised due to the geometrical elastic energy, according to the JT theorem it can be compensated by lowering the symmetry of the electronic configurations. In **Fig. 2.4**, we can see that the tetragonally distorted configuration is more profitable in terms of energy and it follows by an extension along the z-axis called the Jahn Teller distortion.

In the case of copper ferrite crystals, it is known that by rapid cooling the crystal after annealing above 760°C, it will crystalize in the cubic phase [31][32]. At high temperature (above 760°C), the Cu^{2+} cation tends to migrate to the tetrahedral A site which in turn suppressed the JT effect, causing the transition to the highly ordered cubic phase [33][34]. Hence, rapid cooling from such temperature would 'freeze' the cubic structure. On the other hand, slow cooling would enable the stabilization of the tetragonal phase as the Cu^{2+} ions migrate to the octahedral sites. When there are enough octahedral Cu^{2+} ions to serve as JT activated sites, the competition between elastic and electronic energy make it favorable for the total crystal to distort into the tetragonal phase. Ohnishi et al. has shown that to realize tetragonal distortion (phase transition) in copper ferrites, at least 75% of the Cu^{2+} must reside in the octahedral B site [35].

Table 2.2 The tendency of Jahn-Teller effect in *M*-doped spinel compounds [27]

Number of *d*-electrons and *M* cations		B-site	A-site
0	5 Fe^{3+}, Mn^{2+}	0	0
1	6 Fe^{2+}	Small	Small
2	7 Co^{2+}	small	0
Cr^{3+}, Mn^{4+} 3	8 Ni^{2+}	0	Small ($c/a>1$)
Cr^{2+}, Mn^{3+} 4	9 Cu^{2+}	Large ($c/a>1$)	Large ($c/a<1$)

(a)　　　　　　(b)　　　　　　(c)
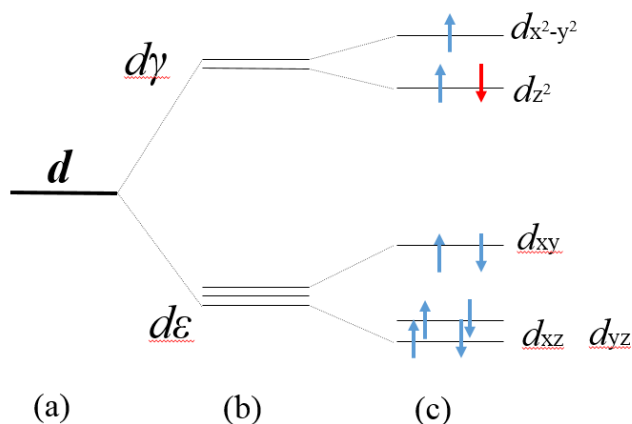
Fig. 2.4 Splitting of energy levels of $3d^9$ electrons (Cu^{2+}) by crystal fields: (a) free ions; (b) cubic crystal field; (c) tetragonal crystal field (arrows represent spins of a Cu^{2+} ion)

2.4. Magnetoelastic anisotropy in cobalt ferrite thin films

As described in Chapter 1, we want to develop permanent magnet materials based on spinel cobalt ferrite by inducing tetragonal distortion via the JT effect of Cu^{2+}. In this case, the strain-induced anisotropy is due to the magnetoelastic energy originating from the magnetostrictive properties of the spinel ferrite. In this section, we will briefly introduce the phenomenology of magnetostriction and then describe the formalism of magnetoelastic anisotropy. Finally, we will review the magnetoelastic anisotropy model in epitaxially grown cobalt ferrite thin films.

2.4.1. Phenomenology of magnetostriction and magnetoelastic anisotropy

Magnetostriction

Magnetostriction is a change in dimension of a solid that accompanies a change in magnetic state. The magnetostrictive effect was first discovered by Joule in 1842. The inverse effect, called the magnetoelastic effect, is a change in magnetic structure of a material induced by a change in the mechanical state. For example, when magnetized in an external magnetic field, an iron sphere will deform to form an ellipsoid. Magnetically-induced deformation is referred to as magnetostriction λ, to distinguish it from mechanical strain ε. A linear strain $\lambda = \delta l / l$ in the direction of magnetization is associated with the magnetization process. The magnetostrictive strain at saturation relative to the sample's length in the demagnetized state is called saturation magnetostriction λ_s. For the purpose of comparison among materials, the parameter λ_s is usually used as a characteristic value of magnetostrictive properties because it is an intrinsic property of the material.

Magnetostriction for isotropic materials or for randomly oriented polycrystals can be expressed as a function of θ by

$$\lambda(\theta) = \lambda_s \frac{3cos^2\theta - 1}{2}$$

(2.7)

where θ is the angle between the measurement direction and the magnetization direction.

Magnetoelastic anisotropy

By imposing a uniaxial stress σ (Nm^{-2}) on a ferromagnetic material, one can create strain-induced anisotropy, also known as magnetoelastic anisotropy. This is because an applied tensile strain can rotate the magnetization away from the easy direction, depending on the magnitude of the strain ε and the strength of the magnetoelastic coupling coefficient. Similar to λ_s, the magnetoelastic coupling coefficient (usually denoted as B_1) is a material's intrinsic property and is used as a characteristic value to compare materials.

In the case of an isotropic polycrystalline body, the magnetoelastic energy density E_{me} associated with a stress σ is:

$$E_{me} = -\frac{3}{2}\lambda_s\sigma cos^2\theta$$

(2.8)

Comparing with the expression of uniaxial anisotropy energy in eq. (2.1), $E_a = K_u \sin^2\theta$, we see that the magnetoelastic anisotropy energy K_u^{me} is

$$K_u^{me} = -\frac{3}{2}\lambda_s\sigma_i$$

(2.9)

where σ_i is the stress tensor, which can be expressed in terms of the elastic modulus C_{ij} and strain ε_j as $\sigma_{ij} = C_{ij}\varepsilon_j$ [6].

For a cubic crystal symmetry, the corresponding magnetoelastic energy density is:

$$E_{me} = B_1(\varepsilon_{xx}\alpha_1^2 + \varepsilon_{xx}\alpha_1^2 + \varepsilon_{xx}\alpha_1^2) + B_2(\alpha_1\alpha_2\varepsilon_{xy} + \alpha_2\alpha_3\varepsilon_{yz} + \alpha_3\alpha_1\varepsilon_{zx})$$

(2.10)

where ε_{ij} is the strain tensor and $(\alpha_1, \alpha_2, \alpha_3)$ are the cosine directions of the cubic axes. Fundamentally, eq. (2.9) and (2.10) show that an imposed stress σ_i or strain ε_{ij} may give rise to a magnetoelastic anisotropy proportional to the strength of the magnetoelastic (ME) coupling coefficients, B_i $(i = 1, 2, …)$.

2.4.2. Magnetoelastic anisotropy in epitaxial cobalt ferrite thin films

Consider the case of a uniaxial strain in the form of tetragonal distortion, such as that produced in epitaxial cobalt ferrite (CFO) thin films [3]. The epitaxial CFO (001) thin films were grown on MgO(001) substrates and the tetragonal distortion is essentially obtained by lattice mismatch between the substrate and the film. The magnetoelastic anisotropy can be considered by following the model discussed by Schulz et al. and Thamankar et al. in the case of Fe-Ni alloy epitaxial thin films [1][2].

In the case of epitaxially grown thin films, there is a pseudomorphic growth regime in which the substrate exerts lateral (tensile) stress ε_1 on the film due to the lattice mismatch, to yield the associated tetragonal distortion ε_2 (compressive stress). The mismatch between the lattice parameters of the substrate and the thin film results in a build-up of elastic energy, which can be minimized by changing the out-of-plane lattice constant of the thin film, compared to the bulk value. For a given ε_1, the elastic energy is minimized with respect to the resulting tetragonal strain ε_2, and the following expression is derived:

$$\varepsilon_2 = \frac{-2C_{12}}{C_{11}}\varepsilon_1$$

(2.11),

where C_{11} and C_{12} are the cubic elastic moduli. Hence, the uniaxial magnetoelastic anisotropy due to tetragonal distortion from epitaxial strain can be expressed as

$$K_u^{me} = \frac{3}{2}\lambda_{100}(C_{11} - C_{12})(\varepsilon_2 - \varepsilon_1)$$

(2.12).

Here, λ_{100} is the magnetostriction constant for a uniaxial distortion along the [100] direction. The term $(\varepsilon_2 - \varepsilon_1)$ denotes the tetragonal distortion and it can also be expressed in terms of tetragonality χ as

$$\chi = \frac{c - a}{a} = \frac{c}{a} - 1$$

(2.13),

where a and c are the lattice parameters of the tetragonal lattice normalized to the cubic coordinates, and c/a denotes the tetragonal distortion. Now, if we express the magnetoelastic coupling coefficient B_1 as

$$B_1 = \frac{3}{2}\lambda_{100}(C_{12} - C_{11})$$

(2.14),

we can rewrite eq. (2.12) in the form of B_1 and tetragonality χ as

$$K_u^{me} = B_1\chi$$

(2.15).

Equation (2.15) summarizes the phenomenological model of magnetoelastic anisotropy in the case of tetragonal distortion (uniaxial strain). From the elastic moduli of bulk cobalt ferrites and the magnetostriction constant, one can estimate the value of K_u^{me} for cobalt ferrite thin films on MgO(001) substrates. Conversely, by measuring the uniaxial magnetic anisotropy K_u, one can estimate the value of the magnetoelastic coefficient B_1, for comparison with the bulk value.

Tainosho et al. investigated the epitaxial strain dependence of anisotropy in tetragonally distorted CFO(001) thin films to elucidate the limitation of the magnetoelastic model described above. The tetragonal distortion was varied by varying the thickness of the films and the resulting magnetic anisotropy was measured using the torque method. Using eq. (2.15), the uniaxial anisotropy was plotted against the tetragonality. From the linear fit, the experimental data showed that the magnetoelastic model is highly applicable even under a large strain of 3% [4]. The slope of the linear fit was taken as the ME coupling coefficient B_1, and the value was compared with that calculated for bulk cobalt ferrite.

2.4.3. Limitation of the epitaxial strain for permanent magnet applications

In the pioneering work regarding tetragonal CFO thin films by Niizeki et al., the reported value of perpendicular magnetic anisotropy obtained by torque measurement was as high as 1.5 MJ/m^3, with an estimated anisotropy field of 5 T. This result suggests that CFO can be a promising candidate for RE free permanent magnets. However, it is completely impractical to produce bulk magnets from thin film technology. Furthermore, since the epitaxial strain is developed via the lattice mismatch, the resulting tetragonal distortion has a strong dependence on film thickness. Increasing the thickness of the thin film results in lattice relaxation which reduces the magnitude of the epitaxial strain [36]. This also shows that the epitaxial thin films are not feasible for bulk applications.

To address this limitation, it is important to fabricate tetragonal spinel ferrite in the form of particles that can serve as building blocks for bulk materials, i.e. for their application as permanent magnets. In this case, epitaxial strain is no more applicable, and so we propose to exploit Jahn-Teller distortion to induce magnetoelastic anisotropy in cobalt-based spinel ferrite nanoparticles. As with epitaxial strain, JT distortion is a one-dimensional (tetragonal) distortion involving the extension/distortion of the c-axis. The magnetoelastic model which couples the JT effect of Cu^{2+} and the ME effect of Co^{2+} in the tetragonally distorted spinel ferrite particles is described in Chapter 5.

3. Theory of coercivity

Coercivity characterizes the resistance of a ferro- or ferrimagnetic material to demagnetization and is a key requirement for permanent magnets. It is typically defined as the value of external field needed to demagnetize a previously saturated sample, though in some cases it is defined as the field at which the derivative of magnetization with respect to field is maximum.

Understanding the physics of coercivity, whether through simulations, calculations or using phenomenological approaches, has been the subject of intensive studies since many decades of scientists within the academic community and among their industrial counterparts who seek to develop materials with higher coercivity (stronger permanent magnets).

In the following sections, we will first review the origin of coercivity. Then we will briefly describe magnetization reversal in uniaxial systems by considering the simplest model of coherent rotation – the Stoner-Wohlfarth (SW) model. For real systems, we will review two models – the micromagnetic (MM) model – which is considered as an extension of the SW model applicable to real systems. The other model is the global model (GM), one where the magnetization reversal energy is associated with thermal activation and with a critical volume the formation of which is related to the domain wall energy.

3.1. Origin of coercivity: Anisotropy

Hard magnetic materials are characterized by their strong magnetic anisotropies, which implies the existence of energetically favorable directions for magnetization. The magnetic anisotropy energy can thus be expressed as an angular-dependent energy, either related to the crystalline axes (magnetocrystalline anisotropy) or related to the macroscopic shape of the sample (shape anisotropy). The axis direction corresponding to the lowest energy state is the easy axis, while that corresponding to the highest energy is the hard axis. For uniaxial anisotropy systems which have a unique easy axis, the angular dependence of uniform reversal has been derived by Stoner and Wohlfarth [37], where they considered the simple case of magnetization reversal in a single domain particle with uniaxial magnetic anisotropy and a positive anisotropy constant K_1.

The energy density of uniaxial magnetic anisotropy is given in eq. (2.1). Except in special cases where high-order terms become important (such as in the case of NdFeB magnets at low temperature [38]), only the first order anisotropy constant is considered, giving the expression in eq. (2.1)

$$E(\theta) = K_1 \sin^2\theta$$

Consider $K_1 > 0$, two equivalent energy minima corresponding to $\theta = 0$ and $\theta = \pi$ exist (**Fig. 3.1**). In the minimum energy states, the magnetization prefers to lie along the easy-axis, in either the negative or the positive direction. In the absence of an external magnetic field, the system will occupy one of the two possible states with equal probability (**Fig. 3.1** (a)). The two energy minima are separated by a maximum at $\theta = \pi/2$, which corresponds to the hard-axis. Therefore, the anisotropy energy is the energy needed to align the magnetization perpendicular to the easy axis.

Consider now that the magnetization is aligned along the easy axis at $\theta = 0$ and a magnetic field H is applied along the same axis in the opposite direction, $\theta = \pi$. The energy associated becomes:

$$E(\theta) = K_1 \sin^2\theta + \mu_0 M_s H \cos\theta$$

(3.1)

where the second term represents the Zeeman energy and M_s is the spontaneous magnetization.

As the field strength H is increased, the energy minimum corresponding to the magnetization anti-parallel to H ($\theta = 0$) is progressively raised whereas that corresponding to the magnetization parallel to H ($\theta = \pi$) is lowered. In low applied field, the magnetization remains anti-parallel to the field. At $H = H_c$, the energy barrier between the two states vanishes and the magnetization flips and aligns along the applied field.

3.2. The ideal system: Stoner-Wohlfarth model

Nucleation implies the occurrence of instabilities in a saturated magnetic state for a certain value of an applied field, the nucleation field H_n. In the Stoner-Wohlfarth (SW) model, magnetization is considered homogenous and the magnetic moments parallel at all times. Under an applied external field, the total energy density of a SW system with a strong uniaxial anisotropy is given as the sum of the uniaxial magnetic anisotropy energy and the Zeeman energy, as in eq. (3.1). The local minimum energy state is derived from the equality $\partial E / \partial \theta = 0$, giving

$$2K_1\sin\theta\cos\theta - \mu_0 M_s H\sin\theta = 0$$

$$(3.2)$$

$$\sin\theta(2K_1\cos\theta - \mu_0 M_s H) = 0$$

$$(3.3)$$

if $\sin\theta = 0$, then $E(\theta = 0)$ and $E(\theta = \pi)$ are the minimum energy states, E_{min}

if $2K_1\cos\theta - \mu_0 M_s H = 0$ then $E\left(\cos\theta = \frac{2K_1}{\mu_0 M_s H}\right)$ is the maximum energy state, E_{max}.

Considering that at the nucleation field, the first instability in the moment configuration will occur, the energy barrier E_a depicted in **Fig. 3.1** becomes 0, corresponding to $E_{min} = E_{max}$, giving

$$H_n = \frac{2K_1}{\mu_0 M_s}$$

$$(3.4)$$

which is the anisotropy field H_A. In an ideal system such as that considered in the SW model, the homogenous magnetization is assumed to rotate uniformly and the coercivity field is equal to the nucleation field, which is also the anisotropy field ($H_c = H_n = H_A$). In real systems, however, reversal is considered to begin at defects, and it may be decomposed into two stages, nucleation and propagation. The larger of the associated critical fields would determine the value of the coercive field.
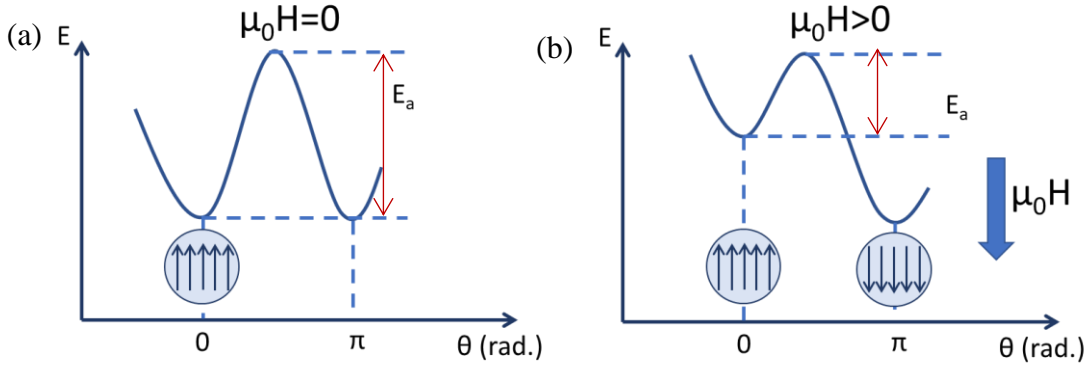
Fig. 3.1 Schematic diagrams of the energy barriers in the case of a uniaxial system (a) with no external magnetic field and (b) with an external applied field H.

3.3. General models of coercivity in real materials

In real materials, magnetization reversal is complex and may involve one or more events including;

i)   nucleation of reversed domains at low anisotropy points followed by the formation of domain walls,

ii)   propagation of these domain walls into the main saturated phase,

iii)   pinning – depinning of domain walls

Each event takes place at a certain value of the external applied field, the highest of them being the coercive field. In order to characterize hard magnetic materials such as permanent magnets, it is important to understand why a certain process happened for that certain field before relating it to the microstructure. By knowing how the microstructure should be optimized, one can exploit better the intrinsic properties of the materials.

Since the said microstructural properties consist of lattice defects, it is almost impossible to probe directly their characteristics, i.e. the critical lengths concerned are too small to be accessible to experiment. To solve this problem, several models of coercivity have been developed so that one can determine the relevant microstructural features by indirect measurements. These models also consider the physical properties of the main phase (not defects) which are accessible to experiments. Empirical relations between coercivity and main phase properties are derived in several terms associated with microstructure parameters.

One of the approaches is to analyze the temperature dependence of coercivity. The idea is that the coercivity and the other physical properties such as M_s and K_u of the main phase are temperature dependent whereas the microstructure may be considered as independent of temperature (although, this may not always be the case). The coercivity models are developed in an attempt to find a linear relation between coercivity and physical properties so that the microstructure parameters can be extracted as constants.

3.4. Micromagnetic approach

The most used approach to analyze $H_c(T)$ is the so-called micromagnetic model (MM). In the framework of this model, the coercive field is expressed as

$$H_c(T) = \alpha \frac{2K_1(T)}{\mu_0 M_s(T)} - N_{eff} M_s(T)$$

(3.5),

where H_c is the coercive field, K_1 is the first order uniaxial magnetocrystalline anisotropy constant, and M_s the spontaneous magnetization. In this model, α and N_{eff} are considered as temperature independent parameters which are associated with microstructural properties. Hereafter we shall denote these parameters as α^{MM} and N_{eff}^{MM}.

Equation (3.5) was initially introduced on purely phenomenological grounds to access microstructural parameters using an empirical approach [39][40]. Kronmüller and co-workers showed that the equation may be derived from linearization of the classical micromagnetic equations in the case of inhomogeneous systems, characterized by strong magnetocrystalline anisotropy with local deviations of the anisotropy constant [41][42]. It is assumed that nucleation of reversed domains starts at defect points where the anisotropy is a fraction of the anisotropy of the main phase. The first term of eq. (3.5) represents the critical field which depends on the actual mechanism involved in magnetization reversal, and the parameter α represents how much the anisotropy is lowered at the starting point of nucleation. The second term describes dipolar interactions via the average parameter N_{eff}. Note that the dipolar interactions evaluated via this model were found to be very significant: $N_{eff} \approx 1.6 - 1.8$ [42], which corresponds to a reduction of about 2.7 T of the coercive field of sintered NdFeB magnets at 300 K. It is claimed that the MM model can be used to distinguish between nucleation and pinning governed coercivity [42].

3.5. Global approach

Another model is the so-called Global Model (GM) proposed by Givord et al. [8][43][44]. In contrast with the Stoner-Wohlfarth and micromagnetic models, the global model does not relate the coercivity directly to the anisotropy of the main phase. Rather it considers in a more global sense, what the various possible processes of magnetization reversal have in common. The concept of activation volume is used and the coercivity is related to this parameter which can be accessed experimentally from time and field dependent measurements.

3.5.1. Derivation of the H_c(T) equation in the global model

Regardless of the mechanism involved, the process of magnetization reversal begins with the formation of a nucleus of volume v_a (known as the activation volume) with an inversed magnetization. The cost of this operation is proportional to the increase of the associated domain wall energy, $\gamma's$. The surface area, s of the nucleus can be expressed in terms of $v_a^{2/3}$, and the domain wall energy of the nucleus γ' is assumed to be proportional to the domain wall energy γ of the main phase $\gamma' \propto \gamma$. The domain wall energy of the activation volume thus can be expressed as $\gamma's = \alpha\gamma v_a^{2/3}$, where α is a critical field parameter, which considers the dimensional correspondence between s and v_a, in addition to quantifying the relationship between the domain wall energy in the main phase and in the activation volume. Here, α is considered as temperature independent assuming that these two relationships are simply proportional.

The total energy barrier considered to reverse a single nucleus of volume v_a is thus given as

$$\Delta E = -\mu_0 M_s H_c v_a + \alpha\gamma v_a^{2/3} - N_{\text{eff}} M_s v_a$$

(3.6),

where the first term is the Zeeman energy term, the second term represents the domain-wall (formation) energy, and the last term is the effective dipolar energy acting locally on the nucleus.

During magnetization reversal, the GM does not assume a local minimum of the energy barrier like that considered in the MM, but rather a global minimum. The reversal process of a single activation volume is considered in terms of a thermally activated process as follow.

At a given field close to the coercive field, just before the initial reversal occurs, the magnetization fluctuates between two energy states separated by the energy barrier ΔE. When this energy barrier is defined by the thermal energies, the process is called thermal fluctuations and it is the origin of the magnetic viscosity (magnetic after-effect); a phenomenon where the magnetization decays linearly with the logarithmic time scale under a constant applied field. Theoretical interpretation of the magnetic viscosity was proposed by Street & Woolley [45][46] and the physical theories of thermal fluctuation was described by Néel [47]. At a given time τ, the energy barriers may be overcome by the thermal energy, causing the magnetization to reverse. This time is given by the Néel-Arrhenius law

$$\tau = \tau_0 e^{-\frac{E_a}{k_B T}}$$

where τ_0 is a constant of the order of 10^{-9} s, E_a is the height of the energy barrier that will be surpassed after time τ and k_B is the Boltzmann's constant. For DC magnetization measurements using an average laboratory magnetometer, the typical measurement time τ is averaged to 100 s. This gives the average thermal energy of $25 k_B T$.

Therefore, at a given field close to the coercive field, the energy barrier ΔE in eq. (3.6) vanishes when the total energy equals to $25 k_B T$ and reversal is initiated. The total energy barrier equation for which reversal occurs is now expressed as

$$\Delta E = -\mu_0 M_s H_c v_a + \alpha\gamma v_a^{2/3} - N_{\text{eff}} M_s v_a = 25 k_B T$$

(3.7).

One then derives the following expression for the coercive field H_c in the GM by rearranging eq. (3.6):

$$H_c = \alpha \frac{\gamma}{v_a^{1/3} \mu_0 M_s} - N_{eff} M_s - \frac{25 k_B T}{\mu_0 M_s v_a}$$

(3.8).

The activation volume v_a at finite temperature is given as

$$v_a = \frac{k_B T}{\mu_0 M_s S_v}$$

(3.9),

where S_v is the magnetic viscosity coefficient, which is experimentally accessible through magnetic after-effect measurements, also called magnetic viscosity measurements. Replacing this in the last term of eq. (3.8), one gets the expression

$$H_c = \alpha \frac{\gamma}{v_a^{1/3} \mu_0 M_s} - N_{eff} M_s - 25 S_v$$

(3.10).

Using the notation $H_0 = H_c + 25\, S_v$, eq. (3.10) becomes

$$H_0 = \alpha \frac{\gamma}{v_a^{1/3} \mu_0 M_s} - N_{eff} M_s$$

(3.11),

where H_0 represents the coercive field corrected for thermal effects. The two parameters: α and N_{eff} can then be extracted empirically by plotting H_0/M_s vs. $\gamma/v_a^{1/3}\mu_0 M_s$. For the global model, we shall hereafter denote these parameters as α^{GM} and N_{eff}^{GM}. Note that the α^{GM} parameter does not have a simple physical meaning such as the α^{MM} that was interpreted in the micromagnetic model.

3.5.2. The activation volume and magnetic viscosity

The activation volume v_a parameter used in the global model can be derived from magnetic viscosity measurements [48][47]. The formalism to derive the activation volume v_a in eq. (3.9) is described as follow:

Given E_a is the energy barrier for a single reversal (activation) process for a nucleus with volume v_a, it can be expressed as follow

$$E_a = v_a \mu_0 M_s H_c$$

(3.12).

During the reversal process, the variation of magnetization M, dM is given as

$$dM = 2 M_s f(E) dE$$

(3.13),

where M_s is the spontaneous magnetization and f(E) is the distribution function of the energy barriers. The time taken for reversal to occur is, as described from the thermal fluctuation theory, given as

$$t = \tau_0 e^{-\frac{E_a}{k_B T}}$$

from which one derives the variation of energy barrier with logarithmic time as

$$\frac{dE_a}{d\ln t} = k_B T$$

(3.14).

From eq. (3.13), one derives the expression of magnetic viscosity S; which is the variation of M with logarithmic time as

$$S = \frac{dM}{d\ln t} = 2 M_s f(E) \frac{dE_a}{d\ln t} = 2 M_s f(E) k_B T$$

(3.15).

Fundamentally, eq. (3.15) shows that the magnetic viscosity is proportional to temperature, given that $2M_s f(E)$ is a constant. Next, we consider the variation of M in eq. (3.13) with the applied field H,

$$\frac{dM}{dH} = 2 M_s f(E) \frac{dE_a}{dH}$$

(3.16).

Using the derivatives of E_a in eq. (3.12) and substitute it in eq. (3.16), one gets

$$\frac{dM}{dH} = 2 M_s f(E) v_a \mu_0 M_s$$

(3.17).

During magnetization reversal, eq. (3.17) corresponds to the irreversible susceptibility χ^{irr} as only the irreversible changes of the magnetization with the applied field is considered. Experimentally, this can be

accessed by measuring the total susceptibility χ^{tot} and the reversible susceptibility χ^{rev} (see Chapter 4 for the measurement protocols), where the relation is given as

$$\chi^{\text{irr}} = \chi^{\text{tot}} - \chi^{\text{rev}}$$

(3.18).

Finally, by comparing the time-dependent measurement in eq. (3.16) and the field-dependent measurement in eq. (3.18), one derives the expression of magnetic viscosity coefficient, S_v as follow

$$S_v = \frac{S}{\chi^{\text{irr}}} = \frac{\dfrac{\text{d}M}{\text{d}\ln t}}{\dfrac{\text{d}M}{\text{d}H}} = \frac{k_B T}{v_a \mu_0 M_s}$$

(3.19).

Rearranging eq. (3.19), one gets the expression of activation volume shown in eq. (3.9), that is $v_a = \frac{k_B T}{\mu_0 M_s S_v}$.

4. Sample preparation and characterization techniques

This chapter reviews the experimental techniques and analysis methods used throughout this thesis. For the sample preparation, first we briefly introduce the basics of the synthesis techniques employed in this study. Then we describe how we implement the methods in our study; i.e. the recipe and preparation of the particles. Concerning characterization, we will briefly recall the principles of the main techniques used such as transmission electron microscopies (TEM), x-ray diffraction (XRD) and vibrating sample magnetometry (VSM). We will discuss in more detail the principles of Mössbauer spectroscopy which was employed to analyze the Fe cation distribution and local structural analysis. We also describe the rotational hysteresis analysis using torque measurements which was employed to determine the anisotropy field. Finally, one section is dedicated to describing measurement protocols used for coercivity analysis.

4.1.   Sample preparation
4.1.1.   Synthesis techniques

The particles were synthesized via a chemical route following 3 main steps including i) nucleation via the coprecipitation method, ii) particle growth via the flux method and iii) tetragonalization via a heat-treatment process.

(i)   *Coprecipitation method*

Coprecipitation is the simultaneous precipitation of normally soluble components by the formation of mixed crystals [49]. Consider an aqueous solution containing 2 or more metallic ions. At a certain range of pH where both metal hydroxides precipitate, the metallic ions of each type will precipitate simultaneously. This process is referred to as coprecipitation. This method is one of the most simple and convenient methods of synthesizing ferrite nanoparticles. Using aqueous salts of Fe^{3+} and the corresponding divalent cation salt M^{2+}, nanoparticles are formed by the addition of a base either at room temperature or at elevated temperature. The factors affecting the composition, size, and shape of the nanoparticles include: (i) Type of M^{2+}, ratio of M^{2+}/Fe^{3+}, (ii) temperature of reaction, (iii) type of salts used (chloride, nitrate, etc.), (iv) pH (e.g. concentration of NaOH) and (v) the addition of surfactants. Due to its simplicity and convenience, this method is mostly used for large scale production. However, one major disadvantage of this method is the broad size distribution of the particles. For the formation of spinel ferrite nanoparticles, the typical equation of reaction by coprecipitation is given as

$$2Fe^{3+} + M^{2+} + 8OH^- \rightarrow MFe_2O_4 + 4H_2O$$

(4.1).
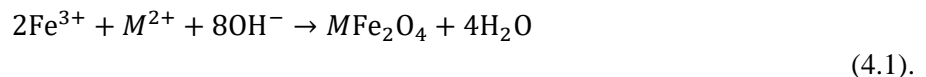
In practice, highly alkaline media tend to produce the needle-like goethite phase (α-FeOOH or δ-FeOOH) as impurities together with the spinel phase (magnetite, Fe_3O_4) [50]. High concentration and reaction temperatures usually favor the formation of spherical nanoparticles because the direction of crystallographic growth is more isotropic and less selective [51]. In this study, during coprecipitation the suspensions were kept at 95°C under continuous stirring (250 rpm) for 3 h; a process called 'digestion' or 'aging'. This aging process helps to narrow the size distribution and reduce the impurities by transforming the goethite phase to the spinel phase, and thus improving the crystallinity and magnetic properties of the spinel ferrites [52].

(ii)   *Flux method*

The flux method, also known as the molten salt method and the salt bath method, is a method of crystal growth where the components of a desired substance are dissolved in a flux. It is particularly suitable to grow crystals free from thermal strain. The process takes place in a crucible made of highly stable, non-reactive material, in which the reactant and the flux are mixed and heated to a temperature high enough to melt the flux. The flux agent acts as a solvent and can be formed of metals, hydroxides, salts, etc. The range of operating temperature in a flux method depends on the melting and boiling points of the flux agent. Salt based flux are popular due to their water-soluble properties making it easy to separate the solvent, furthermore some salts such as NaCl and KBr have a wide range of operating temperature. For chloride base salt such as NaCl, the molten salt may decompose to produce Cl_2 at high temperature, which can cause corrosion of the crucible

and/or the grown crystals. In this study, we have selected a bromide salt, KBr as the flux agent. The melting point of KBr is 734°C and the boiling point 1435°C, and the annealing temperature can be varied in the range between these two points.

(iii)   *Tetragonalization process induced by Cu^{2+}*

We recall that the aim of this thesis is to study tetragonally distorted (Cu,Co)-ferrite particles produced via the cooperative JT effect induced by Cu^{2+}. As we have reviewed in the previous chapter, the critical composition of Cu^{2+} to realize is 75% in the octahedral B site. Considering this, the composition of particles is varied as $Cu_{1-x}Co_xFe_2O_4$, where $x = 0 - 0.2$. In addition to the critical compositions, the emergence and suppression of the JT effect in Cu^{2+} seems to be highly dependent on the ambient pressure during synthesis [53]. Since optimization of the synthesis process is not in the scope of this thesis, we followed the fabrication protocols reported by Kimura et al. to realize the cooperative JT effect (tetragonal distortion) in (Cu,Co)-ferrite particles [54]. Kimura et al. systematically investigated the effect of heat treatments on the JT distortion in copper ferrite nanoparticles synthesized via the coprecipitation method. The synthesis parameters varied were (i) the annealing temperature (700 – 900°C); and (ii) the quenching methods (furnace cooling, slow cooling and rapid cooling). It was shown that both the annealing temperature and quenching methods are crucial to realize cooperative JT distortion. Specifically, the optimum conditions reported to obtain tetragonal copper ferrite is the annealing temperature of 900°C followed by a furnace cooling process.

4.1.2. Synthesis of (Cu,Co)Fe₂O₄ particles via the coprecipitation and flux methods

Figure 4.1 shows the schematic flow charts of the coprecipitation and the flux processes. $Cu_{1-x}Co_xFe_2O_4$ ($x = 0 - 0.2$) particles were prepared by mixing aqueous solutions of ferric chloride ($FeCl_3.6H_2O$), cobalt chloride ($CoCl_2.4H_2O$), copper chloride ($CuCl_2.2H_2O$) and sodium hydroxide solution (NaOH aq.). The molar ratio of divalent ions ($Cu^{2+} + Co^{2+}$) to the trivalent ions Fe^{3+} was kept constant at 1:2, which is near the stoichiometric composition of spinel ferrites, i.e. MFe_2O_4, while the molar ratio of Co^{2+} to Cu^{2+} was varied as x:($1-x$). The reaction was conducted with a 4-fold molar excess of NaOH to avoid the formation of intermediate products. The mixed suspensions were kept at 95 °C with continuous stirring for 3 h (aging process), after which the obtained nanoparticles were washed several times with water to neutralize the pH. After decantation, the wet suspension containing the particles were mixed with the flux agent, potassium bromide (KBr), at a weight ratio of 1:10, and the mixture was oven-dried at 80°C. The dried mixture was subsequently heated in a muffle oven at 850 °C for 3 hours (flux method). The obtained products were washed several times with water to remove the flux. Finally, tetragonalization is achieved by annealing the particles in air at 700–900°C, followed by furnace cooling over a period of 6 hours (**Fig. 4.2**).

4.1.3. Remark on reproducibility of sample preparation

Most metal chlorides including iron chlorides, copper chlorides, and cobalt chlorides are by nature highly hygroscopic, which means they have high tendency to absorb moisture. Due to this, each compound usually attaches to one or more water molecules to form stable metal chloride hydrate compounds. For example, the metal chloride of iron (III) attaches to 6 water molecules to form $FeCl_3.6H_2O$. Although the chemical reagent $FeCl_3.6H_2O$ is already at its stable state, the hydrophilic parts of the water molecules make the compound hygroscopic. Over time, the reagent will absorb moisture and gain water mass.

In this study, the starting metal chloride reagents ($FeCl_3.6H_2O$, $CoCl_2.4H_2O$, $CuCl_2.2H_2O$) were weighed before dissolved in water for the coprecipitation process. The mass and ratio are fixed so as to yield a certain mole of the product spinel ferrite particles. Since the reagents tends to absorb moisture, they gain mass from water molecules over time. Due to this reason, it is to be noted that the reproducibility of samples prepared in this study depends to a great extent, on the batch of the chemical reagents used and the period of time at which the coprecipitation process takes place.

FeCl$_3$.6H$_2$O (Fe^{3+})
CuCl$_2$.2H$_2$O (Cu^{2+})   NaOH
CoCl$_2$.6H$_2$O (Co^{2+})   /water
        /water

Coprecipitation

Stirring (200 rpm)
at 95°C for 3 hours

(Cu,Co)Fe$_2$O$_4$ suspension
(alkaline)

Neutralization & removal of NaCl
via water-wash

(Cu,Fe)Fe$_2$O$_4$ suspension
(neutral)

Sedimentation &
removal of supernatant liquid

Ready for particle growth
via flux method

(Cu,Co)Fe$_2$O$_4$ Flux agent
precipitate   / KBr

Mixed at 1:10 ratio
(KBr in excess)

(Cu,Co)Fe$_2$O$_4$ + KBr mixture
(wet)

Oven-dried at 80°C

(Cu,Fe)Fe$_2$O$_4$ + KBr mixture
(dry)

Heated in air
at 850°C for 2 hours

Particle growth in molten flux

Fig. 4.1 Schematic flow charts showing the coprecipitation and flux methods in the synthesis process of (Cu,Co)-ferrite particles

(Cu,Co)Fe$_2$O$_4$ + KBr mixture
(dry)

removal of KBr
via water-wash

(Cu,Co)Fe$_2$O$_4$ (powdered form, cubic phase)

Annealed in air
at 900°C for 2 hours

Furnace cooled for 6 hours

Tetragonally distorted
(Cu,Co)Fe$_2$O$_4$ particles
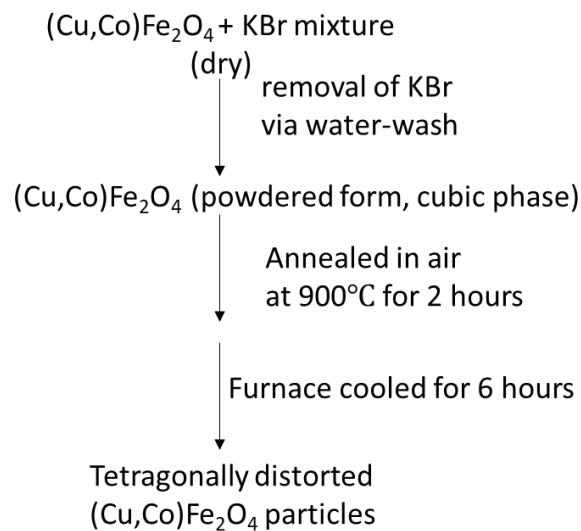
Fig. 4.2 Schematic flow chart of the tetragonalization process as adapted from the conditions optimized by Kimura et al. (Kimura, 2012).

4.2. Basic characterization

In this section, we will briefly recall the basic principles of the main techniques used; transmission electron microscopy (TEM), x-ray diffraction (XRD), vibrating sample magnetometry (VSM).

4.2.1. Transmission Electron microscopy (TEM)

TEM is a microscopy technique where a beam of electrons is transmitted through a very thin sample. As the electron beam passes through the specimen, interactions between the electrons and the atoms in the sample can be used to observe features like the crystal structure, dislocations, grain boundaries, etc. TEM works on the same basic principles as the light microscope but instead of light, it uses electrons. It can be used to observe particles at much higher magnification as the optimal resolution for TEM images is many orders of magnitudes better than that from a light microscope due to the much smaller wavelength of electrons compared to that of light (photons).

Typically, a TEM system is composed of 5 main components which are the electron gun, vacuum system (column), electromagnetic lenses, specimen stage, and imaging device. The principle of TEM imaging is as follow. The electron beam from the electron gun is focused into a small, thin, coherent beam using the condenser lens. Using a condenser aperture, this beam is restricted to exclude high angle electrons. The beam then strikes the specimen and parts of it are transmitted; depending upon the thickness of the specimen. This transmitted portion is focused by the objective lens into an image on a phosphor screen or charge coupled device (CCD) camera, i.e. the imaging device. The image which passes down the column through the intermediate and projector lenses, is therefore enlarged all the way. When the image strikes the phosphor screen, light is generated, and this allows the user to see the image. The image contrast is determined by the number of electrons transmitted through the sample. The darker areas of the image represent areas where fewer electrons are transmitted while the lighter areas of the image represent areas where more electrons were transmitted through the sample. Optional objective apertures can be used to enhance the contrast by blocking out high-angle diffracted electrons.

In this study, the size and shape of the particles were visually determined from transmission electron microscopy (TEM) images.

4.2.2. X-ray diffraction (XRD)

X-ray diffraction (XRD) patterns are the diffraction peaks produced by constructive interference of a monochromatic beam of x-rays diffracted at specific angles from each set of lattice planes in a sample. The peak intensities are determined by the distribution of atoms within the lattice, making the XRD patterns the fingerprint of the periodic atomic arrangements. The angle of diffraction for a given wavelength can be obtained from Bragg's law, as seen in **Fig. 4.3**.
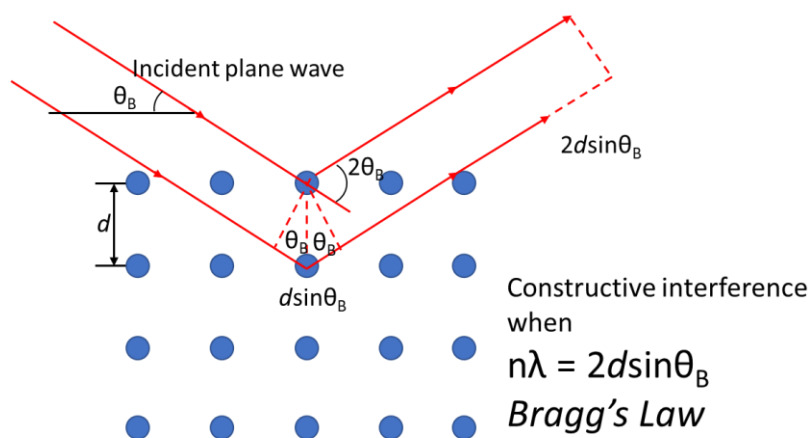
Fig. 4.3 Schematic diagram showing the geometry of the x-ray diffraction technique and Bragg's law.

In Bragg's law equation, n is the order of reflection, λ is the wavelength of the x-ray, d is the spacing between the lattice planes, and θ_B is the angle of incidence that the incident x-ray makes with the plane of atoms, indexed with the Miller indices as (*hkl*). The angle at which a beam of a given wavelength is diffracted by a given set of lattice planes is determined by the crystal system to which the crystal belongs and to its lattice parameters.

For the case of a simple cubic crystal, the lattice vectors are orthogonal and of equal lengths. In this case the spacing d between (*hkl*) lattice planes is given as d_{hkl}, and relates to the lattice constant a ($= b = c$) as

$$d_{hkl} = \frac{a}{\sqrt{h^2 + k^2 + l^2}}$$

(4.2).

For a tetragonal crystal, the lattice parameters a ($= b$) and c are

$$d_{hkl} = \frac{a}{\sqrt{h^2 + k^2}} + \frac{c}{\sqrt{l^2}}$$

(4.3).

In this study, the crystalline structure determination and the lattice distortion analysis were performed from the XRD patterns analysis. From the XRD patterns indexed with the respective (*hkl*) reflections, the degrees of lattice strain *c/a* of the tetragonally distorted samples were calculated from the interplanar spacings d and lattice constants a and c. In the case of tetragonal spinel ferrites, the respective reflections which determine the a and c axes are the (004) and the (220) reflections around $41 < 2\theta$ (deg.) < 44. The tetragonality is defined as $\chi = c/a - 1$ (%)

4.2.3. Vibrating Sample Magnetometer (VSM)

In this study, magnetic measurements were performed using either a vibrating sample magnetometer (VSM) or a VSM-SQUID.

Faraday's law of induction states that a changing magnetic field will produce an electric field. This electric field can be measured to give us information about the changing magnetic field. Many magnetometers including the VSM operates based on this principle.

The sample is placed in the center of the pickup coil under an external magnetic field. While the sample is vibrated at a constant frequency and amplitude, this causes the magnetic flux through the pickup coil to vary accordingly. Maxwell-Faraday's law of induction states that the change of magnetic flux induces a voltage. This induced voltage is proportional to the sample's magnetic moment and does not depend on the strength of the applied magnetic field. In a normal VSM, the magnetic moment of the sample is extracted directly from the voltage induced in the pickup coils. In the VSM-SQUID, the pickup coils are connected to a SQUID element that works like a very sensitive current-to-voltage converter and allows measuring indirectly weak magnetic field (signals).

4.3. Fe^{57} Mössbauer Spectroscopy

This section introduces the basic principles of Mössbauer spectroscopy and how we implemented it in this study. Fe^{57} Mössbauer spectroscopy provides a unique means of studying the structural properties by probing the information of Fe nuclei in a given crystal. Particularly for inverse spinel ferrites, the Fe nuclei corresponds to the two types of Fe cations residing in the A and B sites. Zero-field Mössbauer measurements help to determine the valency and the electrical gradient symmetry of the Fe ions in each respective site. In-field Mössbauer measurements give information regarding (i) collinearity of the spins in the A and B sites, and (ii) the quantitative cationic site distribution of Fe in the respective sites. We performed both the zero-field and in-field Mössbauer measurements at room temperature.

4.3.1. Overview

Nuclei in atoms undergo a variety of energy level transitions, often associated with the emission or absorption of a gamma ray. These energy levels are influenced by their surrounding environment, both electronic and magnetic, which can shift or split these energy levels. These changes in the energy levels provide information about the local environment of the atom. Due to the conservation of momentum, a free nucleus recoils during emission or absorption of a gamma ray, with a recoil energy E_R, just like a gun recoils when firing a bullet. The emitted gamma ray has E_R less energy than the nuclear transition, but to be resonantly absorbed it must be E_R greater than the transition energy due to the recoil of the absorbing nucleus. To achieve resonance, the loss of the recoil energy must be overcome in some way. Mössbauer discovered that when the atoms are within a solid matrix (fixed in a lattice), the effective mass of the nucleus is very much greater. The recoiling mass is now effectively the mass of the whole system, making E_R very small. If the gamma-ray energy is small enough, the recoil of the nucleus is too low to be transmitted as a phonon, and so the whole system recoils, making the recoil energy practically zero; a recoil-free event. In this situation, if the emitting and absorbing nuclei are both in a solid matrix, the emitted and absorbed gamma-ray are the same energy.

4.3.2. Hyperfine interactions

The local information obtained at the nuclear sites includes the electron density, electrical field gradient, and the internal magnetic field. All of these are the result of interactions between the nucleus and the surrounding electrons, known as the hyperfine interactions.

a) Isomer Shift (*I.S.*)

The isomer shift arises due to the electron monopole interaction between the nuclear charge density and the surrounding *s*-electrons. This leads to a monopole interaction, altering the nuclear energy levels. Any difference in the *s*-electrons between the source and the absorber thus produces a shift in the resonance energy of the transition. This shifts the whole spectrum depending on the s-electron density and sets the centroid of the spectrum. As the shift cannot be measured directly, it is quoted relative to a known absorber. For the Fe^{57} Mössbauer spectra, the isomer shifts are always quoted relative to α-Fe (metal) at room temperature.

The isomer shift is particularly useful in determining the cationic valency and oxidation states of the probed nucleus. The electron density at the nucleus can be affected directly by the change in the number of bonding electrons in orbitals with *s*-character. It can also be affected indirectly by the screening of the *s*-electrons caused by the *p* or *d* electrons which themselves do not have a finite probability density at the nuclear site. For example, the electron configurations for Fe^{2+} and Fe^{3+} are $3d^6$ and $3d^5$, respectively. Due to the greater screening of the *d*-electrons, the Fe^{2+} ions effectively have less *s*-electrons at the nucleus. Therefore, Fe^{2+} ions have larger positive isomer shifts than Fe^{3+} ions. The difference in isomer shifts makes it possible to distinguish between Fe^{2+} and Fe^{3+} in compounds such as magnetite where both are present in the same sublattice.

b) Quadrupole Splitting (*Q.S.*)

A nuclear quadrupole moment is produced by the non-spherical charge distribution of nuclei in states with an angular momentum quantum number $I > 1/2$. The presence of an electrical field gradient from asymmetrical electronic charge distribution splits the nuclear energy levels and gives rise to the quadrupole splitting (*Q.S.*). This interaction generates multiple line spectra and can give information about the charge symmetry around the probed nucleus. The magnitude of *Q.S.* obtained from Mössbauer spectroscopy may characterize the charge

distribution and/or the symmetries of the electronic charge distribution. For the highly symmetrical cubic crystals, the electronic charge is symmetrical and evenly distributed, and thus the *Q.S.* gives a zero value.

c) Internal field/Hyperfine field (H_{hf})

Hyperfine field, or magnetic hyperfine interaction, is the result of the interaction between the nucleus and the local magnetic field. It is present even in the absence of an external field, so it is sometimes called the internal field. The origin of the hyperfine field in a 3*d*-cation is mostly from the polarization of the electron spins at the nuclear site (*s-d* coupling) [55]. The schematic diagram of the electron density in the respective *s*- and *d*- shells are plotted against their respective distances from the nucleus (**Fig. 4.4**). Mainly, the 1*s*- and 2*s*-electrons are distributed at the nucleus, and thus one may think that the internal magnetic field is contributed to by the *s*-electrons. However, if the up spins and down spins of the *s*-electrons at the nuclear sites are distributed evenly in the spherical *s*-electron shells, then theoretically there should be no net magnetization nor any magnetic fields at the

Fig. 4.4 Schematic diagram of *s-d* coupling; the origin of the internal hyperfine field.

nucleus. Nonetheless, large internal fields have been observed, which suggests that the internal field does not originate exclusively from the *s*-electrons. Although the *d*-electrons are not located at the nucleus, strong exchange interactions between the up spins of the *d*-electrons and the *s*-electrons produce polarization of the up and down spins of the *s*-electrons at the nuclear sites. This results in a net magnetic field which acts opposite to the external field, and that measured for α-Fe at room temperature is-33 T [56].

4.3.3. Mössbauer spectra and the line intensity ratio

For the 14.4 keV transition of ^{57}Fe, the energy levels of the ground state, $I = 1/2$ and the first excited state, $I = 3/2$ split into 2 and 4 levels, respectively, due to Zeeman splitting. The magnetic splitting of the nuclear energy levels is shown in **Fig. 4.5**. According to the selection rules, the transitions are limited only for a change in magnetic quantum number, $m = 0, \pm1$. Therefore, a ferromagnetic sample such as α-Fe will generate a sextet line in the Mössbauer spectrum. We denote absorption lines with the respective transitions as:

$I_{1,6}$ for $\pm3/2 \rightarrow \pm1/2$ transition denotes the outermost absorption lines (first and sixth peaks)
$I_{2,5}$ for $\pm1/2 \rightarrow \pm1/2$ transition denotes the middle absorption lines (second and fifth peaks)
$I_{3,4}$ for $\pm1/2 \rightarrow \mp1/2$ transition denotes the innermost absorption lines (third and fourth peaks)

Given that Φ is the angle between the incident γ-ray and the magnetization vector, the ratio of the line intensities of the outer $I_{1,6}$, middle $I_{2,5}$ and inner $I_{2,3}$ transitions is given as [55]:

$$3 : \frac{4\sin^2\Phi}{1 + \cos^2\Phi} : 1$$

(4.4).

Equation (4.4) shows that the outer $I_{1,6}$ and inner $I_{3,4}$ lines are always in the same proportion, but the middle $I_{2,5}$ lines can vary in relative intensity between 0 and 4 depending upon the angle Φ. In polycrystalline samples with no applied field, this value $\frac{4\sin^2\Phi}{1+\cos^2\Phi}$ averages to 2. In single crystals and/or under applied fields where the magnetization direction is defined, the relative intensities of the $I_{2,5}$ absorption lines can give information about moment orientation and magnetic ordering. Specifically, if the applied external field is parallel to the gamma-ray, the moment will orient parallel to this direction and the angle Φ becomes 0. Then, the relative intensity of the $I_{2,5}$ absorption lines becomes 0 (**Fig. 4.5**).
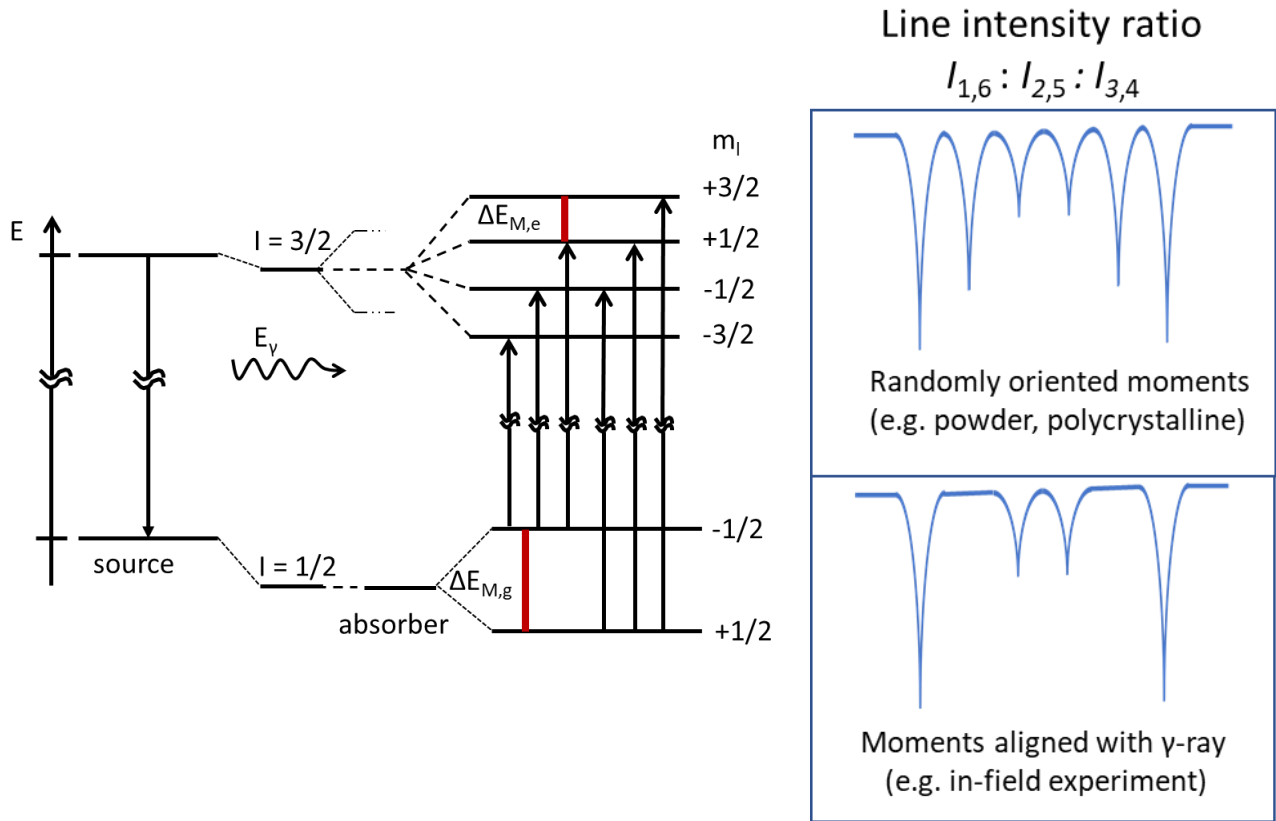
Fig. 4.5 Magnetic splitting of the nuclear energy levels for Fe^{57} and the transitions lines, along with the schematic diagram of the intensity ratio of the transition lines.

4.3.4. Fe site-distribution analysis via in-field Mössbauer spectroscopy

In the Mössbauer spectra of spinel ferrites, there will be two resonance lines originating from Fe residing in the interstitial A and B sites of the compound. The integral of each resonance lines corresponds to the area population of the respective site. Therefore, one can estimate the Fe cationic site distribution from the integrals given that one can distinguish the resonance lines.

However, the problem arises in *M*-doped spinel ferrites because one cannot easily distinguish between the resonance lines from the A and B sites. The reason is that in these compounds, the Fe cations exist in the same trivalent (Fe^{3+}) state in both A and B sites (except for the case of magnetite, Fe_3O_4 where the structure contains Fe^{2+}). This results in the similarity in magnitude of the isomer shifts and hyperfine fields, resulting in the two resonance lines overlapping with each other. To solve this problem, in-field Mössbauer experiments can be useful. Since the moments in the A and B sites are antiferromagnetically coupled, the internal fields are also in opposite directions. By applying an external field parallel to the incidental γ-rays, the magnetic field arising from the majority spin will decrease while that from the minority spin will increase.

Consider H_{ext} to be the external field and H_n the magnetic field measured at the nuclei. The hyperfine fields H_{hf} of Fe cations for each sublattices (A) and (B) may be deduced using the following expressions:

For the majority spin (B site) and minority spin (A site), the hyperfine fields are:

$$H_{hf}(B) = H_n(B) - H_{ext}$$
$$H_{hf}(A) = H_n(A) + H_{ext}$$

(4.5).

Without an applied field ($H_{ext} = 0$), the difference between the two hyperfine fields is simply
$$H_{hf}(B) - H_{hf}(A) = H_n(B) - H_n(A)$$

(4.6).

With an applied field ($H_{ext} > 0$), the difference between the two hyperfine fields becomes

$$H_{hf}(B) - H_{hf}(A) = H_n(B) - H_n(A) - 2H_{ext}$$

(4.7).

The opposite effect given by the external field to the internal fields of the A and B sites produces a difference in the measured hyperfine fields by a magnitude of $2H_{ext}$, which helps to resolve the overlapping resonance lines. Once the overlapping lines are resolved, the integrals of the absorption lines can give quantitative information (i.e. the cation site distribution). It is to note that in the in-field experiments, the intrinsic magnetic and electric properties of the sites are perturbed by the external field. For example, the argument that quadrupole splitting parameter *Q.S.* represents the electrical gradient symmetry is no longer valid when an external field is applied.

4.4. Torque magnetometer
4.4.1. Principle operation

Torque magnetometry is based on the principle that a magnetic field exerts a torque on ferromagnetic samples to align the magnetization with the field. Whenever the magnetization is pulled in a direction other than the easy axis, the anisotropy of the sample tries to pull the magnetization back to the easy axis direction. The force with which this takes place can be measured as the torque, *L*. A simple schematic method is described by Cullity [57]. The sample is attached to a rod hanging on a torsion wire and it is positioned in a magnetic field. A torque force is needed to twist the wire and hence the torque exerted on the sample is proportional to the angle of rotation of the sample. The schematic of the measurement set-up is shown in **Fig. 4.6**.

The sample holder is hung on a thin wire placed in a magnetic field (produced by electromagnets). The sample experiences a torque due to the magnetic field. At the top end of the sample holder, a coil is mounted between permanent magnets of known strength. When a current flow through this compensation coil, the torque on the sample can be compensated by a torque on the coil. The current that passes through the compensation coil is regulated using a small mirror, a lamp and two photo diodes to detect the rotation of the sample. The torque exerted on the sample is measured as it is proportional to the current passing through the compensation coil.
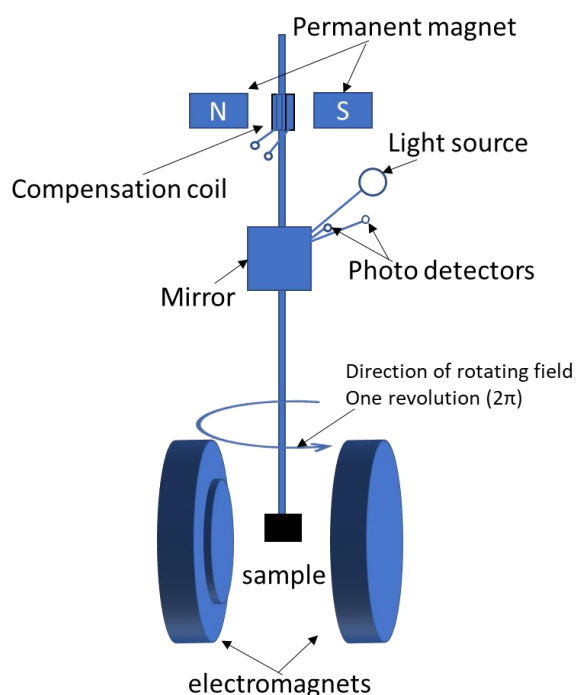

Fig. 4.6 Schematic diagram of a typical torque measurement set-up.

4.4.2. Rotational hysteresis analysis and anisotropy fields

In general, hysteresis loss is caused by irreversible displacement of domain walls and/or irreversible magnetization rotation. The 'normal'/static hysteresis loss obtained with AC measurements using a VSM may contain the contributions of both domain wall displacement and irreversible magnetization. The measurement of rotational hysteresis loss is useful as it separates these two effects. When torque is measured as a function of angle of rotation using a torque magnetometer for polycrystalline or powder specimens, the energy loss resulting from irreversible magnetization rotation appears as a torque opposing the rotation of the sample which results in a hysteresis. In other words, irreversible magnetization processes give a finite value of the integral of torque with respect to the angle of rotation over one revolution given as

$$W_r = - \int L d\theta_T$$

(4.8).

Here, W_r is the rotational hysteresis loss, L is the torque exerted on the sample, and θ_T is the angle of rotation. This value is equal to the energy loss per unit volume of the specimen during one rotation and is called the rotational hysteresis loss.

The rotational hysteresis loss W_r measured using a torque magnetometer is mainly used for estimating the anisotropy field of a magnetic material. The method is referred to as rotational hysteresis loss analysis and the protocols are as follow. First, the torque is measured while changing the field direction with respect to the sample from 0 to 2π. This is usually done by rotating the electromagnets as shown in **Fig. 4.6**. The measurement is done for different values of the field in order to be able to make an extrapolation to infinite field. The idea is that, at the high-field regions, the irreversible magnetization rotation vanishes as the magnitude of the applied field overcomes the anisotropy field. In other words, there will be no hysteresis loss ($W_r = 0$) when the external field is larger than the anisotropy field. If we plot W_r against the reciprocal field $1/H$ and extrapolate the plot to 0, the field where W_r vanishes can be approximated as the effective anisotropy field, H_A. This method has been employed to estimate the anisotropy fields of fine powders in magnetic tape [58] and of polycrystalline thin films [59][60]. **Fig. 4.7 (a)** shows an example of a W_r versus applied field H plot of a magnetic tape taken from a commercial floppy disk. The applied field is varied from 0.02 T to 1.75 T. By plotting W_r against the reciprocal field, the anisotropy field H_A is estimated to be around 0.73 T (**Fig. 4.7(b)**).

In this study, rotational hysteresis loss analysis was used to determine the anisotropy field and the anisotropy constant of the prepared powder samples. Torque measurements were performed using a torque magnetometer (TRT torque magnetometer from Toei Kogyo, Tokyo) with the external magnetic field varied from 0.01 T to 1.5 T. The measurement set-up is similar to that shown in **Fig. 4.6**. The sample was fixed while the external magnet was rotated from -10 to $370\degree$ clockwise and anti-clockwise, and the torque exerted on the sample is measured by a galvanometer placed on top of the rod which is attached to the sample.
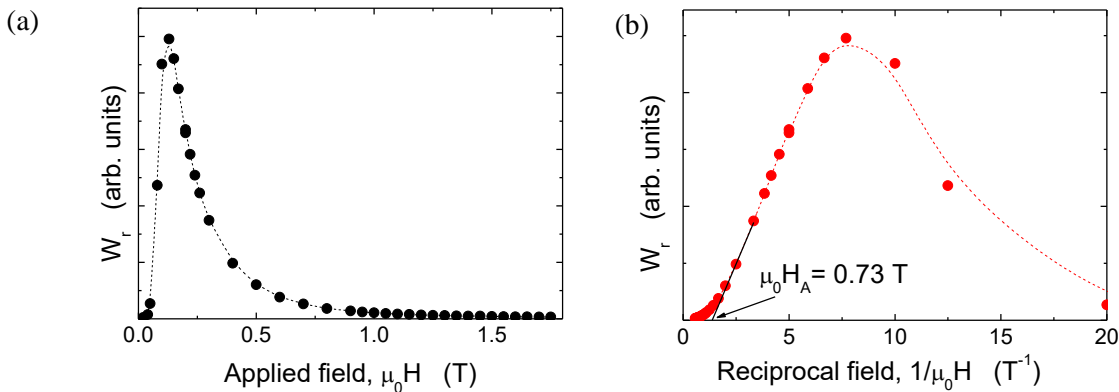
Fig. 4.7 Example of the rotational hysteresis W_r plot of a commercial floppy disk (aligned magnetic nanoparticles). W_r is plotted against (a) the applied field μ_0H; and (b) the reciprocal field $1/\mu_0H$.

4.5. Measurement protocols for coercivity analysis
Magnetic viscosity measurement and size of activation volume

Magnetic viscosity measurements are performed to derive the activation volume v_a used in the global model analysis (section 3.5) [48][47]. In the thermal fluctuation state discussed in the said model, the system is in a metastable state separated from lower energy states. When the energy barriers became of the same order of magnitude as the thermal energy, thermal activation will contribute to magnetization reversal. The magnetic viscosity coefficient S_v can be accessed experimentally from the following relation

$$S_v = \frac{S}{\chi^{\text{irr}}}$$

(4.9).

Here, S is the magnetic viscosity given as

$$S = \frac{dM}{d\ln t}$$

(4.10).

For magnetic viscosity measurements, the sample is first saturated under a magnetic field of 2 T in a positive direction, then a demagnetizing field ($-H_i$), the value of which is near the coercive field, is applied. The magnetization is measured for a duration of typically 30 min, under the constant applied field, $-H_i$. Such measurements were performed at several temperatures.

During thermal activation, only the irreversible changes of the M with respect to the applied field is considered. The irreversible magnetic susceptibility, χ^{irr} is given as

$$\chi^{\text{irr}} = \chi^{\text{tot}} - \chi^{\text{rev}}$$

(4.11).

where χ^{tot} is the total susceptibility and χ^{rev} is the reversible susceptibility. χ^{rev} characterizes magnetization changes associated with magnetic moments that rotate back to their initial position once the applied field is reduced zero. Experimentally, χ^{rev} can be determined from the measurement of recoil curves.

The measurement protocols are similar to the magnetic viscosity measurement, except this time we are measuring the field-dependent magnetization. The sample is first saturated under a magnetic field of 2 T in a positive direction, then a demagnetizing field near $-H_i$ the coercive field is applied. The field is then brought back to zero, and the magnetization is measured as a function of magnetic field to get the demagnetizing recoil curves. Like the magnetic viscosity, the recoil curves are also measured for several $-H_i$ values at several temperatures.

Finally, the magnetic viscosity S_v is determined by comparing the two parameters S and χ^{irr}. The activation volume is then calculated from the expression

$$v_a = \frac{k_B T}{\mu_0 M_s S_v}$$

(4.12).

For magnetization reversal due to thermal activation, the size of the activation volume is expected to be independent of $-H_i$.

5. Structural and magnetic properties of (Cu,Co)-ferrite particles

This chapter describes the basic structural and magnetic properties of the (Cu,Co)-ferrite particles synthesized via the coprecipitation and flux methods. The structural properties were analyzed by TEM, XRD and Mössbauer spectroscopy, whereas the magnetic properties reported in this chapter were measured using a VSM under a maximum applied field of 1.3 T.

5.1. Structural analysis: XRD and TEM
5.1.1. Effect of heat treatment on the tetragonalization of $CuFe_2O_4$ particles

Figure 5.1 (a) shows XRD patterns of as-fluxed $CuFe_2O_4$ particles. The crystal structure was that of a cubic spinel with some traces of CuO as a secondary phase. These particles were subsequently heat-treated in air at 700 – 900 °C, followed by furnace cooling. The XRD patterns of the resulting particles are shown in **Fig. 5.1 (b) – (d)**. Cubic-tetragonal transformation is observed for an annealing temperature, $T_A = 700 – 800$ °C and a single-phase tetragonal spinel structure is obtained when $T_A = 900°C$. For the single-phase tetragonal sample, the lattice distortion due to the JT effect was estimated to be $c/a = 1.056$, in excellent agreement with the value for bulk $CuFe_2O_4$ ($c/a = 1.056$) [34]. High temperature XRD spectra recorded while slow cooling the $CuFe_2O_4$ from 900 °C to room temperature ($-5°C/min$) are shown in **Fig. 5.2**. The cubic-tetragonal phase transition is observed at approximately 370°C, which is similar to the transition temperature reported for bulk $CuFe_2O_4$ ($T_P \sim 360°C$) [33]. **Fig. 5.1 (e)** shows the XRD patterns for $(Cu,Co)Fe_2O_4$ particles after heat treatment at 900 °C for 2 h. The amount of substituted cobalt was 10% of the total number of copper and cobalt ions. All peaks can be attributed to the tetragonal spinel phase, which indicates that both Co and Cu were completely substituted in the spinel structure.

TEM images of as-fluxed (cubic) and heat-treated (tetragonal) $CuFe_2O_4$ and $(Cu,Co)Fe_2O_4$ are shown in **Fig. 5.3 (a) – (d)**. We observed two different length scales for the as-fluxed particles, corresponding to individual crystals (primary particles with estimated average size 50 nm) and to agglomerates of such particles. The difference in the two length scales is attributed to the two independent synthesis processes, i.e. coprecipitation and flux method.

After coprecipitation, the particles obtained were in the range of 10 nm, we call these the primary grains. When the primary grains were mixed in the KBr flux, they tend to agglomerate within the length scale of the KBr crystals (several microns), we call these micron-sized agglomerates the secondary grains. When the particle / KBr mixtures were heat-treated during flux treatment, two types of growth occur, the first corresponds to the growth of individual primary grains, and the second to the growth of secondary grains. The size of the primary grains of cubic $CuFe_2O_4$ was 100 – 200 nm, and that of the secondary particles about 500 nm. For the cubic $(Cu,Co)Fe_2O_4$, the size of the primary grains was 20 – 50 nm and that of the secondary particles about 500 nm. The decrease in primary particle size with Co addition as compared to that of $CuFe_2O_4$ is possibly due to suppression of grain growth because of the addition of cobalt during coprecipitation (**Fig. 5.3 (a)** and **(c)**).

After flux treatment, these particles were subjected to a heat-treatment to induce tetragonalization (**Fig. 5.3 (b)** and **(d)**). Even though the primary particle size can hardly be distinguished from these images, both $CuFe_2O_4$ and $(Cu,Co)Fe_2O_4$ primary particles had grown to sub-micron size upon being heat-treated at 900 °C, considering that aggregation and sintering are likely to occur due to the high heating temperature.
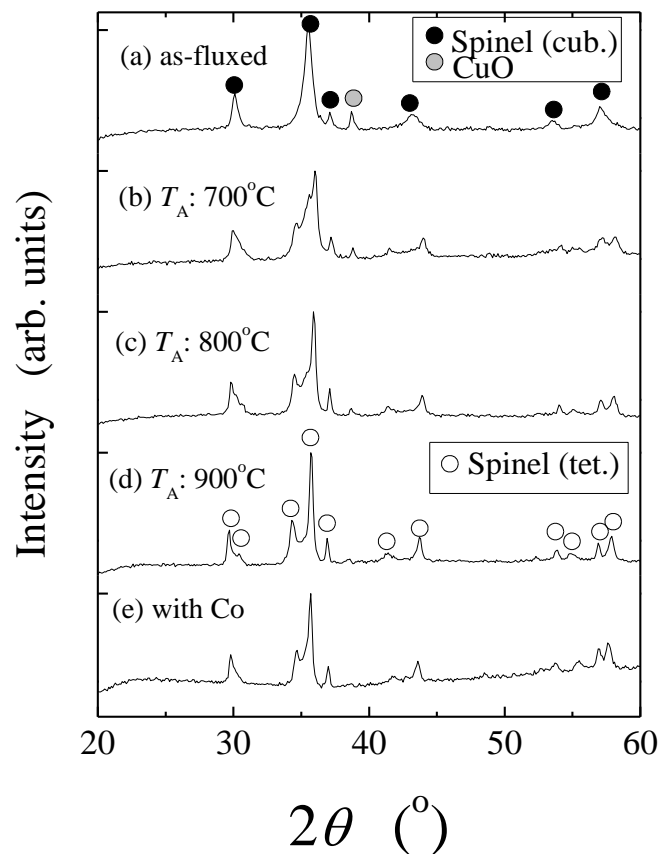
Fig. 5.1. XRD patterns of the (a) $CuFe_2O_4$ particles after flux-treatment, black markers represent the peaks attributed to the cubic spinel phase whereas grey markers represent those of the cupric oxide (CuO) phase. (b)–(d) $CuFe_2O_4$ particles after heat-treated at 700–900 °C, white markers represent the peaks attributed to the tetragonal spinel phase. (e) $(Cu,Co)Fe_2O_4$ particles after heat-treated at 900 °C.
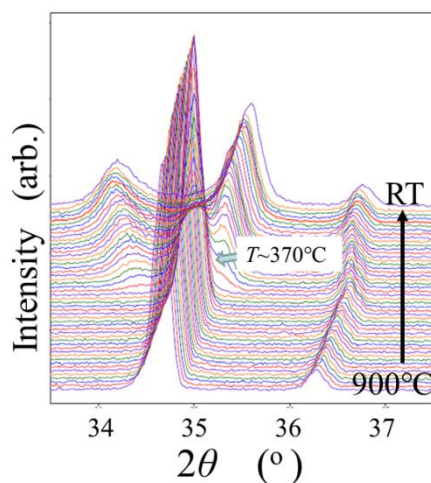
Fig. 5.2. High-temperature XRD patterns of $CuFe_2O_4$ particles recorded from 900 °C, slowly cooled to room temperature (-5 °C/min.). The main (311) peak at $2\theta = 34.8$ (deg.) splits into the (103) and (211) peaks at $2\theta = 34.7$ (deg.) and $2\theta = 35.8$ (deg.), respectively, as the cubic phase transformed into the tetragonal phase.
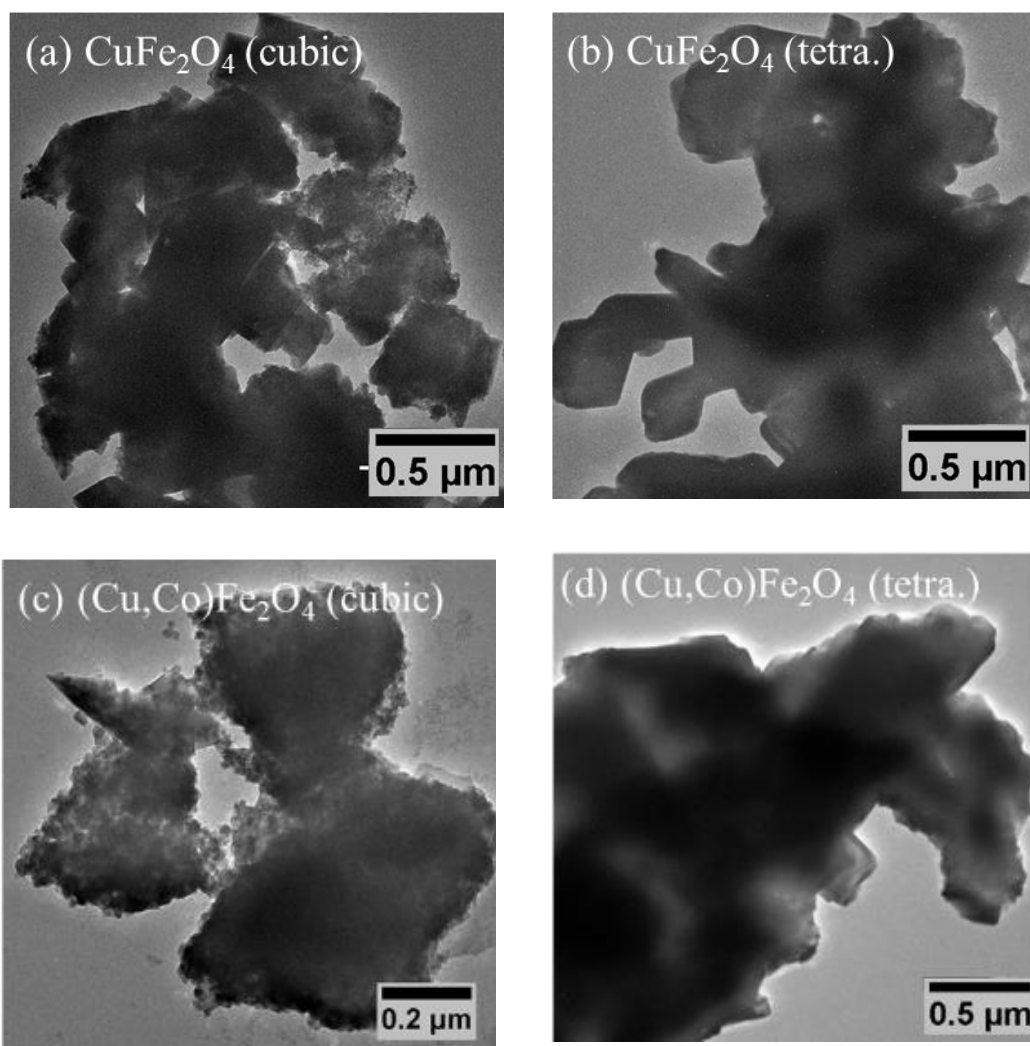
Fig. 5.3. TEM images of the cubic and tetragonal $CuFe_2O_4$ particles (panels (a) and (b), respectively); and the cubic and tetragonal $(Cu,Co)Fe_2O_4$ particles (panels (c) and (d), respectively).

5.1.2. Effect of Co content on the tetragonality

The XRD patterns of the heat-treated $Cu_{1-x}Co_xFe_2O_4$ ($x = 0 - 0.2$) samples are shown in **Fig. 5.4** (a). Distinct tetragonal distortions are confirmed in the $x = 0 - 0.1$ samples. Asymmetrical cubic peaks observed when $x = 0.15$ suggest a mixed phase of the cubic and tetragonally distorted spinel structures. Symmetrical cubic peaks observed when $x = 0.2$ indicates the absence of a cooperative JT distortion. The degree of lattice strain, c/a is

calculated from the interplanar spacings and lattice constants evaluated from the (004) and the (220) reflections around $41 < 2\theta$ (deg.) < 44. The tetragonality, defined in Chapter 4, as $\chi = c/a - 1$, is shown in **Fig. 5.4** (b). Since the Cu and Co content are varied simultaneously, the Cu content decreases with increasing x. As we have reviewed in Section 2.3, the cooperative JT effect is very sensitive to the critical composition of the JT ion, i.e. Cu^{2+}. Therefore, the decrease in Cu content with increasing Co content x results in the reduction of the tetragonality due to the suppression of the cooperative JT effect.
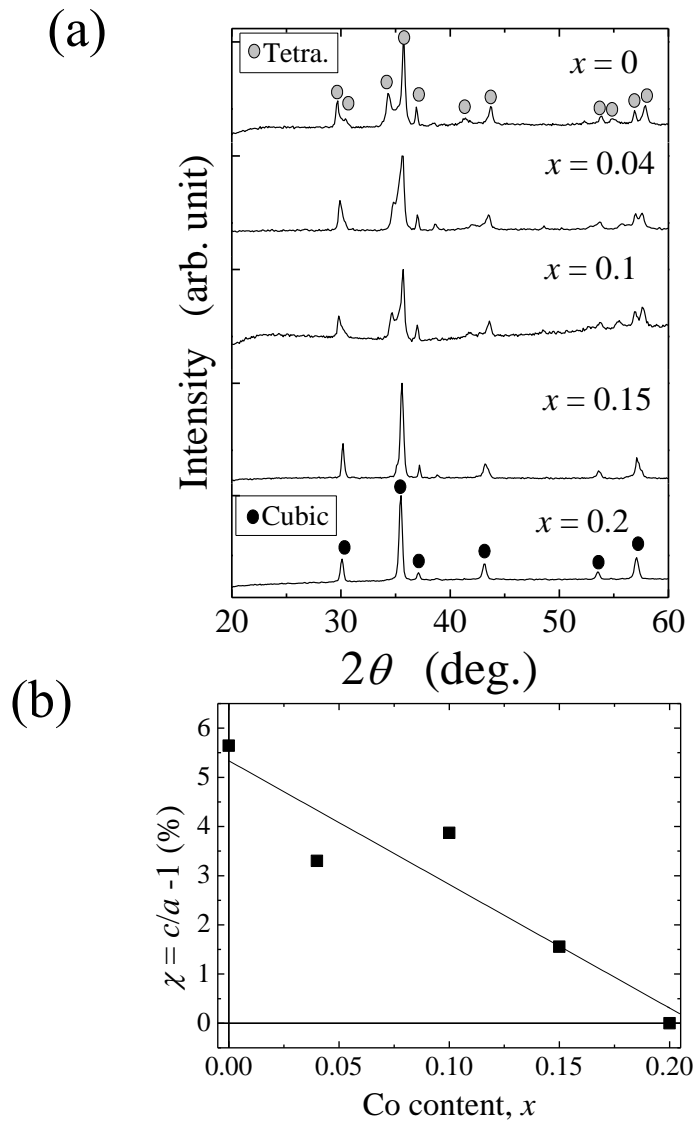
Fig. 5.4 (a) XRD patterns of the $Cu_{1-x}Co_xFe_2O_4$ particles. Black markers represent the peaks attributed to the cubic spinel phase whereas grey markers represent those of the tetragonal spinel phase. (b) Tetragonality χ shows a decreasing tendency due to the suppression of the JT effect with increasing Co content.

5.2. Mössbauer spectroscopy

Zero-field and 5 T in-field ^{57}Fe Mössbauer analysis were performed on two representative $Cu_{1-x}Co_xFe_2O_4$ samples, which are the $CuFe_2O_4$ ($x = 0$) and the $Cu_{0.9}Co_{0.1}Fe_2O_4$ ($x = 0.1$) particles, to determine the Fe site distribution and estimate the amount of anti-site defects. The Mössbauer spectra were recorded at room temperature and they were fitted using the program MossWin Ver. 4 [61] with the velocity and isomer shift calibrated relative to α-Fe foil. For the in-field experiments, the external field was applied parallel to the incident γ-rays. The fitting parameters, including the isomer shift ($I.S.$), hyperfine field (H_{hf}), quadrupole splitting ($Q.S.$), and line width ($L.W.$) are tabulated in **Table 5.1** and **Table 5.2**, for the two samples, respectively. The literature values of H_{hf}, $I.S.$, $Q.S.$, of bulk tetragonal $CuFe_2O_4$ are summarized in **Table 5.3**.

5.2.1. CuFe₂O₄ particles

Zero-field spectrum

Figure 5.6 (top) shows the zero-field (0 T) Mössbauer spectrum of the tetragonal $CuFe_2O_4$ ($x = 0$) particles. The spectrum was fitted with a combination of two magnetic sextets. The ratio of the line intensity $I_{1,6}:I_{2,5}:I_{3,4}$ is 3:2:1, which is a classical value for polycrystalline materials (as described in Section 4.3). The isomer shifts $I.S.$ of the A and B sites' sub-spectra were 0.26 mm/s and 0.36 mm/s, respectively, which are very close to the values reported by Janicki et al., which were 0.28 mm/s and 0.36 mm/s, respectively [62]. The non-zero value of $Q.S.$ observed in the Fe^{3+}(B) resonance of the zero-field spectrum indicates a non-cubic electrical gradient at the local environment of the octahedral B site. This is evident from the global distortion observed from the XRD patterns. Although the JT distortion is produced by the octahedral Cu^{2+}, it is a cooperative effect and thus consequently the octahedral Fe^{3+} must also be distorted, giving a finite value of the local quadrupole splitting. The hyperfine fields obtained for the respective sub-spectra were 47.9 T and 50.7 T, respectively, whereas the corresponding literature values are 48.6 T and 50.7 T. Thus, within experimental error, our zero-field spectrum exhibits relatively good agreement with the reported values.

From the fitting parameters of the zero-field spectrum, the area populations of the two types of Fe^{3+} ions distributed in the A and B sites were 38.1% and 61.9%, respectively. If we assume that the two Fe ions of the $CuFe_2O_4$ are distributed according to this ratio, the respective quantities of Fe ions in A and B sites are,

$$\text{A-site: } Fe^{3+}_{0.742}$$
$$\text{B-site: } Fe^{3+}_{1.258}$$

Therefore, given the cationic configuration as {Asite}[B site], the cationic distribution can be written as

$$\{Fe^{3+}_{0.742}Cu^{2+}_{0.258}\}[Fe^{3+}_{1.258}Cu^{2+}_{0.742}]O^{2-}_4$$

This corresponds to a mixture of inverse and normal spinel configurations, with an anti-site defect of about 26%. This is close to the critical value (25%) for the cooperative JT effect to occur. Thus, this configuration with 26% of anti-site defects is likely, given that we have observed the cooperative JT effect from the XRD patterns.

From this configuration, we can calculate the net molecular moment and get

$$|+\{(0.742 \times 5) + (0.258 \times 1)\} - [(1.258 \times 5) + (0.742 \times 1)]| \approx 3.06 \ \mu_B.$$

The experimental value, which is approximately 1.3 μ_B (27 Am^2/kg), is much smaller. This would suggest that the estimated cationic distribution is inaccurate. The origin of this deviation is attributed to the inaccurate spectral fitting from the overlapping of the A and B sites' resonance lines.

In-field spectrum

To solve the problem of the overlapping A and B sites' spectra, we employed in-field Mössbauer experiments. For the in-field experiments, we will not discuss the $I.S.$ and $Q.S.$ parameters because the effect of applying external field would have perturbed these parameters.

Figure 5.6 (bottom) shows the in-field (5 T) Mössbauer spectrum of the tetragonal $CuFe_2O_4$ ($x = 0$) particles. One can clearly observe that the overlapping spectra was resolved into two distinguished resonance lines. The spectrum was fitted with a combination of two magnetic sextets. This time however, the ratio of the line intensity $I_{1,6}:I_{2,5}:I_{3,4}$ became 3:0:1. What does this mean?

We recall that the relative intensity of the 2-5 absorption lines, $I_{2,5}$ depends on the angle Φ between the

incident γ-rays and the magnetization vector. The line intensity ratio of the outer $I_{1,6}$, middle $I_{2,5}$ and inner $I_{2,3}$ transitions, $I_{1,6}$:$I_{2,5}$:$I_{3,4}$, is given:

$$3 : \frac{4\sin^2\Phi}{1 + \cos^2\Phi} : 1$$

Since the external field is applied parallel to the incident γ-rays, the effective moments originating from spins in the B sites (majority spins) will orient in this direction so that the term $\sin^2\Phi$ become 0. The reduction of the relative intensity of $I_{2,5}$ thus indicates the collinearity of the spins in the A and B sites, as suggested in Néel's model [63][9]. If however, the relative intensity of $I_{2,5}$ is non-zero, then another model regarding the spin arrangement must be considered; such as the spin canting model proposed by Yafet and Kittel [14].

The resolved sub-spectra of the A and B sites give a more accurate spectral fit and area populations of the respective lines. From the fitting parameters of the in-field spectrum, the area populations of the two types of Fe^{3+} ions distributed in the A and B sites were 46.3 % and 53.7%, respectively. If we assume that the two Fe ions of the $CuFe_2O_4$ are distributed in this ratio, the respective quantities of Fe ions in A and B sites are,

A-site: $Fe^{3+}_{0.926}$

B-site: $Fe^{3+}_{1.074}$

Therefore, given the cationic configuration as {Asite}[B site], the cationic distribution can be written as

$$\{Fe^{3+}_{0.926}Cu^{2+}_{0.074}\}[Fe^{3+}_{1.074}Cu^{2+}_{0.926}]O^{2-}_4$$

This configuration corresponds to a near stoichiometric copper ferrite which is fully inverse, where the ratio of Fe ions in the A and B sites is 1:1.

From this configuration, we calculate the net molecular moment and get

$$|\{(0.926 \times 5) + (0.074 \times 1)\} - [(1.074 \times 5) + (0.926 \times 1)]| \approx 1.6 \, \mu_B.$$

This value is in much better agreement with the experimental value, 1.3 μ_B (27 Am^2/kg) compared to that estimated from the zero-field fitting parameters described previously. Furthermore, the estimated amount of anti-site defects is less than 10%, which obviously did not contribute to the suppression of the JT effect.
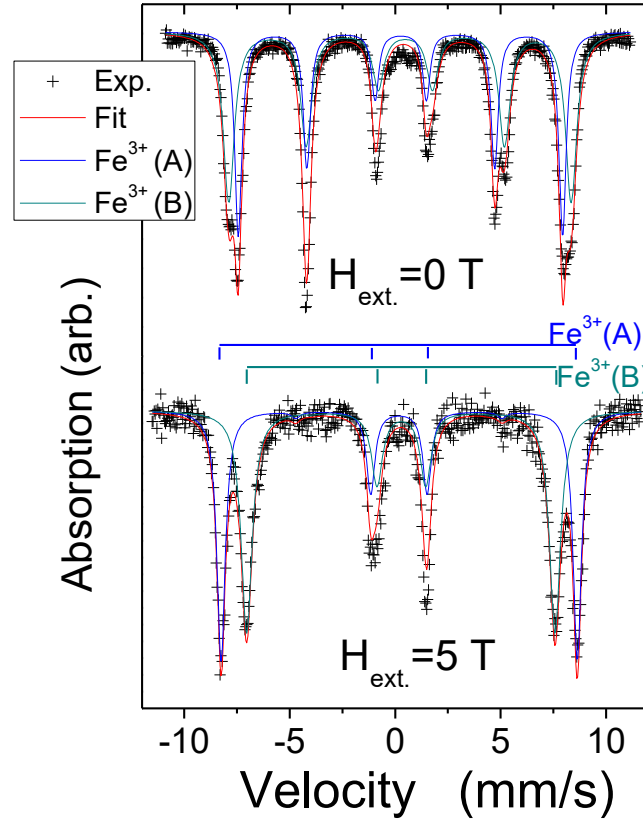
Fig. 5.5. Room temperature ^{57}Fe Mössbauer spectra of tetragonal $CuFe_2O_4$ particles without external magnetic field (top) and with a 5 T external magnetic field applied along the direction of the incident γ-rays (bottom). Solid lines show the results of the fit (see **Table 5.1**).

Table 5.1 Mössbauer parameters for the spectra in **Fig. 5.5**

B_{ext} (T)	Line spectrum	B_{hf} ± 0.03 (T)	I. S.[a] ± 0.01 (mm/s)	Q. S. ± 0.01 (mm/s)	L. W. ±0.01 (mm/s)	Area (%)
0	Fe^{3+} (A)	47.9	0.26	−0.02	0.473	38.1
	Fe^{3+} (B)	50.7	0.36	−0.28	0.412	61.9
5	Fe^{3+} (A)	52.5	0.19	0.01	0.479	46.3
	Fe^{3+} (B)	45.4	0.28	−0.02	0.635	53.7

[a] Relative to room temperature α-Fe

5.2.2. $Cu_{1-x}Co_xFe_2O_4$ particles ($x = 0.1$)

Figure 5.7 (top) shows the zero-field (0 T) Mössbauer spectrum of the tetragonal $Cu_{1-x}Co_xFe_2O_4$ ($x = 0.1$) particles. The in-field (5 T) spectrum is shown in **Fig. 5.7** (bottom). Similar to the spectra in **Fig. 5.6**, the 0 T and 5 T spectra were fitted with a combination of two magnetic sextets.

The ratio of the line intensities shows a similar tendency to that seen in **Fig. 5.6**, where the ratio $I_{1,6}:I_{2,5}:I_{3,4}$ is 3:2:1 for the zero-field spectrum and it becomes 3:0:1 for the in-field spectrum. From the zero-field spectrum, the isomer shifts *I.S.* of the A and B sites' sub-spectra were 0.27 mm/s and 0.36 mm/s, respectively. These values are also similar to those reported by Janicki et al., which were 0.28 mm/s and 0.36 mm/s, respectively [62]. The *Q.S.* also showed non-zero value for the Fe^{3+}(B) line, which indicates a non-cubic electrical gradient at the local environment of the octahedral B site. These results are all similar to those shown in the previous Section 5.2.1. Therefore, we can draw the same conclusions regarding the *I.S., Q.S.* and the collinearity of the spins in the A and B sites for the $x = 0.1$ and $x = 0$ samples. In other words, a 10% substitution of Co does not affect significantly the structural properties of the spinel compound.

In-field spectrum

Next, we try to estimate the cationic distribution of the $x = 0.1$ sample using the area population parameter taken from the in-field spectrum. The area populations of the two types of Fe^{3+} ions distributed in the A and B sites were 43.4 % and 56.7%, respectively. If we assume that the two Fe ions of the $CuFe_2O_4$ are distributed by this ratio, the respective quantity of Fe ions in A and B sites are,

A-site: $Fe^{3+}_{0.868}$
B-site: $Fe^{3+}_{1.132}$

Since the Mossbauer studies only probe the Fe nuclei, the site distribution information is limited to the Fe ions. Although we may not know the direct distribution of Cu and Co, we can assume that on average, they are equally distributed among the A and B sites, so that the cationic distribution can be written as

$$\{Fe^{3+}_{0.868}(Cu,Co)^{2+}_{0.132}\}[Fe^{3+}_{1.132}(Cu,Co)^{2+}_{0.868}]O^{2-}_4$$

This corresponds to a mixture of inverse and normal spinel configurations, with an anti-site defect of about 11%. This amount is safely below the critical value for cooperative JT effect (i.e. 25%) and concludes that the 10% Co substitution did not suppress the cooperative JT effect. Evidently, global tetragonal distortion was confirmed in the XRD patterns.

We assume that the effective magnetic moment of the $(Cu,Co)^{2+}$ is 2 μ_B, which is the average of Cu^{2+} (1μ_B) and Co^{2+} (3μ_B). From the above configuration, we estimate the net molecular moment as follow

$$|\{(0.868 \times 5) + (0.132 \times 2)\} - [(1.132 \times 5) + (0.868 \times 2)]| \approx 2.79 \ \mu_B.$$

The experimental value was approximately 1.5 μ_B (32 Am^2/kg), which is much lower than the estimated value above. This can be expected since the exact cation distribution of Cu^{2+} and Co^{2+} is unknown. Nonetheless, we can consider that the two values did not vary much significantly.
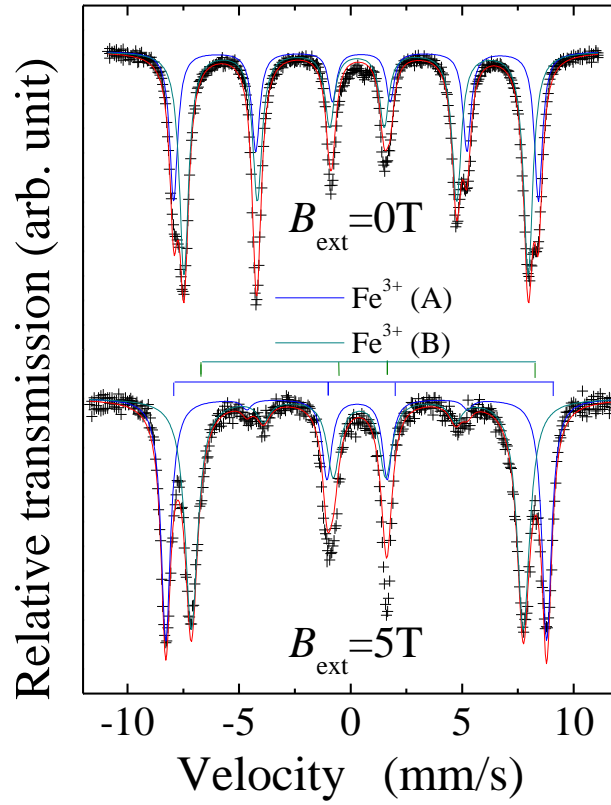
Fig. 5.6 Room temperature ^{57}Fe Mössbauer spectra of the tetragonal $Cu_{1-x}Co_xFe_2O_4$ (x=0.1) sample without external magnetic field (top) and with 5T external magnetic field applied along the direction of the incident γ-rays (bottom). Solid lines show the results of the fit (see **Table 5.2**).

Table 5.2 Mössbauer parameters for the spectra in **Fig. 5.6**

B_{ext} (T)	Line spectrum	B_{hf} ± 0.03 (T)	I. S.[a] ± 0.01 (mm/s)	Q. S. ± 0.01 (mm/s)	L. W. ±0.01 (mm/s)	Area (%)
0	Fe^{3+} (A)	47.99	0.27	-0.04	0.502	63.3
	Fe^{3+} (B)	50.84	0.36	-0.24	0.433	36.7
5	Fe^{3+} (A)	53.10	0.27	-0.04	0.517	43.4
	Fe^{3+} (B)	46.27	0.35	-0.10	0.686	56.7

[a] Relative to room temperature α-Fe

Table 5.3 Summary of Mössbauer fitting parameters for bulk tetragonal $CuFe_2O_4$.

Compound	Line spectra	$H_{h.f.}$ (T)	I. S. (mm/s)	Q. S. (mm/s)	L. W. (mm/s)	Ref
$CuFe_2O_4$	Fe^{3+}/A	48.6	0.28	-0.02	-	[62]
(tetragonal)	Fe^{3+}/B	50.7	0.36	-0.72	-	

5.3. Magnetic properties

Figure 5.7 (a) shows magnetization curves of the samples measured using a vibrating sample magnetometer (VSM) at room temperature under a maximum applied field of 1030 kA/m (13 kOe). The variation of saturation magnetization M_s and coercivity H_c are plotted as a function of x in **Fig. 5.7 (b)**. For the $x = 0$ sample, the M_s was 27 Am^2/kg, and the value increases up to 37 Am^2/kg with x. Since the structure is that of an inverse spinel and the cations are collinear, the increase of M_s with x can be explained by the higher magnetic moment of the Co^{2+} ion (3 μ_B) compared to that of the Cu^{2+} ion (1 μ_B). The coercivity increases from 68.4 kA/m (0.86 kOe) to 175 kA/m (2.2 kOe) when x is increased from 0 to 0.1. Above $x = 0.1$, H_c starts to decline, dropping to a value of 71.6 kA/m (0.9 kOe) when $x = 0.2$.

In the case of cubic cobalt doped spinel ferrite particles [64][21][65], coercivity is often almost directly proportional to the Co concentration. This can be attributed to the octahedral Co^{2+} which enhances the magnetocrystalline anisotropy from the unquenched orbital moment due to the trigonal field [19][20]. In this study, the linear relation between coercivity and Co content does not hold above $x = 0.1$. Since most of the Cu and Co are in the octahedral sites, the main contributing factor to the magnetic anisotropy can be considered to be the octahedral Co^{2+}. In this case then, the variation of coercivity may be due to the added tetragonality factor. The distorted environment created by the Cu^{2+} induces magnetoelasticity at the octahedral Co^{2+} sites, which may be the origin of the higher coercivity in samples with high tetragonality ($x \leqq 0.1$), and the lower coercivity in samples with lower tetragonality ($x > 0.1$). In the next chapter, we will determine the anisotropy and establish the relation between anisotropy and coercivity. We will also discuss in more detail the origin of anisotropy and why the linear relation between coercivity and Co content does not hold above $x = 0.1$.
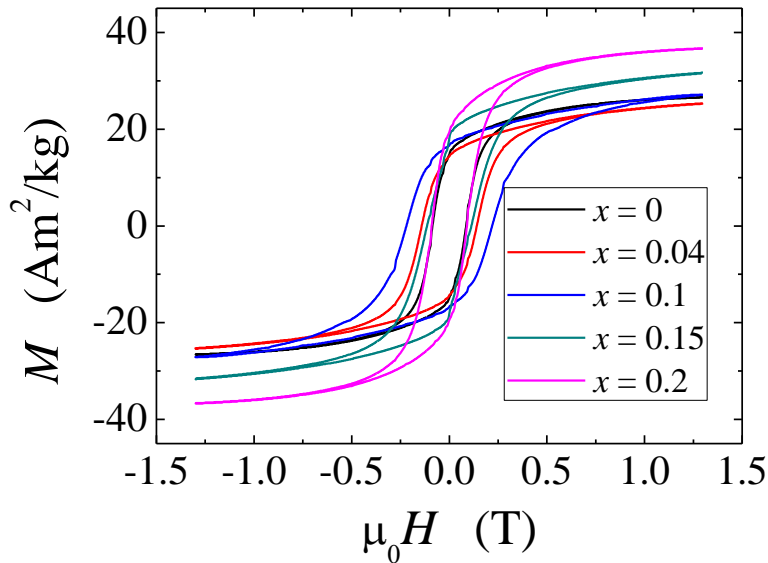
Fig. 5.7 (a) Room temperature magnetization curves of the $Cu_{1-x}Co_xFe_2O_4$ particles (H_{max}=1030 kA/m).

Fig. 5.7 (b) Room temperature saturation magnetization, M_S (closed-circles) and coercivity, H_c (opened-circles) of the $Cu_{1-x}Co_xFe_2O_4$ particles ($H_{max} = 1030$ kA/m).
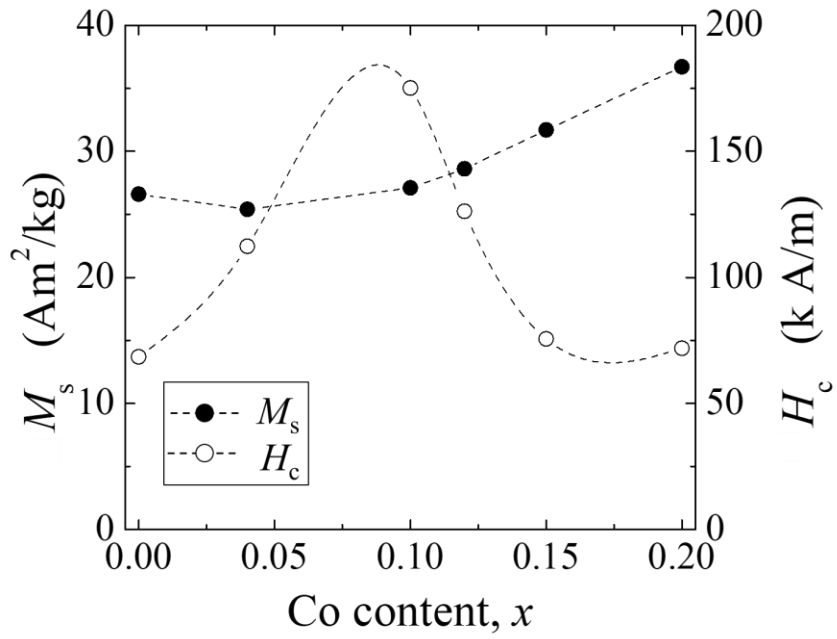
5.4. Conclusions

We synthesized sub-micron sized $Cu_{1-x}Co_xFe_2O_4$ particles via coprecipitation and flux methods and varied the Co content ($x = 0 - 0.2$). The tetragonalization process was performed by annealing the particles at 900°C followed by furnace cooling.

Structural properties

The size of particles obtained showed two different length scales corresponding to the primary and secondary grains, which are approximately of the order of 50 nm and 500 nm, respectively. The latter correspond to agglomerates of the former.

Despite the complex microstructure observed in TEM images, the crystal structure obtained from the XRD patterns for the $CuFe_2O_4$ particles ($x = 0$ sample) showed similar lattice parameters to bulk tetragonal $CuFe_2O_4$, with the lattice distortion estimated to be $c/a = 1.056$. High temperature XRD spectra indicate the transition temperature to be approximately 370°C, similar to that observed for bulk copper ferrite (360°C). The effect of Co substitution on the crystal structure was investigated. XRD patterns revealed that the optimum composition required for single-phase tetragonal distortion or cooperative JT distortion is $x = 0.1$ and below. Above this value, one observes either a mixture of cubic and tetragonal phases, or a single phase of the cubic spinel. Since XRD only provides the long-range order information, i.e. the global distortion, it is unclear if there is any short-range ordered local distortion, i.e. non-cooperative JT distortion occurring between $x = 0.1$ and $x = 0.2$. By analyzing the tetragonality, we observe that the value decreases as the cobalt substitution increases. This is an expected behavior as the increase in Co would mean a reduction in Cu content. Since JT distortion is highly dependent on the concentration of the JT ion, in this case Cu^{2+}, it is only natural that reducing the Cu content would suppress the JT effect.

Zero-field and in-field Mössbauer studies suggest that the magnetic moments in the A and B sites of the spinel compound studied are in a colinear configuration, as proposed in Néel's model of antiferromagnetism. The quadrupole splitting *Q.S.* of the Fe in the octahedral B site showed a non-zero value, which suggests an asymmetric electrical gradient of the interstitial B sites. A similar *Q.S.* value was also reported for bulk tetragonal copper ferrite and we can attribute the anisotropic electrical field to the cooperative JT effect of the octahedral Cu^{2+}. For the $x = 0$ sample, the cationic distribution obtained suggests a near stoichiometric copper ferrite in the fully inverse spinel configuration. On the other hand, for the $x = 0.1$ the cationic distribution obtained suggests a mixture of normal and inverse spinel configurations. The ratio of the normal spinel configuration denoted as the anti-site defects was estimated to be approximately 11% and proved to be small enough not to suppress the cooperative JT effect.

Magnetic properties

From the cationic site distribution estimated via the Mössbauer studies, the calculated net molecular moment was mostly in agreement with the experimental values. By increasing the Co substitution, the saturation magnetization showed a monotonous increase. This is attributed to the larger magnetic moment of the Co^{2+} ions compared to the Cu^{2+} ions. The coercivity on the other hand, showed non-linear behavior with respect to the Co content substitution, x. The value of coercivity increases with x from $x = 0$ up to $x = 0.1$. Above this value, the coercivity tends to decrease. This is contrary to the linear behavior that would be expected in cubic cobalt doped spinel ferrites. We then attribute the irregular behavior of the coercivity to the added tetragonality factor which is not present in the reported cubic cobalt doped spinel ferrites. We propose that the distorted environment created by the Cu^{2+} ions induces the magnetoelasticity of the octahedral Co^{2+} sites. This causes the coercivity to be higher in samples with high tetragonality ($x \leqq 0.1$), and vice versa with the lower coercivity observed in samples with lower tetragonality ($x > 0.1$). We will discuss further regarding this coercivity and/or anisotropy enhancement mechanism in the next chapter.

6. Strain-induced magnetic anisotropy in (Cu,Co)-ferrite particles via the Jahn-Teller distortion

In the previous chapter, we observed that the coercivity of the synthesized (Cu,Co)-ferrite particles were not directly proportional to the Co content, which could have been expected in Co doped spinel ferrites. The origin of the non-linear behavior is attributed to the tetragonality factor, which may affect the anisotropy through magnetoelastic coupling. In this chapter, we discuss the strain-induced magnetic anisotropy of these (Cu,Co)ferrite particles. First, we analyze the magnetic anisotropy from torque measurements and rotational hysteresis loss analysis. Then, using the tetragonality expression obtained from XRD analysis in the previous chapter, we propose a physical model which couples the Jahn-Teller effect and the magnetoelastic effect to explain the magnetic anisotropy of the tetragonal (Cu,Co)-ferrite particles. The uniaxial magnetic anisotropy K_u is described using the phenomenological expression of the magnetoelastic model, $K_u = B_1\chi$. The value of magnetoelastic coupling coefficient B_1 is compared with the calculated and reported values for bulk and thin film cobalt ferrites.

6.1. Magnetic anisotropy analysis
6.1.1. Torque measurements and rotational hysteresis loss (W_r) analysis

The formalism of magnetic anisotropy analysis using torque measurements has been described in Section 4.4. Here, let us recall the main idea of the rotational hysteresis loss W_r analysis. In the absence of external fields, the magnetization vector lies in the easy axis of the magnetization at which the energy E is minimized. This direction is defined by the anisotropy energy of the sample. When an external field is applied in a direction off the easy-axis (e.g. by rotating the external field), the magnetization vector deviates to a new direction at which the torque exerted by the external field balances the torque due to the anisotropy energy. Under a moderately high-field, the competition between the external magnetic field and the internal anisotropy field of the sample results in irreversible processes during the magnetization rotation which are reflected in the rotational hysteresis loss. By measuring the torque of the sample under a rotating external field (forward and backward in one revolution), W_r is defined as 1/2 of the area between the angle dependent torque curves. Measuring the torque curves in various magnetic fields, allows one to plot W_r as a function of the external field. The W_r plot can be extrapolated at the high-field region to find the magnitude of the external field where the hysteresis loss vanishes ($W_r = 0$). Theoretically, this field corresponds to the effective anisotropy field of the sample.

Figure 6.1 shows representative torque curves of the $x = 0.1$ sample measured under a rotating magnetic field of $0.1 - 1.5$ T. Under a relatively low magnetic field (0.1 T), almost no hysteresis loss was observed because the anisotropy energy of the sample is more dominant than the external field. By increasing the field to $0.5 - 1.5$T, hysteresis loss was observed in each case, indicative of the competition between the anisotropy energy and the external field which results in the irreversible magnetization processes. For each value of applied external field, the rotational hysteresis loss W_r was determined by the integrals of the torque curves. In general, the value of W_r is normalized by the volume magnetization of the sample. However, since the exact volumes of the nanoparticle samples are unknown, we performed the normalization with respect to the maximum value of W_r, hence the arbitrary unit of W_r.

The normalized W_r versus the applied external field H plot for the $x = 0 - 0.2$ samples are shown in **Fig. 6.2**. For the $x = 0$ sample, we observed that W_r approaches zero in the high-field region. For the other samples where $x > 0$, W_r remains at finite values even in the high-field region, above 1 T. The non-vanishing W_r suggests that the $x > 0$ samples are characterized by strong anisotropy fields. This can be well understood since the cobalt added samples ($x > 0$) exhibit larger magnetic anisotropy due to the magnetocrystalline anisotropy of Co^{2+} as compared to the pure copper ferrite ($x = 0$) sample. W_r is plotted as a function of the reciprocal field ($1/H$) and the effective magnetic anisotropy fields, H_A are determined by extrapolating the linear part of the high-field region towards 0 (**Fig. 6.3**).

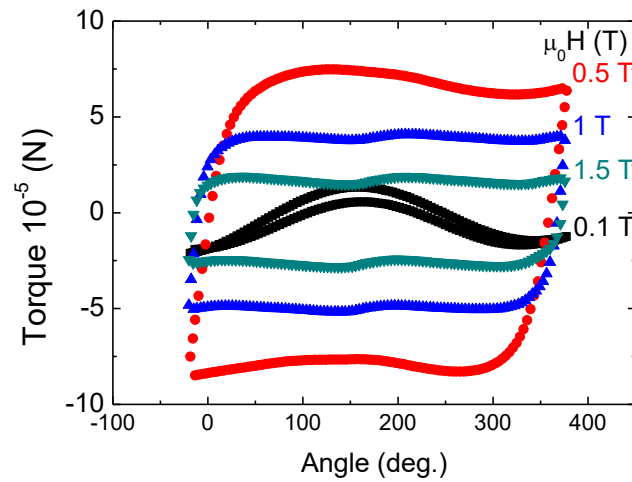**Fig. 6.1** Representative torque curves of the $x = 0.1$ sample measured under a rotating magnetic field of $0.1 - 1.5$ T.
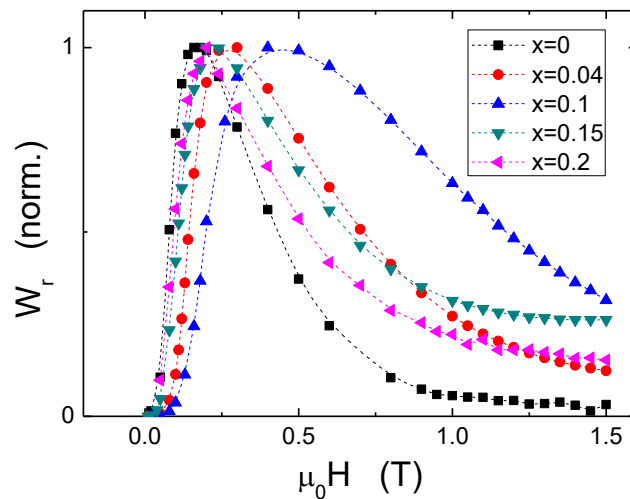

Fig. 6.2 The rotational hysteresis (W_r) plotted against the applied field. Finite values of W_r in the high-field region suggest strong magnetic anisotropy in the Co added $x > 0$ samples.
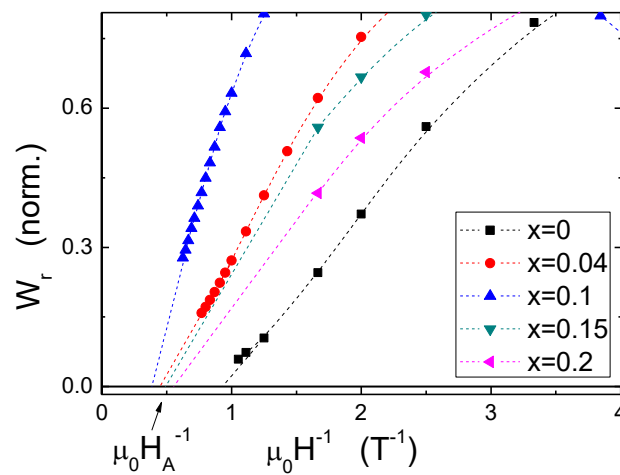
Fig. 6.3 Rotational hysteresis (W_r) versus the reciprocal field (1/H) plot.

6.1.2. Anisotropy fields deduced from W_r analysis

Figure 6.4 shows the estimated anisotropy field plotted as a function of x. The Co content dependency of the anisotropy field is similar to that shown for the coercive field in **Fig. 5.8 (b)**. The anisotropy field tends to increase with x up to $x = 0.1$ and it decreases above this value. By plotting the anisotropy field against the coercivity, one gets the plot shown in **Fig. 6.5**. Note that we found a linear dependence for the Co added samples ($x > 0$). This suggests that Co^{2+} is the main source of anisotropy reflected in both the anisotropy field and coercivity values.

In the case of cobalt doped spinel ferrites, it has been shown experimentally that the anisotropy increases monotonously with Co concentration [65][21]. The one-ion model in cobalt ferrites also suggests that K_1 is dependent on the Co^{2+} ions concentration. In our case however, we did not observe the monotonous increase in the anisotropy fields with x. Why so? We suggest that the magnetic anisotropy may not originate exclusively from the K_1 of Co, but also from the tetragonality factor. The interaction between tetragonal distortion and Co^{2+} may produce magnetoelastic anisotropy which contributed to the total anisotropy. To verify this, the magnetic anisotropy energy K_u is determined from the estimate anisotropy field using the expression $H_A = 2|K_u|/M_s$ and we propose the correlation of K_u with lattice distortion and the magnetoelastic effect of the material.
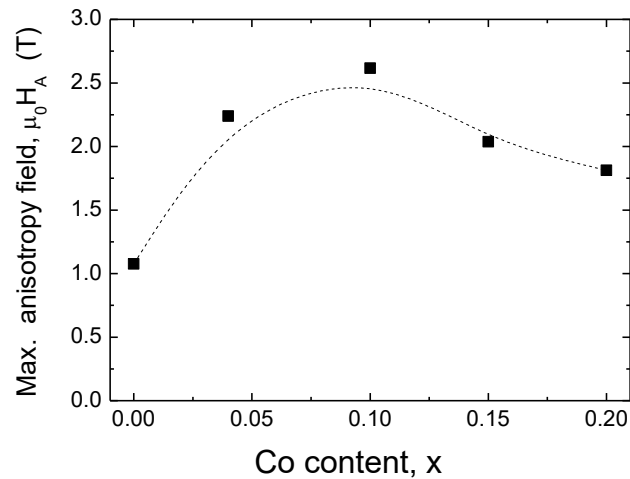
Fig. 6.4 The maximum anisotropy field determined from the W_r analysis, plotted as a function of x.

Fig. 6.5 Anisotropy field vs. coercivity plot showing a linear relation for $x > 0$ samples (closed-circles). This suggests that the coercivities are almost a direct measure of the magnetic anisotropies in this region.

6.2. Magnetoelastic (ME) coupling by the Jahn-Teller effect

Figure 6.6 shows the magnetic anisotropy constant K_u derived from the anisotropy field in **Fig. 6.4**, plotted as a function of the Co content, x. K_u increases progressively up until $x = 0.1$ and then tends to reach a plateau above thi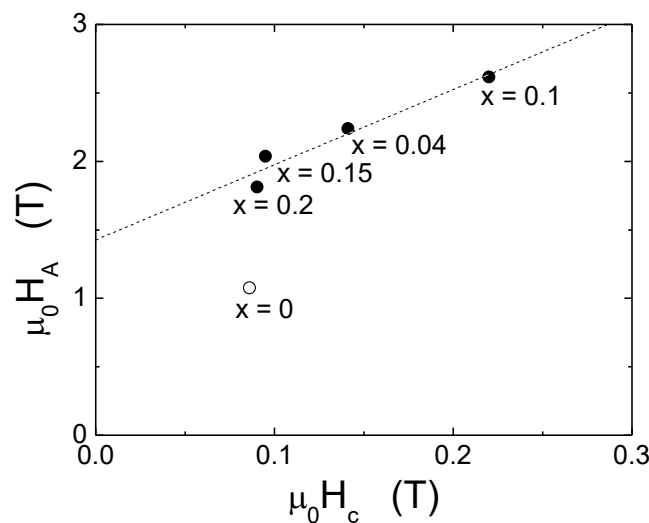s value. This is also an indication that the origin of anisotropy is not exclusive to the K_1 of Co, because otherwise the value of K_u should increase monotonously with x. The other source to be considered is the tetragonality factor, but how do we model that? Using the phenomenological magnetoelastic theory described in Section 2.4, we attempt to explain the variation of K_u as a function of x. We propose the following ME coupling model induced by the JT distortion.

We recall that the magnetoelastic anisotropy energy K_u^{me} is given in eq. (2.12) as

$$K_u^{me} = B_1 \chi$$

(6.1).

where B_1 is the ME coupling coefficient and χ represents the degree of uniaxial lattice distortion, i.e. the tetragonality. Since we want to model the variation of K_u as a function of x, the corresponding parameters on the right-hand side of the eq. (2.12) should also be expressed in terms of x so that

$$K_u(x) = B_1(x)\chi(x)$$

(6.1).

For the tetragonality, the expression of $\chi(x)$ is simple as the JT distortion decreases monotonously with the concentration of Cu, which is inversely related to x. Using the least-square method, the tetragonality obtained in **Fig. 5.4** (b) can therefore be expressed as a linear function of x with a negative slope, such that

$$\chi(x) = -25.1(\pm 5.5)x + 5.34\ (\pm 0.67)$$

(6.2).

However, for the ME coupling coefficient, the expression of $B_1(x)$ is not as simple. Since B_1 is correlated to the magnetostriction parameter λ_{100}, the value depends greatly on the magnetostriction. Co-ferrite is known for its highly magnetostrictive properties with λ_{100} as high as -590 ppm reported at room temperature [24]. Although the order of magnitude is much smaller, magnetostriction was also observed in Cu-ferrite with a reported λ_{100} value of -87 ppm [66]. Therefore, in the case of (Cu,Co)-ferrite particles, we must consider contributions from both Co and Cu to express $B_1(x)$. We consider the total effective contribution B_1^{tot} as

$$B_1^{tot}(x) = B_{1Co}x + B_{1Cu}(1-x)$$

(6.3)

where B_{1Co} and B_{1Cu} are the individual components of magnetoelastic coefficients per unit Co and Cu ion, respectively. We assume that B_1^{tot} can be expressed as a Taylor series and we only consider the lowest order term shown in eq. (6.3). Now, by taking the product of eq. (6.3) and $\chi(x)$, the magnetoelastic model in eq. (6.1) becomes

$$K_u(x) = (B_{1Co} - B_{1Cu})x\chi(x) + B_{1Cu}\chi(x)$$

(6.4).

Equation (6.4) represents the coupling of the JT distortion and the magnetoelastic effect considered for the case of (Cu,Co)-ferrites. Since both B_1^{tot} and χ are linear functions of x, we see that the product of the two parameters gives a quadratic function of x. This is the reason that the measured H_A and K_u values were not simple linear functions of x. To get a linear representative of the measured K_u, we plotted $K(x)$ as a function of $x\chi(x)$, according to eq. (6.4). The result is shown in **Fig. 6.7**. The solid line represents the linear fit for the tetragonally distorted samples. One observes a clear deviation for the cubic $x = 0.2$ sample where $\chi \approx 0$, which indicates that the magnetoelastic model is applicable to tetragonally distorted samples where $\chi > 0$. The linearity strongly suggests that the JT distortion is coupled with the ME effect of Co.
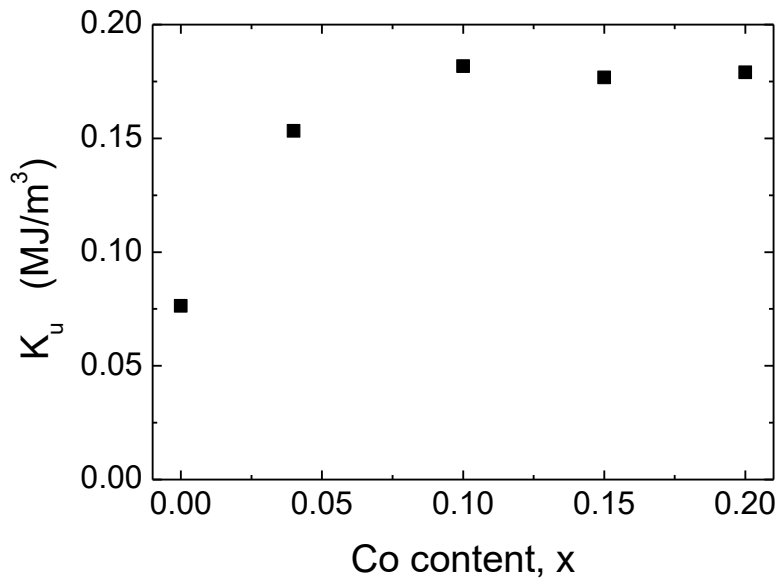
Fig. 6.6 The magnetic anisotropy constant K derived from the anisotropy fields plotted as a function of x.
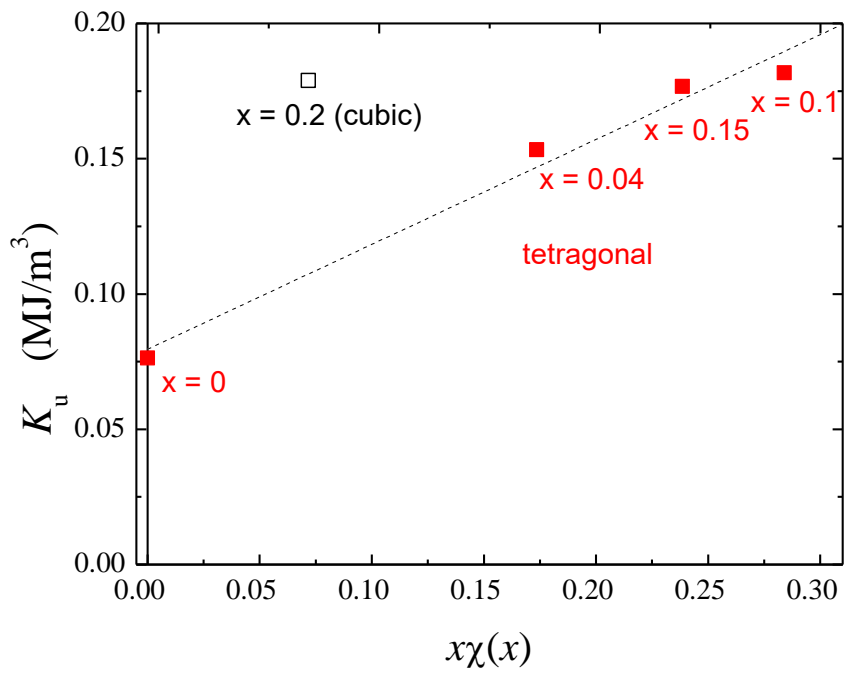

Fig. 6.7 Plot of the experimental K versus $x\chi$, to model the JT distortion and ME coupling. Solid red squares represent tetragonally distorted samples, whereas the empty black square is the cubic $x=0.2$ sample.

6.3. Discussion: Magnetoelastic coupling coefficients of Cu and Co

From **Fig. 6.7**, the linear fit obtained by the least-square method is expressed as

$$K(x\chi) = 38.7(\pm 3.83)x\chi + 7.95(\pm 0.78)$$

$$(6.5).$$

Comparing eq. (6.5) with that in eq. (6.4), the magnetoelastic coefficients of Co and Cu are determined to be $B_{1Co} = 40$ MJ/m^3 and $B_{1Cu} = 1.5$ MJ/m^3, respectively. We compare these values with the ME coupling coefficients calculated for bulk cobalt ferrite and copper ferrite, per unit Co and Cu ions, respectively.

The tetragonality of pure copper ferrite (CuFe$_2$O$_4$) is attributed fully to cooperative JT distortion which can be defined per unit Cu ion. For bulk tetragonal copper ferrite, the reported values of the magnetic anisotropy and tetragonality are $K_1 = 0.2$ MJ/m^3 [67] and $\chi = 5.6$ % ($c/a = 1.056$) [35], respectively. From the magnetoelastic model, $K = B_1\chi$, the B_1 value for bulk tetragonal copper ferrite is calculated to be approximately 4 MJ/m^3, which is close to our estimated B_{1Cu} value, i.e. 1.5 MJ/m^3.

Since bulk cobalt ferrites are generally cubic, the tetragonality is defined as $\chi = 0$. Therefore, the magnetoelastic model equation (as described above) cannot be applied to calculate B_1 of bulk cobalt ferrites. In this case, we can calculate the theoretical B_1 values for bulk cobalt ferrites using the magnetostriction constant λ_{100} and the respective elastic moduli C_{ij}. For a given cubic lattice with uniaxial distortion along the direction [100], the ME coupling coefficient B_1 is given as

$$B_1 = \frac{3}{2}\lambda_{100}(C_{12} - C_{11})$$

$$(6.6).$$

Using the magnetostriction constants λ_{100} reported by Bozorth et al. [24], the theoretical ME coefficients B_1 values are calculated using the elastic moduli $C_{11} = 273$ GPa and $C_{12} = 106$ GPa [68][69]. Since all the samples contain a different amount of Co, it is more realistic to normalize the value per unit Co ion (B_{1Co}) to be compared with our obtained value. The reported λ_{100} values, theoretical B_1 and the normalized B_{1Co} values are summarized in **Table 6.1**.

Table 6.1 List of magnetostriction constants λ_{100} [24] and the corresponding theoretical (B_1) and the normalized ME coefficients (B_{1Co}).

Composition Co$_x$Fe$_{3-x}$O$_4$	$\lambda_{100} \times 10^{-6}$	B_1 (MJ/m^3)	B_{1Co} (MJ/m^3)	Reference
Co$_{0.8}$Fe$_{2.2}$O$_4$	-590	148	180	[24]
Co$_{0.3}$Zn$_{0.2}$Fe$_{2.2}$O$_4$	-210	53	160	
Co$_{1.1}$Fe$_{1.9}$O$_4$	-250	60	55	

From the calculated B_{1Co}, we observe quite different values depending on the Co:Fe ratio. For near-stoichiometric Co$_{1.1}$Fe$_{1.9}$O$_4$, the calculated B_{1Co} value was about 55 MJ/m^3 while for non-stoichiometric Co$_{0.8}$Fe$_{2.2}$O$_4$, the calculated B_{1Co} value was of the order of 180 MJ/m^3. The value for near-stoichiometric cobalt ferrite is closest to our estimated value of B_{1Co} which is 40 MJ/m^3. This is consistent with the fact that our particles were synthesized with the initial ingredients' molar ratio fixed to that of stoichiometric spinel ferrite.

On a more fundamental note, we will discuss what causes the difference in the two values in the first place. In their paper, Bozorth et al. reported that near-stoichiometric bulk Co$_{1.1}$Fe$_{1.9}$O$_4$ was found to have a much lower anisotropy constant and it was not responsive to magnetic annealing, i.e. it has low magnetostriction as compared to the non-stoichiometric samples [24]. The physical interpretation can be explained from the theory of directional ordering proposed by Néel [23]. As described in Chapter 2, directional ordering refers to the

macroscopic anisotropy in the local atomic configuration which occurs under certain anisotropic treatments, in this case, magnetic annealing. Since the non-stoichiometric samples were fabricated by combining a solid solution of magnetite (Fe_3O_4) and cobalt ferrite ($CoFe_2O_4$), it is highly possible that the spinel compound contains both Fe^{2+} and Co^{2+} ions. At a stable state, the Fe^{2+} and Co^{2+} ions will be distributed randomly in the B sites, forming an isotropic mean local configuration. Under the magnetic annealing effect, the ions would distribute unevenly to form an anisotropic local configuration. Conversely, we consider the case of stoichiometric cobalt ferrite where only one Co^{2+} ions reside in the B site. With or without an anisotropic treatment, the Co^{2+} ion population would distribute equally in the B sites and there would be no polarization in the local configuration. This explains the high magnetostriction (and anisotropy) of the non-stoichiometric, Fe-rich cobalt ferrite and the low magnetostriction of the stoichiometric cobalt ferrite.

Another explanation is provided by Iida et al. where they consider the effect of cationic vacancies in non-stoichiometric cobalt ferrites, which promotes the directional ordering of Co^{2+} by speeding up ionic diffusion during magnetic annealing [25]. Lattice vacancies tend to occur in non-stoichiometric compounds to compensate the imbalance in the net ionic charges. This may be the case for tetragonally distorted CFO thin films [3][4]. As opposed to the heat stress induced during magnetic annealing, magnetostriction in these thin films is due to mechanical stress coming from the epitaxial strain. In the most recent report by Tainosho et al. [4], the B_1 value estimated for the epitaxial CFO thin films is 131 MJ/m^3. This value is evidently much higher than our obtained value (B_{1Co} = 40 MJ/m^3). We can attribute the B_{1Co} deviation to the compositional difference between the two materials. As opposed to our stoichiometric particles, the thin films were fabricated using a Co:Fe ratio of 1:3, to get the cobalt ferrite composition of $Co_{0.75}Fe_{2.25}O_4$. The non-stoichiometric composition was arrived at by optimizing the crystallinity and saturation magnetization of the thin films (Niizeki et al. 2013). Interestingly, the B_{1Co} value of the thin films is 175 MJ/m^3, which is consistent with the value for bulk non-stoichiometric cobalt ferrite (as above). The thin films, however, do not contain Fe^{2+}, as revealed by compositional analysis from x-ray absorption fine structure (XAFS) experiments [unpublished]. If so, then the high magnetostriction can be attributed to the presence of lattice vacancies, as proposed by Iida et al. for non-stoichiometric cobalt ferrites.

Another argument for the deviation observed between our B_{1Co} value and that of the thin films is the difference between the intrinsic nature of particles and thin films. For example, the high ME coupling coefficient in the thin films may originate due to the presence of higher order terms of B_1 [70][71]. Higher order terms of ME coupling coefficients may arise from residual strain near the thin films' surface, and therefore it is called surface anisotropy [22][72]. Compared to the epitaxial thin films, our synthesized particles are sub-micron in size, which means they have a much smaller surface to volume ratio and therefore are much less susceptible to surface effects. In the case of sub-micron particles, the distribution of lattice strain is averaged and considered as 'homogenous' throughout the sample due to the large dimensions. This means that any residual strain near the particles' surface is insignificant compared to the internal strain, so they do not contribute to higher order terms of B_1. This may not be the case for the epitaxial thin films as they have much larger surface to volume ratio and thus surface anisotropy might come into play. In this case, the higher order terms would no longer be negligible, and it may not be sufficient to express ME coupling with only the lowest order term. The higher order terms of B_1 may contribute to the large magnetostriction and hence the large B_{1Co} of epitaxial CFO thin films.

6.4. Conclusions

We analyzed the magnetic anisotropy of tetragonal (Cu,Co)-ferrite particles within a phenomenological magnetoelastic model.

Anisotropy field deduced from rotational hysteresis loss analysis

The anisotropy fields were deduced from the torque measurements and rotational hysteresis loss analysis. Similar to the coercivity, the anisotropy field showed a non-linear behavior with respect to the Co content x. We try to elucidate the relationship between coercivity and anisotropy field and found a linear representative for the samples with Co substitution ($x > 0$). This is an indication that the origin of the anisotropy is mainly from the Co ions. Considering this, the magnetic anisotropy should increase monotonously with the concentration of Co, as suggested by the one-ion model. From the anisotropy field, we determine the uniaxial anisotropy constant K_u and plotted it against the Co content. We found that the value tends to saturate above $x = 0.1$, which suggests that there is another contributing factor to the anisotropy other than the Co concentration, and the one-ion model alone is insufficient to express the K_u. We consider the tetragonality factor and the magnetoelastic coupling induced by the JT effect/distortion.

Magnetoelastic model of the Jahn-Teller effect

The proposed model considers the magnetoelastic anisotropy which consists of the product of two parameters; i.e. the ME coupling coefficient B_1 and the tetragonality χ, both of which are dependent on the Co concentration. We considered the effective contribution of Cu and Co and express it as B_1^{tot}. Both of these parameters, B_1^{tot} and χ are linear functions of the Co content x, so that the product gives a quadratic function of x. This is the reason that the measured anisotropy fields H_A and the anisotropy constant K_u were not simple linear functions of x. It also explains why the one-ion model was not applicable in this case. To model the magnetoelastic anisotropy, K_u is plotted as a function of $x\chi$, where χ is the tetragonality factor. The $K_u(x)$ versus $x\chi(x)$ plot gave good linear behavior for the tetragonally distorted samples where $\chi > 0$. The deviation observed for the $x = 0.2$ sample where $\chi = 0$ suggests that the magnetoelastic model is not applicable to the non-distorted system.

Estimation of magnetoelastic coupling coefficients

The ME coupling coefficients estimated from the linear behavior observed in the plot of K_u versus $x\chi$ are summarized in **Table 6.2** for both the Cu and Co components. Our estimated values agree with both the bulk values calculated for copper ferrite [67] and for near-stoichiometric cobalt ferrite [24]. The linear behavior observed, along with the consistency in the estimated B_1 values support the proposed magnetoelastic coupling model induced by the Jahn-Teller effect of Cu^{2+}.

Table 6.2 Summary of the magnetoelastic coupling coefficients obtained experimentally and that calculated for the respective bulk materials.

Compound	B_{1Co} (MJ/m^3)	B_{1Cu} (MJ/m^3)	References
$Cu_{1-x} Co_x Fe_2 O_4$ ($0 \leq x < 0.2$)	40	1.5	(this study)
$Co_{0.9}Fe_{1.1}O_4$	55	-	[24]
$CuFe_2O_4$	-	4	[67]

7. Coercivity analysis of (Cu,Co)-ferrite particles

Coercivity is one of the most important features of permanent magnet materials. In this chapter, we will describe an analysis of the coercivity of two representative (Cu,Co)-ferrite samples prepared during this thesis. We analyzed the temperature dependence of coercivity within the micromagnetic (MM) and global models, to probe the role of microstructural features in magnetization reversal.

7.1. Experimental analysis of the temperature dependence of coercivity

The two representative $Cu_{1-x}Co_xFe_2O_4$ samples considered have different values of coercivity owing to their different Co and Cu content, and crystal structure. The sample with the higher coercivity is the tetragonally distorted $x = 0.1$ sample, whereas that with the lower coercivity is the cubic $x = 0.2$ sample.

7.1.1. Hysteresis cycles and H_c(T)

The full loop hysteresis cycle of the tetragonal ($x = 0.1$) sample measured at 300 K is shown in **Fig. 7.1**. Half hysteresis cycles measured at temperatures between 3 K and 300 K are shown in **Fig. 7.2**.

On each measured hysteresis cycle, the coercive field was determined using the following procedure: first, the magnetization variation in the vicinity of the coercive field was measured in detail (see experimental points in **Fig. 7.3 (a)**). Then, the derivative of magnetization variation $M(H)$, or the total magnetic susceptibility χ^{tot}, was calculated and plotted against the applied field in **Fig. 7.3** (b). The maximum magnetic susceptibility, at which the maximum number of reversal events occur, is known as the switching field. Here we take the coercivity to be equal to the switching field. In the case of the powder samples studied here, the switching field is very close in value to the classical definition of coercivity ($M = 0$).

Using the above procedure, the temperature dependence of the coercive field, H_c(T) was evaluated for the tetragonal ($x = 0.1$) and the cubic ($x = 0.2$) samples (**Fig. 7.4**). The coercivity of the tetragonal ($x = 0.1$) sample increases from 0.26 T at 300 K, to 0.56 T at 20 K; before decreasing to 0.55 T at 3 K. The H_c (T) value increases progressively from 300 K to 100 K, but tends towards a constant value at lower temperatures, before dropping at the lowest temperature studied. The behavior of the cubic $x = 0.2$ sample is similar, though translated to lower coercivity values, and the value increases from 0.09 T at 300 K to 0.46 T at 3 K. In this sample the tendency towards a constant value of H_c was observed from 20 K downwards, but no decline in the H_c value was observed at the lowest temperature.
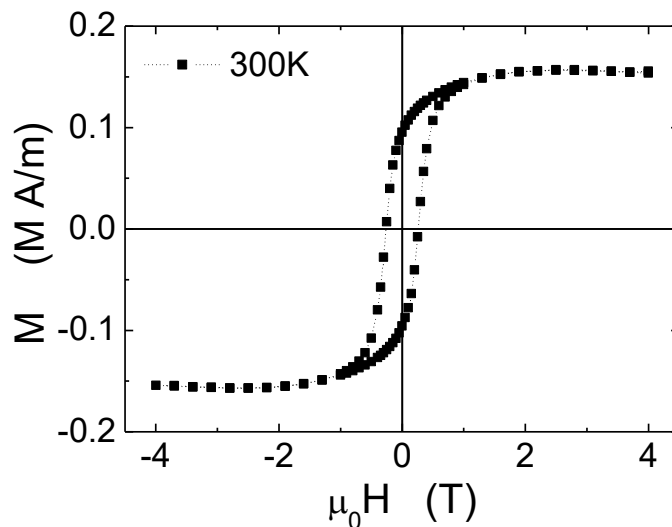
Fig. 7.1 Hysteresis cycle corresponding to the tetragonal $x = 0.1$ sample measured at 300 K.
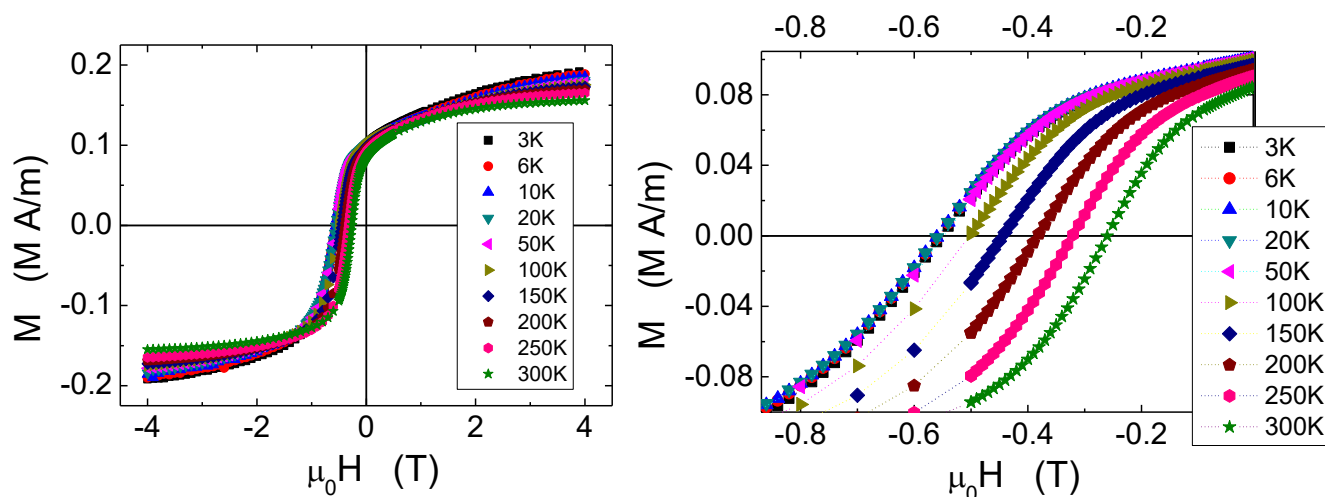
Fig. 7.2 Hysteresis curves measured in the range of 3 K – 300 K for the tetragonal $x = 0.1$ sample; in full scale from -4T to 4T, and in an enlarged scale at the vicinity of the coercive fields.
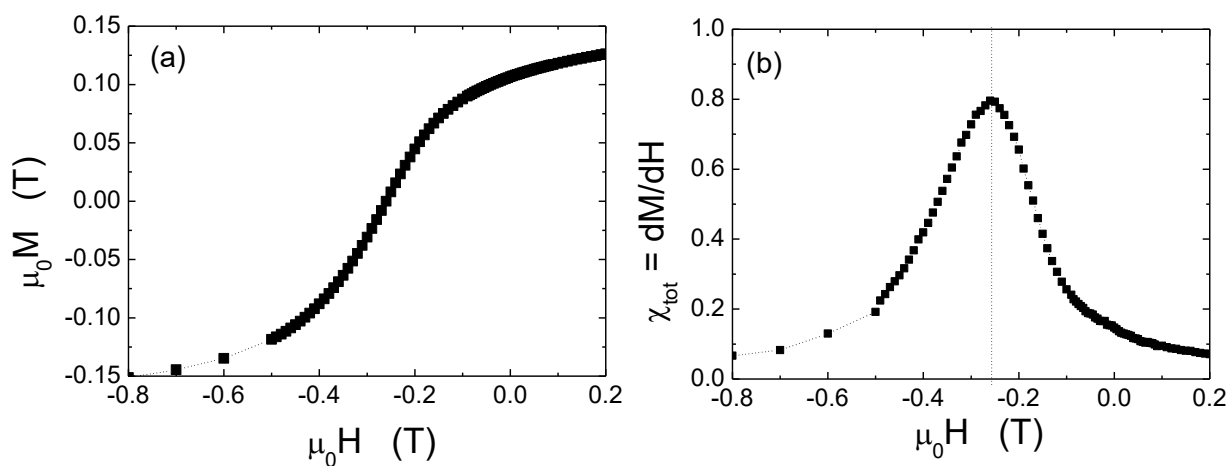
Fig. 7.3 $M(H)$ curve in the vicinity of the coercive field measured on the $x = 0.1$ sample at 300 K (a) and the corresponding plot of susceptibility versus the applied field (b).
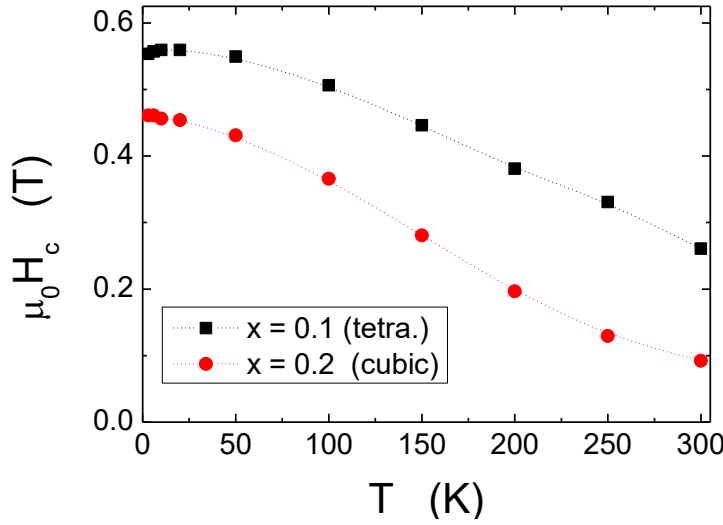
Fig. 7.4 H_c(T) for the tetragonal $x = 0.1$ and the cubic $x = 0.2$ samples.

7.1.2. Temperature dependent coercivity $H_c(T)$ analysis within the Micromagnetic model (MM)

Now we have all that we need to apply the MM analysis to the temperature dependence of H_c in these samples. This model was described in Section 3.4. For temperatures in the range 3 K to 300 K, eq. (3.7) is applied:

$$H_c(T) = \alpha^{MM} \frac{2K}{\mu_0 M_s} - N_{eff}^{MM} M_s$$

The coefficients N_{eff}^{MM} and α^{MM} (we add the MM superscripts to distinguish between the MM and global models) can be determined by plotting $\left(\frac{H_c}{M_s}\right)$ as a function of $\left(\frac{2K}{\mu_0 M_s^2}\right)$, as shown in **Fig. 7.5**. The parameter α^{MM} is considered as a constant, and its value indicates how much the coercivity field is reduced due to microstructural features. The solid points (black and red) in **Fig. 7.5** are the experimental data obtained using the values of M_s and K_1 evaluated in Annex 1. Both data sets can be reasonably well represented by linear fits. For the tetragonal ($x = 0.1$) sample, the linear fit gave values of 1.42 for N_{eff}^{MM} and 0.24 for α^{MM}. For the cubic ($x = 0.2$) sample, the values obtained are 1.47 for N_{eff}^{MM} and 0.27 for α^{MM}.

In the MM model, $\alpha^{MM} > 0.3$ is taken to indicate that coercivity is governed by nucleation, whereas $\alpha^{MM} < 0.3$ may occur for nucleation or pinning [42][73]. Thus, we cannot use the MM model to rule out either coercivity mechanism for our $Cu_{1-x}Co_xFe_2O_4$ samples. Our α^{MM} values are lower than those typically found for NdFeB magnets assessed within the MM model (0.5 – 1) while our N_{eff}^{MM} values fall within the typical range reported for such magnets (0.5 – 1.5) (see **Fig. 7.6**) [73]. As similar values of α^{MM} and N_{eff}^{MM} are found for both sample types, analysis within this commonly used model does not bring much to our study.
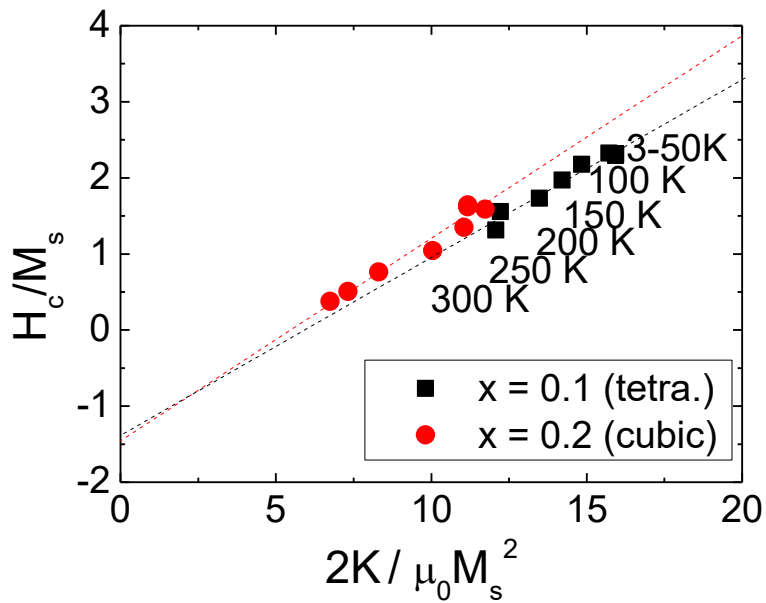
Fig. 7.5 (H_c/M_s) vs. ($2K/M_s^2$) for the $Cu_{1-x}Co_xFe_2O_4$ samples, experimental results (black squares and red dots) and linear fit (dotted lines).
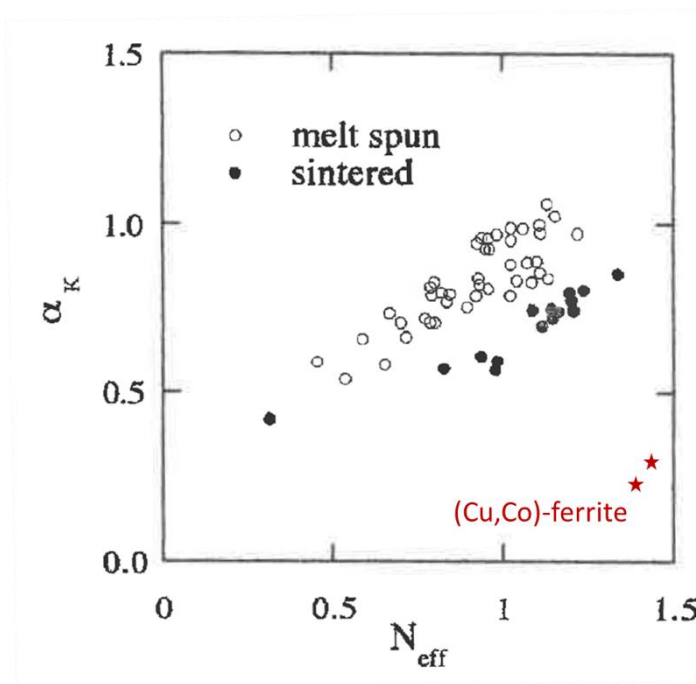

Fig. 7.6 Microstructural parameters α_K versus N_{eff} in a series of Nd-Fe-B magnets. After Givord and Rossignol (Coey, 1996: p. 259) [73]. Red stars represent the α^{MM} and N_{eff}^{MM} parameters of the (Cu,Co)-ferrite particles obtained in this study.

7.1.3. Temperature dependent coercivity $H_c(T)$ analysis within the Global model (GM)

The basic concepts behind this model were already presented in Section 3.5. In this model, another experimental parameter needs to be derived, the activation volume in eq. (3.9) is:

$$v_a = \frac{k_B T}{\mu_0 S_v M_s}$$

where the magnetic viscosity coefficient S_v expressed as

$$S_v = \frac{S}{\chi^{\text{irr}}}$$

can be derived from time and field dependent measurements. The time dependent measurement, or the magnetic viscosity S is given as

$$S = \frac{dM}{d\ln t}$$

whereas the field dependent measurement is the irreversible susceptibility χ^{irr} given as

$$\chi^{\text{irr}} = \chi^{\text{tot}} - \chi^{\text{rev}}$$

where χ^{tot} is the total susceptibility and χ^{rev} is the reversible susceptibility.

The protocol to calculate v_a is presented for the tetragonal ($x = 0.1$) sample at 300 K. For the magnetic viscosity measurement, the sample is first saturated under a magnetic field of 2 T in a certain direction. Then, a demagnetizing field is applied, and the magnetization is measured for a duration of typically 30 min. Since the time effects are more obvious under a demagnetizing field close to the coercive field, we performed these measurements for a few values of applied field near the coercive field, at each temperature indicated in **Fig. 7.2**. In these situations, the height of the energy barrier is high enough so that the magnetization does not reverse under the applied field alone, but low enough so that in a few minutes after the field is applied, it jumps from the saturated "up-state" to the reversed "down-state" due to thermal fluctuations.

The room temperature ($T = 300$ K) $\Delta M(t)$ curves for the tetragonal ($x = 0.1$) sample are shown in **Fig. 7.7** (a) and the corresponding curves on a logarithmic time scale $\Delta M(\ln t)$ are shown in **Fig. 7.7** (b). Magnetic viscosity, S, refers to the linear behavior of M with $\ln t$ and is quantified by the slope of these lines. Another parameter to be derived is the irreversible susceptibility χ^{irr}, for which we take the difference between the total susceptibility (shown in **Fig. 7.8** (a)) and the reversible susceptibility χ^{rev}, given by the slopes of the recoil curves shown in **Fig. 7.8** (b).

The parameters S, χ^{irr}, and S_v are plotted versus the applied field $\mu_0 H$ and the magnetization M corresponding to the applied field for the tetragonal ($x = 0.1$) sample (300 K) in **Fig. 7.9** (a) – (c), respectively. Since M varies with time, the value of the applied field alone cannot be used to characterize each magnetization state. Rather, a given magnetic state may be determined by the value of the material's magnetization. It is thus more significant to plot S and χ^{irr} as a function of the magnetization at which these parameters have been obtained. Both the magnetic viscosity and the irreversible susceptibility present a maximum close to the coercive field (see **Fig. 7.9**). The red and blue points represent the applied field dependent (S vs. H, χ^{irr} vs. H_i, S_v vs. H) and magnetization dependent (S vs. M, χ^{irr} vs. M, S_v vs. M) curves, respectively. Taking the ratio of the two parameters, we get the magnetic viscosity coefficient, S_v,

The same procedure was performed for both samples at different temperatures, from 3 K to 300 K and the activation volume was derived in each case. The results are shown in **Fig. 7.10**. At a fixed temperature, the activation volume does not change significantly for different values of applied field. This was observed in both samples. Upon decreasing the temperature, v_a decreases, the influence of temperature becoming less and less important. Therefore, the activation volume is a parameter that characterizes the sample at a certain temperature, and it does not depend on the value of the applied field, when the field is close to the coercive field.
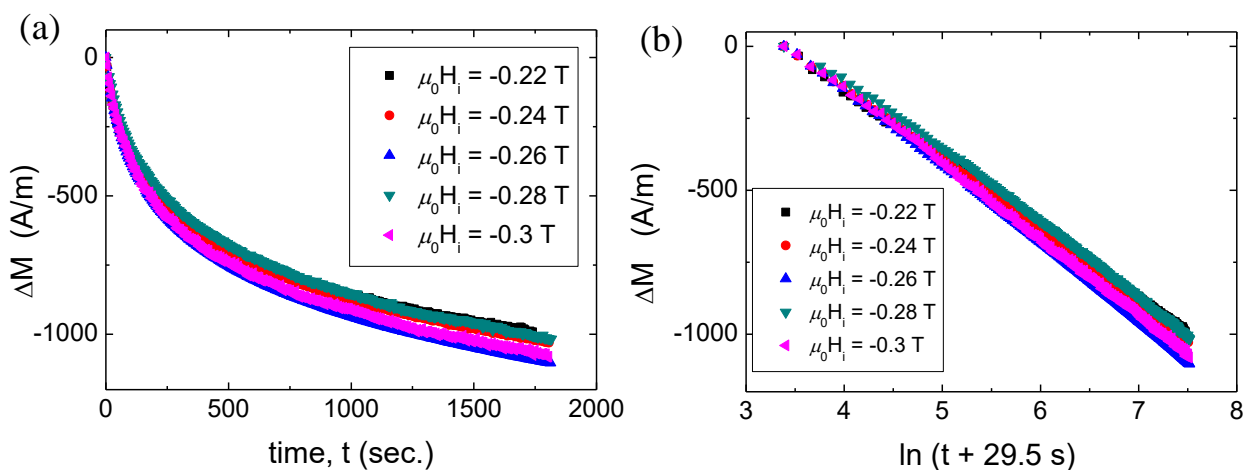
Fig. 7.7 Variation of magnetization ΔM as a function of (a) time, and (b) time on a logarithmic scale, measured at 300 K for different values of the applied demagnetizing fields.
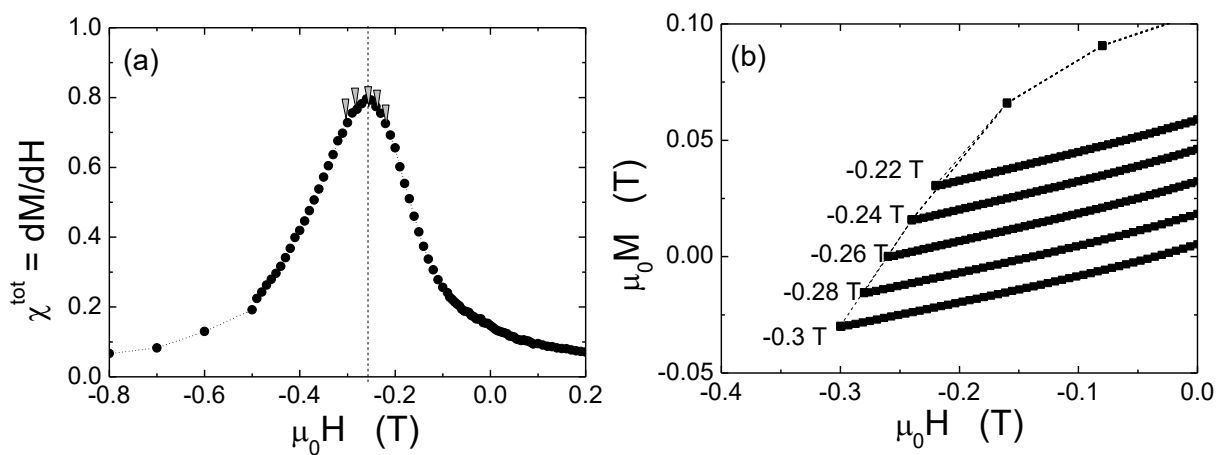
Fig. 7.8 (a) Magnetic susceptibility as a function of the applied field. (b) Recoil curves used to estimate the reversible susceptibility corresponding to different magnetic field values.
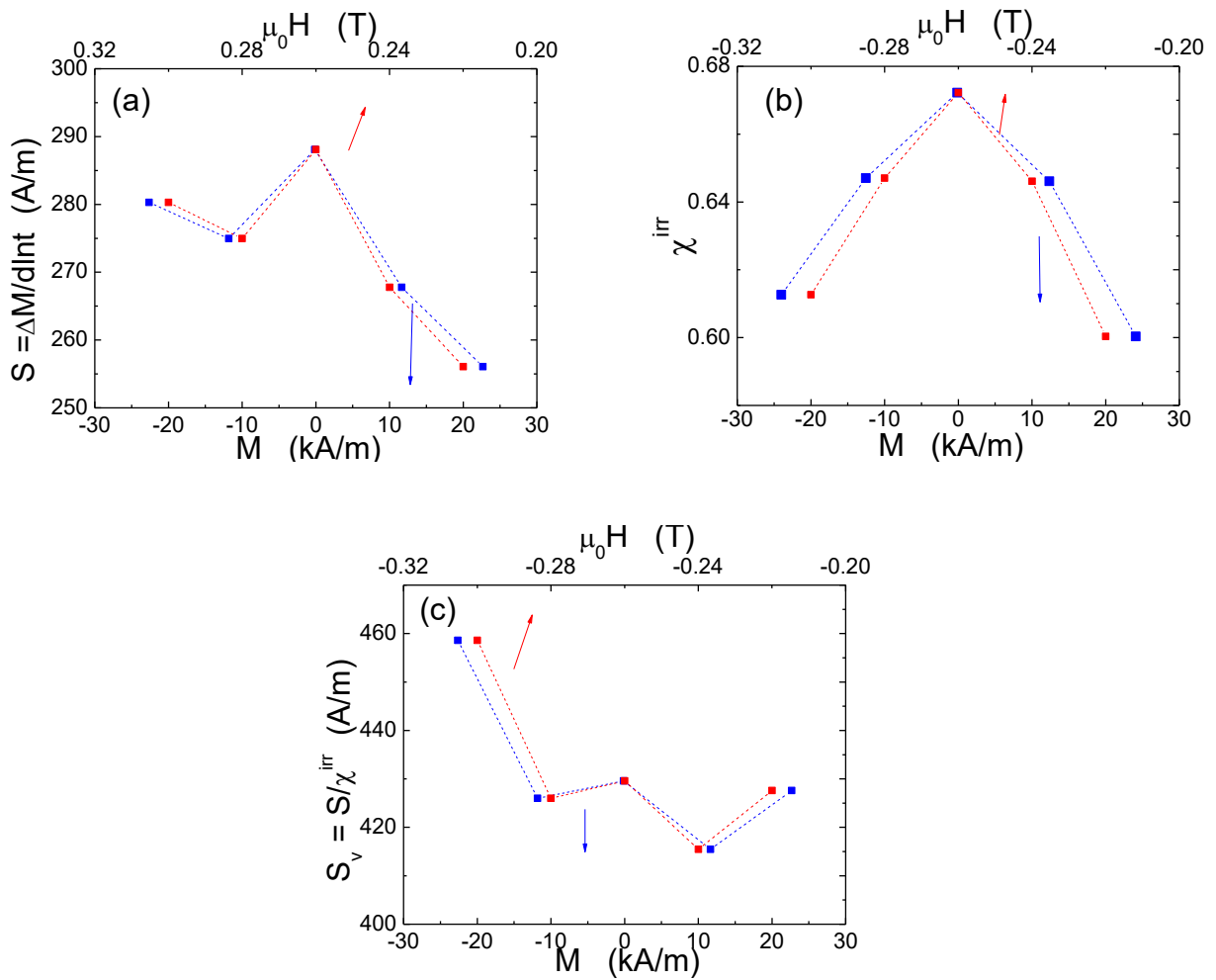
Fig. 7.9 Magnetic viscosity, S (a), irreversible susceptibility, χ^{irr} (b) and magnetic viscosity coefficient, S_v (c) as a function of applied field and magnetization corresponding to the tetragonal ($x = 0.1$) sample at 300 K.

For each sample, a unique value of v_a was determined for each temperature from the graphs in **Fig. 7.10**. Extracting these numbers and plotting them as a function of the temperature, one gets the curves shown in **Fig. 7.11** (a), which show the variation of the activation volume with temperature. For the tetragonal $x = 0.1$ sample, v_a increases monotonously from a value of around 1120 nm^3 ($v_a^{1/3} \approx 10$ nm) at 3 K, up to around 48000 nm^3 ($v_a^{1/3} \approx 36$ nm) at 300 K. Similarly, for the cubic $x = 0.2$ sample, the value increases monotonously from 400 nm^3 ($v_a^{1/3} \approx 7$ nm) at 3 K, up to around 122000 nm^3 ($v_a^{1/3} \approx 50$ nm) at 300 K.

As discussed in Chapter 3, the activation volume is associated with the formation of a non-uniform magnetic configuration, which is reminiscent of a magnetic domain wall [44]. Thus, it is legitimate to compare the size of the activation volume with the size (width) of magnetic domain walls in the considered ferrite materials. The domain wall width (δ) was calculated using the expression $\delta = \pi\sqrt{A/K}$, where A is the exchange stiffness and K the magnetic anisotropy constant. The value of A at absolute zero, $A(0)$ is calculated using the expression $A(0) \approx k_B T_c / a$, where the Curie temperature T_c is taken as that of copper ferrite ($T_c = 728$ K) and a is taken as the lattice parameter of copper ferrite $a = 8.42$ Å. The temperature dependence $A(T)$ was calculated from the expression $A(T) = A(0)\left[\frac{M_s(T)}{M_s(0)}\right]^2$. The values of $M_s(T)$ and $K(T)$ used are evaluated from the analysis given in Annex 1. The ratio between v_a and the cube of the domain wall increases monotonously with temperature (**Fig. 7.11** (b)). From the plot of v_a as a function of the cube of the domain wall, the linear proportionality that has been approximately observed in many other materials [8], is not observed for the samples studied here.

To follow the global model rigorously, the coercive field should be corrected for thermal activation effects, equivalent to a field amounting to $25 S_v$ from the relation

$$H_0 = H_c + 25 S_v$$

where H_0 represents the field needed to reverse the magnetization in the absence of thermal energy. By correcting the coercive field in **Fig. 7.4** for the said thermal activation effects, one gets the $H_0(T)$ curves shown in **Fig. 7.12**.

Now we have all that we need to apply the GM analysis to the temperature dependence of H_c in these samples. For the temperatures 3 – 300 K, eq. (3.11) is applied:

$$\frac{H_0}{M_s} = \alpha^{GM} \frac{\gamma}{\mu_0 M_s^2 v_a^{1/3}} - N_{eff}^{GM}$$

Similar to the micromagnetic analysis, the coefficients N_{eff}^{GM} and α^{GM} are determined by plotting $\left(\frac{H_0}{M_s}\right)$ versus $\left(\frac{\gamma}{\mu_0 M_s^2 v_a^{\frac{1}{3}}}\right)$, as shown in **Fig. 7.13**.

The solid points (black and red) in **Fig. 7.13** are the experimental data obtained using the experimental H_c, and v_a deduced from an analyze of S_v values. The domain wall energy γ was calculated using the expression $\gamma = 4\sqrt{AK}$, where A and K are evaluated as described above. For both samples, the equation of $H_0(T)$ of the GM fits adequately only in the high temperature region ($T > 100$ K). From the linear fit using least-square methods, the N_{eff}^{GM} and α^{GM} values obtained are -0.38 and 0.39, respectively, for the tetragonal $x = 0.1$ sample. For the cubic $x = 0.2$ sample, the N_{eff}^{GM} and α^{GM} values obtained are -0.05 and 0.29, respectively. An important observation here is that, at T < 50 K, large discrepancies are observed between the experimental values and the linear model description. Assuming that the GM premises are acceptable throughout the temperature region, this deviation then suggests that in the low temperature region, the system was acting as if it were at a higher temperature, i.e. there is some sort of heating occurring so that the temperature experienced by the sample is $T + T^*$, rather than T (the nominal temperature). Possible explanations for this phenomenon are presented in the next section.
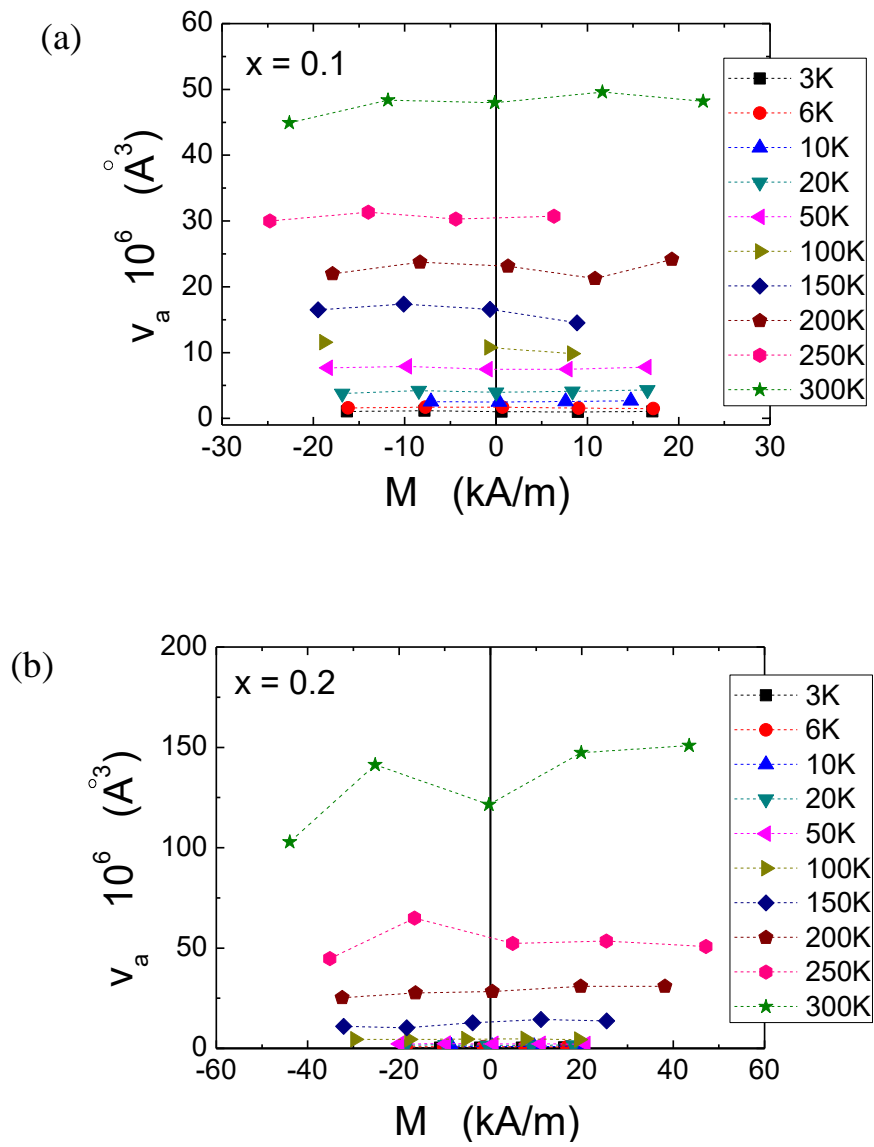
Fig. 7.10 The activation volume as a function of magnetization, at different temperatures for the: tetragonal ($x = 0.1$) sample (a); and the cubic ($x = 0.2$) sample (b).
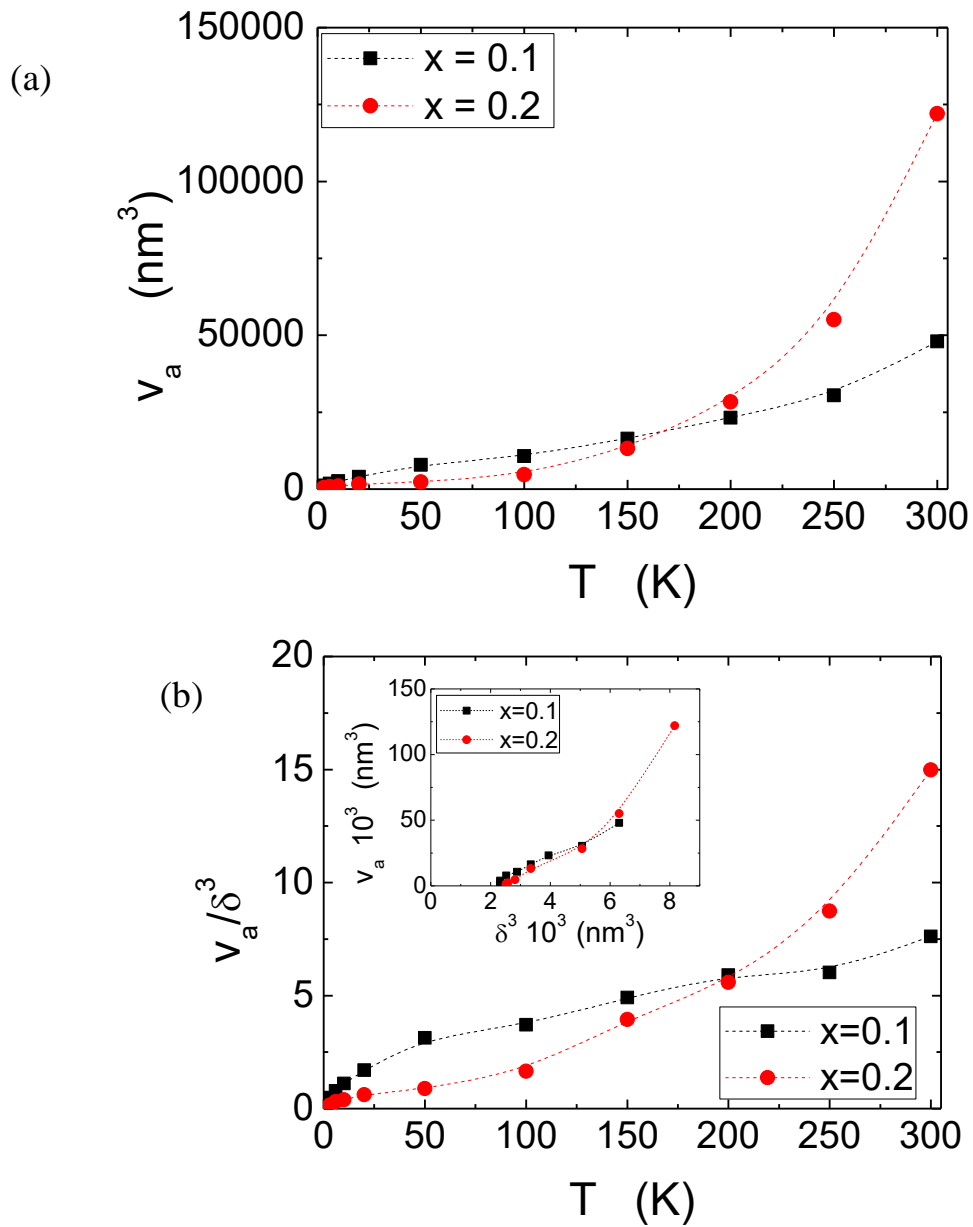
Fig. 7.11 (a) The activation volume of the tetragonal ($x = 0.1$) and cubic ($x = 0.2$) samples; and (b) the ratio between v_a and δ^3 plotted as a function of temperature. Inset (b): deduced temperature dependence of the activation volume plotted as a function of the cube of the domain wall.
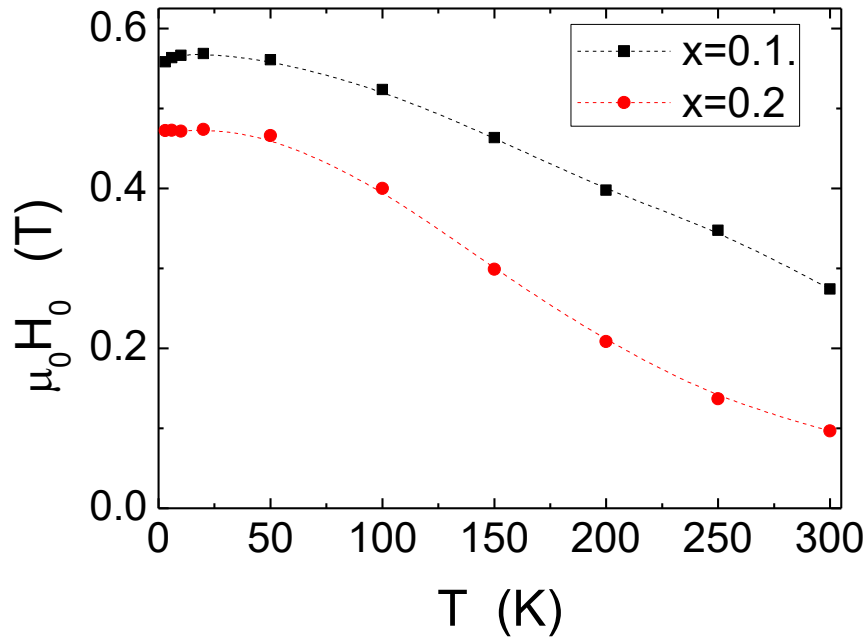
Fig. 7.12 Coercive field corrected for thermal effects ($H_0 = H_c + 25\,S_v$) as a function of temperature for the the tetragonal ($x = 0.1$) and cubic ($x = 0.2$) samples.
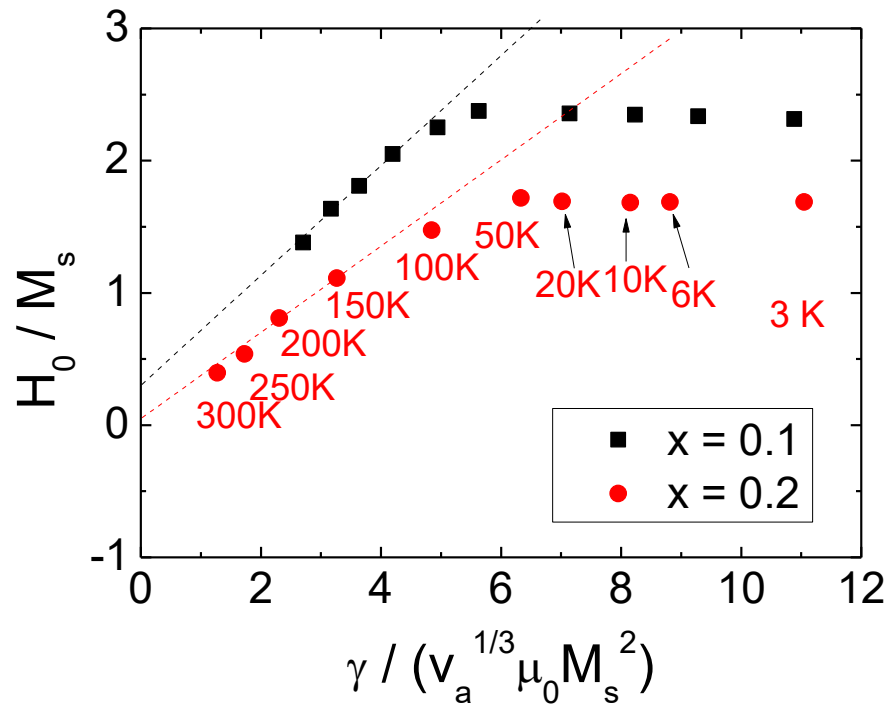
Fig. 7.13 H_0/M_s versus $\gamma/(\mu_0 M_s^2 v_a^{1/3})$ plots for the tetragonal ($x = 0.1$) and cubic ($x = 0.2$) samples. Closed circles and squares represent the experimental points whereas dotted lines are the linear fits.

7.2. Discussion: Estimation of *T** and physical interpretation of the *T** effect
7.2.1. Estimation of *T** and GM correction

To estimate the value of T^*, we assume that the global model premises are applicable throughout the temperature region. The discrepancy in the low temperature region of the GM plot (**Fig. 7.13**) suggests that the temperature is effectively higher in this region. We assume this effective temperature to be $T + T^*$ ($T^* > 0$) and denoted it as the T^* anomaly. The protocols used to estimate the value of T^* is described as follow.

Among the parameters (H_0, γ, v_a, M_s, K, and S_v) used to express coercivity in the global model in eq. (3.11), the magnetic viscosity parameter S_v is derived from thermal expressions. Therefore, the T^* anomaly is most likely to arise from this parameter. First, we recall the derivation of the magnetic viscosity S ($= dM/d\ln t$) from the magnetization reversal induced by thermal fluctuation in eq. (3.15). Essentially, eq. (3.15) shows that the magnetic viscosity S is proportional to $k_B T$ ($S \propto k_B T$). If we replace the value of the nominal measuring temperature T by $T + T^*$ ($T^* > 0$), the ratio of S to $k_B(T + T^*)$ should yield a constant value

$$\frac{S}{k_B(T + T^*)} = const.$$

(7.1).

Using eq. (7.1), we can derive the experimental curves $S_{exp}(T)$ shown in **Fig. 7.14** with several values of ($T + T^*$) and find the value of T^* at which all curves converge to a unique curve (corresponding to a constant value). Doing so, we have found the convergence conditions by using $T^* = 30$ K for the tetragonal ($x = 0.1$) sample and $T^* = 18$ K for the cubic ($x = 0.2$) sample. This suggests that the heating effect, whatever its origin, is likely to be higher in the tetragonal ($x = 0.1$) sample.

Next, by replacing the value of T by $T + T^*$, we can recalculate the activation volumes at low temperature as $v_a' = k_B (T + T^*)/\mu_0 S_v M_s$ and use it in the $H_c(T)$ equation of the global model to get a better description of the model. **Fig. 7.15** (a) shows the global model plot after performing the T^* correction. All data points at the low temperature region now converge to form a linear plot, and thus removing the discrepancies that were observed before. When v_a' is plotted as a function of the cube of the domain wall (**Fig. 7.15** (b)), the values show improved linear proportionality, particularly for the $x = 0.1$ sample, compared to the equivalent plot before application of the T^* correction (see **Fig. 7.11** (b), inset).
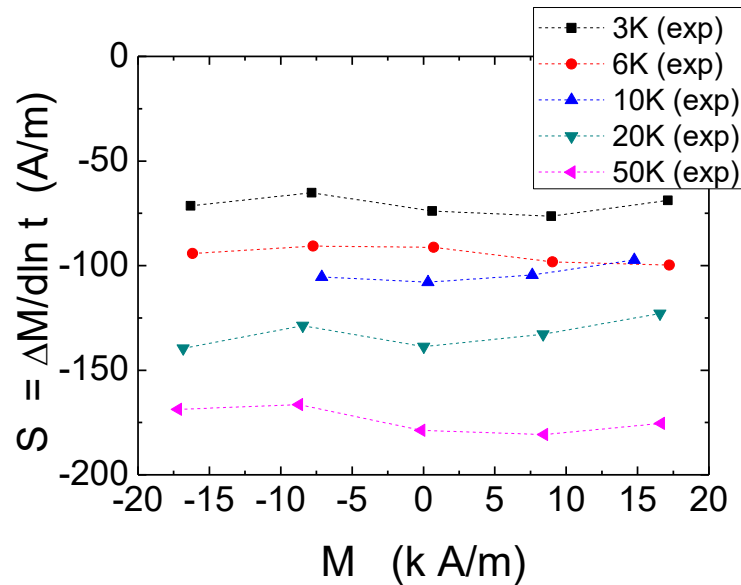

Fig. 7.14 Experimental curves of magnetic viscosity $S_{exp}(T)$ measured between 3 K and 50 K.
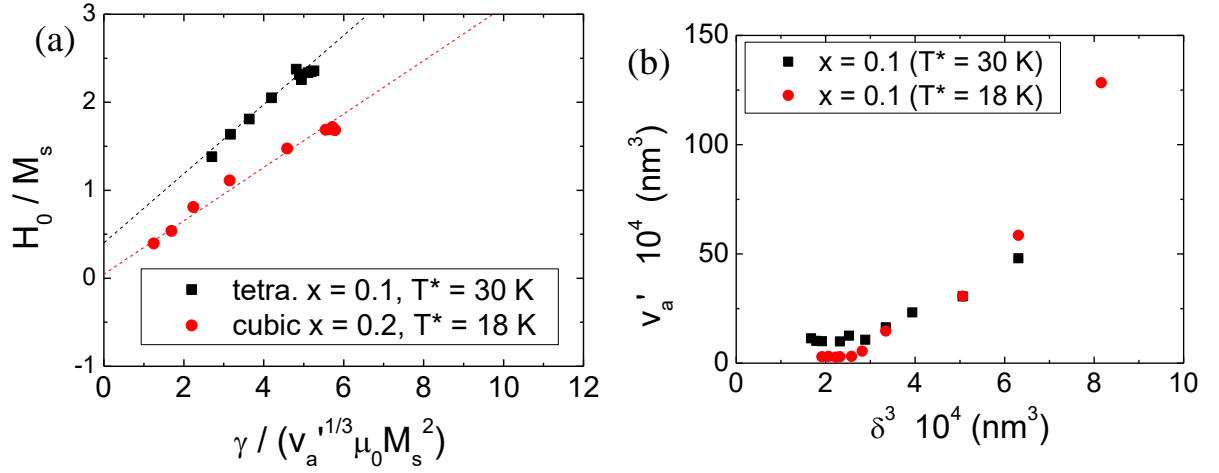
Fig. 7.15 Global model after the T^* correction: H_0/M_s versus $\gamma/(\mu_0 M_s^2 v_a'^{1/3})$ plots for $Cu_{1-x}Co_xFe_2O_4$ samples (a) solid dots and squares – experimental points; dotted lines: linear fit. (b) Deduced temperature dependence of the activation volume after T^* correction, plotted as a function of the cube of the domain wall.

7.2.2. Physical interpretation of the T^* effect

According to the global model analysis, we are almost certain that there is a heating effect which affects magnetization reversal during the magnetic viscosity measurements, causing the T^* anomalies. Let us denote this local heating effect as the T^* effect. In this section, we will discuss the following questions regarding the interpretation of the T^* effect:

(i)   What is the physical meaning of this T^* effect?

(ii)   How much does the T^* effect affect the magnetic viscosity measurements?

(i) *The physical meaning of the T^* effect: Change in Zeeman energy during reversal*

From the order of magnitude of T^* and the region where its effect became significant, it is realistic to assume that the T^* effect is a heating effect that occurs due to the ineffective dissipation of heat generated by magnetization variation following each switching event.

For reversal in a single grain of volume V_{grain}, the conversion of magnetic energy (in Joules) into thermal energy can be expressed approximately by

$$2\mu_0 M_s H_c V_{grain} = V_{grain} \int_{T_{init}}^{T_{fin}} C_V(T)\,dT$$

(7.2)

where $2\mu_0 M_s H_c$ is the change in magnetization energy during reversal (Zeeman energy), C_v is the volume specific heat. Here we assume that the spin contribution ($T^{3/2}$) is small enough and C_v is determined mainly by the lattice contribution (T^3). Using the low temperature specific heats of Fe_3O_4 measured by Westrum *et al.*[74] (see **Annex 2**), C_v is approximated using a simple polynomial function as

$$C_v \approx 8.6 T^{2.7}$$

(7.3)

Substituting this in eq. (7.2), we evaluate the rise in temperature ΔT ($= T_{fin} - T_{init}$) of a volume V_{grain} occurring during magnetization reversal due to thermal activation at the initial temperature T_{init}.

$$\int_{T_{init}}^{T_{fin}} 8.6\, T^{2.7}\, dT = \frac{8.6}{3.7}[T_2^{3.7} - T_1^{3.7}] = 2\mu_0 M_s H_c$$

(7.4)

The final temperature $T_{fin} = 18$ K is obtained by using the values $M_s = 0.2$ MA/m, $\mu_0 H_c = 0.55$ T, and $T_{init} = 3$ K. Hence, starting at 3 K, a temperature-rise of about $\Delta T = 15$K is estimated to occur due to magnetization reversal of a single grain. The order of magnitude of ΔT is of the order of the T^* values, already suggesting that the origin of the T^* effect is that of local heating due to thermally activated grains.

(ii) *Effect of T* on magnetic viscosity measurements*

If we assume that there is no local heating occurring, we can derive the 'expected' magnetic viscosity occurring exclusively due to thermal activation by taking the experimental $S_{exp}(100K)$ values as a reference. At 3K, the 'theoretical' magnetic viscosity following thermal activation $S_{ta}(3K)$ is proportional to $S_{exp}(100K)$ so that

$$S_{ta}(3K) = \frac{3}{100} S_{exp}(100K)$$

(7.5)

Applying eq. (7.5) for temperatures ranging from 3 K to 50 K, the 'theoretical' $S_{ta}(T)$ vs M curves are shown in **Fig. 7.16**. For comparison, the experimental $S_{exp}(T)$ vs M curves are shown in **Fig. 7.14**. Comparing the two sets of values, one observes that the experimental values are larger than the theoretical values by a factor of up to 10 (between 3 to 10 K).
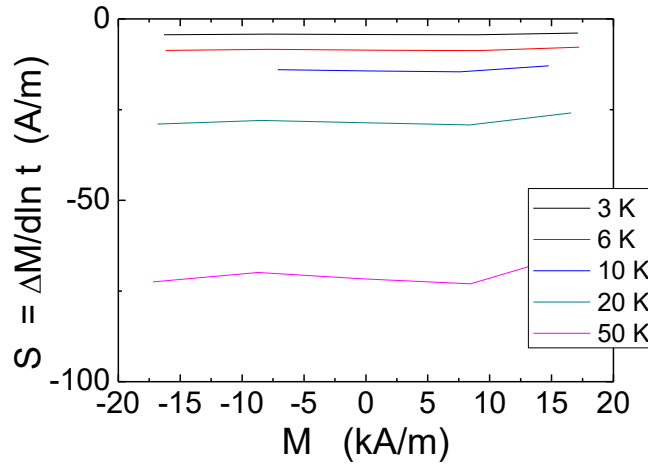

Fig. 7.16 Theoretical curves of magnetic viscosity following thermal activation, assuming there is no local heating.

7.3. Discussion: Enhanced thermal activation and local heating mechanisms

In the previous section, we estimated that local heating in the form of the *T** effect would lead to enhanced thermal activation. We try in this section to elucidate by which mechanism local heating affects magnetization reversal.

The local thermal energy produced by reversal of a single grain would promote magnetization reversal of adjacent grains, which in turn would cause heating of these grains, and subsequently reversal of more adjacent grains. Consequently, a single local heating process would lead to a cascade of magnetization reversal processes, referred to as thermal avalanche of magnetization reversal. To consider such a heating model, one must also consider what arrests the cascade after the avalanche has begun.

For example, Otani et al. proposed the local heating model due to the change in Zeeman energy to describe the anomalous demagnetizing curves observed in Nd-Fe-B magnets at low temperature [75][76]. Using a protocol similar to ours described in section 7.2.2, they estimated a temperature-rise of about 15 K for an initial temperature of 2.5 K. They also observed thermal spikes concurrent with the anomalous magnetization jumps by measuring the response of a thermocouple attached to the bulk sample. The step-like anomalies in the demagnetizing curves (**Fig. 7.16)** are apparent indications of the cascade of magnetization reversal, which Otani et al. described using the following two-step trigger/propagation process. During the demagnetization process, a critical reversal field triggers magnetization reversal of a certain volume of grains. Reversal is followed by local heating of the initially reversed grain, the entropy of which then propagates to adjacent grains and promoted further reversal. The 'shoulder' observed in each step-like anomaly is attributed to this thermal avalanche. As the avalanche progresses, the volume of reversed grains increases, and so does the internal field. At a certain point, the increasing internal field of the grown reversed nucleus requires more field to counter the thus produced demagnetizing field. Finally, the avalanche was arrested due to the effect of the demagnetizing field.

In the case of our CuCo-ferrite particles, we did not observe any anomalous jumps in the demagnetizing curves. Furthermore, unlike the bulk sample used by Otani et al., our samples consist of small particles so that it is not possible to attach a thermocouple to measure thermal spikes along the demagnetization curve. However, the effective temperature-rise that we deduced is similar to that estimated by Otani et al.. Therefore, the local heating model would reasonably explain both the *T** effect and the anomalous decrease in coercivity at low temperature for the tetragonal CuCo-ferrite sample. The absence of step-like demagnetizing curves suggests that the effect of the demagnetizing field in the trigger/propagate process is less significant.

What then arrested the cascade of magnetization reversal? Here, we consider various experimental indications that the particles may be exchange-coupled. If this is the case, the entropy produced during a single reversal process may propagate exclusively to the strongly coupled grains where there is intimate contact between neighboring grains (see **Fig. A1-3 (b)**). In other words, a single reversal process leads to reversal in only a fraction of adjacent grains; which leads to reversal in another fraction of adjacent grains. The probability to reverse magnetization is reduced with each reversal process and the cascade is arrested simply due to the reduced probability of each reversal process. The propagation of magnetization reversal and thermal avalanche effect would be less significant, and this could explain why we did not observe any staircase-like demagnetizing curves in our (Cu,Co)-ferrite particles.
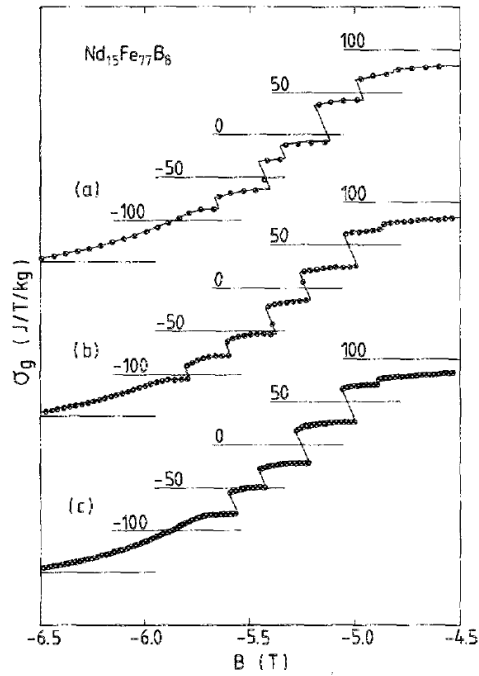
Fig. 7.16 Demagnetizing curves of NdFeB magnets measured at 2.5 K at various magnetic field sweep rates: (a) −0.4, (b) −0.2, (b) −0.1 T/min. All curves are plotted with respect to the effective magnetic field, corrected for the demagnetizing field (After Otani et al.). [75]

7.4. Conclusions
7.4.1. $H_c(T)$ analysis and the microstructure parameters α and N_{eff}

In the micromagnetic model, it is assumed that reversal starts in areas with much lower anisotropy than the main phase and α^{MM} gives an indication about how much the anisotropy is lowered in those volumes. The values found here are around 0.25, which is lower than the values for the micromagnetic analysis of Nd-FeB magnets [73] (**Fig. 7.6**). The parameter α^{GM} in the global model on the other hand, does not have a simple physical interpretation. Rather it relates the coercive field to some parameters of the main hard phase. In both the MM and GM analysis, the small variation of α from one sample to the other suggests that the reversal mechanism is similar for both samples.

The values obtained for N_{eff}^{MM} is about 1.4. Large N_{eff}^{MM} (> 1) are often found experimentally within the micromagnetic analysis of Nd-Fe-B magnets [73] (**Fig. 7.6**). In the global model, the values of N_{eff}^{GM} were -0.38 and -0.05 for the tetragonal ($x = 0.1$) and cubic ($x = 0.2$) samples, respectively. The classical value of N_{eff}^{GM} due to dipolar interactions is around +1. The deviation towards negative values ($N_{eff}^{GM}<0$) suggests the presence of another interaction which acts in a conflicting manner with dipolar interactions, i.e. exchange. The M_s and K analysis described in Annex 1 suggests the presence of intergranular exchange interactions in the assembly of grains, so that we can attribute the negative N_{eff}^{GM} values to exchange-coupling between grains. Comparison of the values of N_{eff}^{GM}, suggests that exchange interactions are weaker in the cubic ($x = 0.2$) sample than in the tetragonal ($x = 0.1$) sample.

7.4.2. The T^* effect and local heating model

The non-linearity observed within the global model suggests local heating of the sample following thermal activation. The estimated values of T^* are the right order of magnitude when compared with the estimated temperature rise due to the change in Zeeman energy of the reversed grains. Analyzing the T^* effect, along with the local heating model provides a suggestion as to why there is a coercivity reduction from 6 K to 3 K, as observed in the tetragonal ($x = 0.1$) sample. With local heating, the temperature increases, causing a reduction of the coercive field due to enhanced thermal activation. The idea is consistent with the grains being exchange-coupled. The T^* effect analysis concluded that at sufficiently low temperature, the coercivity is governed by local heating following thermal activation at low temperature, where the heating process may trigger more reversal.

To conclude this chapter, we can say that the mechanism of magnetization reversal in the tetragonal (Cu,Co)-ferrite particles ($x = 0.1$ sample) is significantly affected by intergranular exchange interactions, resulting from the sample's specific microstructure. The idea of local heating would explain the anomalies in the global model, along with the coercivity reduction at the lowest temperature (3 K). The higher N_{eff}^{GM} value obtained for the tetragonal ($x = 0.1$) sample compared to the cubic ($x = 0.2$) sample suggests stronger intergranular exchange interactions in the former. If we consider the grains are exchange-coupled, then the local heating and dissipation would be more effective due to the stronger exchange interaction between adjacent grains. This could explain why the coercivity variation of the tetragonal ($x = 0.1$) sample reaches saturation faster than the cubic ($x = 0.2$) sample as the temperature decreases.

8. Conclusions and prospects

8.1. Conclusions

This thesis concerned the preparation and study of tetragonal spinel ferrites, as potential permanent magnet material. Before we proceed with the conclusions, we would like to put the context of this work into perspective by using the chef and cook analogy.

When the first 'ferrite magnet' was developed in the 1930s, Kato and Takei found that cobalt-iron spinel ferrite material exhibited remarkable energy product (BH_{max}) values following a magnetic annealing procedure, from which they then developed commercial O.P. magnets. Using the cook's approach, the material was developed with a known procedure (magnetic annealing) which gives good properties (BH_{max}). At that time, this was the state-of-the-art and quickly enough, it gave rise to the development of many important models and theories regarding our understanding of magnetic anisotropy in cobalt-based spinel ferrites. The development of O.P. magnets was associated with a number of important scientific advances including the theory of directional ordering (Néel, 1953); the magnetic annealing effect and magnetostriction (Bozorth, 1955); and the one-ion anisotropy model (Slonczewski, 1955). With the development of these fundamental ideas, we had a better understanding as to the why and how of magnetic anisotropy in these materials. Now, we are entrusted to move onto the chef's approach, where we can (and should) design a specific material based on the first principles to exploit the material's properties.

In light of the directional ordering theory proposed by Néel, we understood that the magnetostrictive properties of cobalt-based spinel ferrites make them susceptible to anisotropic treatments. This could be in the form of heat stress, i.e. magnetic annealing and/or in the form of mechanical stress. In this study, we were interested in exploiting the latter anisotropic treatment. The motivation of this study was to make cobalt-based magnets by exploiting a classical lattice distortion effect, which is the Jahn-Teller effect. The aim was to couple the Jahn-Teller effect and the magnetoelastic effect of cobalt-based spinel ferrites. This study was divided into two main parts. The first part focused on the intrinsic design of the magnetoelastic anisotropy. The second part aimed to investigate the extrinsic factor, which is the coercivity, of the synthesized material. The main results of this work will now be recalled:

1. Magnetoelastic anisotropy of (Cu,Co)Fe₂O₄ particles

The target designed material was tetragonal $(Cu,Co)Fe_2O_4$ particles, where Cu and Co played independent roles in inducing magnetic anisotropy. Cu served as the Jahn-Teller (JT) element which induces tetragonal distortion while Co is the magnetoelastic element which is at the source of magnetic anisotropy. We synthesized sub-micron sized $Cu_{1-x}Co_xFe_2O_4$ particles via coprecipitation and flux methods with the Co content varied as $x = 0 - 0.2$. The narrow composition range was studied because of the critical Cu concentration required for the inducement of the cooperative JT effect. The size of particles obtained exhibited two different length scales corresponding to the primary and secondary grains, which are approximately of the order of 50 nm and 500 nm, respectively. The latter correspond to agglomerates of the former, and we attributed this microstructure formation to the flux process. To begin with, the combination of the coprecipitation and the flux methods was adopted to grow large particles free of thermal strain as we wanted to exclude surface effects and focus on Jahn-Teller distortion. We had not expected the primary grains of the order of 50 nm to remain in the final microstructure. Lattice distortion decreased with increasing x due to the suppression of the JT effect below the critical concentration of Cu. The saturation magnetization increased with x due to the increased content of Co ions which contain a higher magnetic moment than Cu. As it turned out, the unforeseen microstructure did not affect the crystal structure nor the intrinsic magnetic properties (spontaneous magnetization, magnetic anisotropy) since the variation in x was within our expectations. However, the microstructure did play a role in the reversal mechanism and coercivity, as recalled below.

The value of coercivity and anisotropy field both increased with x from $x = 0$ up to $x = 0.1$. Above this value, they tended to decrease. This is contrary to the linear behavior that would be expected in cubic cobalt

doped spinel ferrites. This irregular behavior of the coercivity and anisotropy field is attributed to the added tetragonality factor. Evidently, we found that the one-ion model is insufficient to express the anisotropy constant K_u deduced from the anisotropy fields. The contribution of tetragonality towards anisotropy is discussed within the framework of the phenomenological model of magnetoelastic theory. The phenomenological model expresses the magnetoelastic (ME) anisotropy K_u as the product of two basic parameters; one is the ME coupling coefficient B_1 which is the materials' intrinsic parameter, and the other one is the tetragonality χ, which is a variable. In the case of $(Cu,Co)Fe_2O_4$ particles, these two parameters are dependent on the concentrations of Co and Cu. We obtained the tetragonality expression from the variation in crystal structures and lattice distortion. Then, we defined a new term B_1^{tot} which contains the total contributions of both Cu and Co elements in B_1. Since both B_1^{tot} and χ are linear functions of the Co content x, the product, corresponding to the K_u gives rise to a quadratic function of x. This explains why the one-ion model, which predicted K_u to be a linear function of x, was not applicable in this case. We then modeled the magnetoelastic anisotropy by plotting K_u as a function of $x\chi$, where χ is the tetragonality factor. We found a good linear behavior in the $K_u(x)$ versus $x\chi(x)$ plot for the tetragonally distorted samples where $\chi > 0$. Furthermore, the fitting parameters of this linear expression which correlate to the ME coupling coefficients of Cu and Co are in agreement with the calculated bulk values of copper ferrite and cobalt ferrite. The consistency in our findings indicates that our proposed magnetoelastic model of the Jahn-Teller effect manages to explain the anisotropy of the tetragonal $(Cu,Co)Fe_2O_4$ particles.

2.   Coercivity analysis

The general expression of coercivity is given as

$$H_c = \alpha H_{crit} - N_{eff}M_s$$

where H_c is the coercivity, H_{crit} is the critical field, α and N_{eff} are temperature independent microstructure related parameters. An understanding of these parameters and their contribution to the coercivity and reversal mechanism should aid in the design of permanent magnets. However, the microstructure related parameters are mainly defect properties so that we cannot directly measure them. Coercivity models were applied to determine a and N_{eff} by indirect measurements. From temperature dependent measurements of the tetragonal $(Cu,Co)Fe_2O_4$ particles ($M(H)$ in the range 300 K down to 3 K), we found an anomalous reduction of coercivity when the temperature is reduced from 50 K to 3 K. In addition to extracting values of a and N_{eff}, coercivity analysis was used to study this anomalous behavior. In the framework of the so-called micromagnetic model, the critical field is associated with the anisotropy field. Since we observed a linear dependency down to 10 K, we cannot explain the coercivity anomalies found below 50 K using only the premises of this model. In the framework of the so-called global model, the critical field is associated with the energy of formation of a domain-wall inside the so-called activated volume. In this case we observed a linear dependency down to 100 K. The negative sign of the N_{eff}^{GM} parameter suggests the presence of exchange interactions, which we attributed to intergranular exchange interactions between the primary nanograins. Below 100 K, the linear behavior was disrupted. To correct the discrepancy, we replaced the temperature T term by $T + T^*$ and found a unique value of T^* of 30 K. Further analysis suggested that T^* is a local heating effect which occurs due to ineffective heat dissipation from the change in Zeeman energy during reversal. Considering the heat energy produced had promoted magnetization reversal in adjacent grains, the T^* effect is thought to be the main origin of the anomalous coercivity reduction in the low temperature region. Therefore, the GM analysis indicates that the coercivity is strongly influenced by intergranular exchange interactions. When there is local heating, exchange interactions promote the transmission of heat from one grain to the next, which resulted in the coercivity reduction.

8.2. Prospects

This study covered a new holistic approach to engineering the unique class of tetragonal spinel ferrites including; fabrication, experimental characterization, phenomenological modelling and coercivity analysis. Each aspect had brought new insights and at the same time uncovered new avenues for future work in this domain to better understand the material.

Optimization of the synthesis method was performed on the basis of the crystal structure (from XRD patterns) and magnetic properties (H_c and K). TEM analysis revealed that the flux method employed gives a very specific grain structure. More detailed, high resolution microstructure analysis (TEM, EDX..) could be used to further optimize the particle fabrication method.

Regarding magnetoelastic anisotropy, tetragonal (Cu,Co)ferrite particles may be considered as a model system in which the anisotropy can be controlled by the JT distortion. For consideration of this material in applications like permanent magnets, the following limitations need to be addressed. One is the trade-off condition between the JT ion and ME element in producing the magnetoelastic anisotropy. In order to maximize the distortion, we must incorporate as many Cu^{2+} ions, but this would mean that the source of ME anisotropy, the Co^{2+} ions have to be reduced. Another limitation is the low magnetization of Cu^{2+}. In permanent magnets, spontaneous magnetization is another key element, that together with coercivity, contributes to the energy product BH_{max}. The magnetization of copper ferrite corresponds to the magnetic moment of Cu^{2+} ($1\mu_B$). For comparison, magnetite has a magnetic moment of $4\mu_B$ originating from Fe^{2+} ions. In other words, despite the high coercivity and anisotropy obtained in the (Cu,Co)ferrite particles, the low magnetization makes it less suitable for applications as permanent magnets. To address these limitations, we propose the synthesis and investigation of tetragonal $Co^{2+}(Mn^{3+}, Fe^{3+})O_4$ particles with a normal spinel configuration. Firstly, the normal spinel configuration would allow us to fix the Co^{2+} ion concentration, so that there is no trade-off condition with varying the JT and ME elements. Secondly, to address the low magnetic moment of Cu^{2+}, we propose the use of other JT elements, Mn^{3+} and/or Cr^{2+}, which have higher magnetic moments ($4\mu_B$).

Concerning coercivity analysis, we believe that the magnetic viscosity parameter considered in the global model is an important factor to be considered in the study of magnetization reversal in tetragonal ferrite particles. By considering the magnetic viscosity and the thermal activation effects, we were able to explain the coercivity anomalies observed at low temperature. The global model analysis suggested that the exchange-coupled grains are what causes coercivity reduction at sufficiently low temperatures. What if the particles are not exchange-coupled? How would this affect the coercivity? These fundamental questions spark our interest in the development of tetragonal ferrite particles which are exchange-decoupled. To synthesize non-interacting ferrite particles, one can utilize a core-shell structure by for example, the use of silica coating around the particles. We propose silica coating because there are a number of literature reports [77][78][79] regarding the preparation of silica-coated iron oxide nanoparticles, mainly using a method called the Stöber process [80]. To investigate exchange-decoupled grains system, optimization of fabrication method will be very challenging and crucial because one needs to optimize, not only the lattice distortion and magnetic anisotropy, but also the targeted microstructure (silica-coated structure).

Bibliography

[1]   B. Schulz and K. Baberschke, "Crossover from in-plane to perpendicular magnetization in ultrathin Ni/Cu(001) films," *Phys. Rev. B*, vol. 50, no. 18, pp. 13467–13471, Nov. 1994.

[2]   R. Thamankar, A. Ostroukhova, and F. O. Schumann, "Spin-reorientation transition in FexNi1-xalloy films," *Phys. Rev. B*, vol. 66, no. 13, pp. 1344141–1344148, 2002.

[3]   T. Niizeki *et al.*, "Extraordinarily large perpendicular magnetic anisotropy in epitaxially strained cobalt-ferrite $Co_xFe_{3-x}O_4(001)$ ($x = 0.75, 1.0$) thin films," *Appl. Phys. Lett.*, vol. 103, no. 162407, pp. 1–5, 2013.

[4]   T. Tainosho, J. Inoue, S. Sharmin, and H. Yanagihara, "Large Negative Uniaxial Magnetic Anisotropy of Cobalt Ferrite Thin Films," *Dig. TMRC 2017 28th Magn. Rec. Conf.*, pp. 133–134, 2017. [manuscript submitted]

[5]   J. Inoue, T. Niizeki, H. Yanagihara, H. Itoh, and E. Kita, "Electron theory of perpendicular magnetic anisotropy of Co-ferrite thin films," *AIP Adv.*, vol. 4, no. 027111, pp. 2014–2017, 2014.

[6]   S. Chikazumi, *Physics of Ferromagnetism*. Oxford, New York: Oxford University Press, 1997.

[7]   H. Kronmüller, K.-D. Durst, S. Hock, and G. Martinek, "MICROMAGNETIC ANALYSIS OF THE MAGNETIC HARDENING MECHANISMS IN RE-Fe-B MAGNETS," *Le J. Phys. Colloq.*, vol. 49, no. C8, pp. 623–628, Dec. 1988.

[8]   D. Givord, P. Tenaud, and T. Viadieu, "Coercivity mechanisms in ferrite and rare earth transition metal sintered magnets ($SmCo_5$, Nd-Fe-B)," *IEEE Trans. Magn.*, vol. 24, no. 2, pp. 1921–1923, Mar. 1988.

[9]   L. Néel, "Antiferromagnetism and ferrimagnetism," *Proc. Phys. Soc. Sect. A*, vol. 65, no. 11, pp. 869–885, Nov. 1952.

[10]   E. W. GORTER, "Magnetization in Ferrites: Saturation Magnetization of Ferrites with Spinel Structure," *Nature*, vol. 165, no. 4203, pp. 798–800, May 1950.

[11]   E. W. Gorter, "Saturation Magnetization and Crystal Chemistry Of Ferrimagnetic Oxides," *Philips Res. Reports*, vol. 9, pp. 321–365, 1954.

[12]   G. A. Sawatzky, F. VAN DER Woude, and A. H. Morrish, "Cation Distributions in Octahedral and Tetrahedral Sites of the Ferrimagnetic Spinel $CoFe_2O_4$," *J. Appl. Phys.*, vol. 39, no. 2, pp. 1204–1205, Feb. 1968.

[13]   M. R. De Guire, R. C. O'Handley, and G. Kalonji, "The cooling rate dependence of cation distributions in $CoFe_2O_4$," *J. Appl. Phys.*, vol. 65, no. 8, pp. 3167–3172, Apr. 1989.

[14]   Y. Yafet and C. Kittel, "Antiferromagnetic Arrangements in Ferrites," *Phys. Rev.*, vol. 87, no. 2, pp. 290–294, Jul. 1952.

[15]   G. T. Rado and H. Suhl, *Magnetism. Vol. 1, Magnetic ions in insulators, their interactions, resonances and optical properties*. Academic Press, 1963.

[16]   J. F. Dillon, S. Geschwind, and V. Jaccarino, "Ferrimagnetic Resonance in Single Crystals of Manganese Ferrite," *Phys. Rev.*, vol. 100, no. 2, pp. 750–752, Oct. 1955.

[17]   L. R. Bickford, "Ferromagnetic Resonance Absorption in Magnetite Single Crystals," *Phys. Rev.*, vol. 78, no. 4, pp. 449–457, May 1950.

[18]   H. Shenker, "Magnetic anisotropy of cobalt ferrite ($Co_{1.01}Fe_{2.00}O_{3.62}$) and nickel cobalt ferrite ($Ni_{0.72}Fe_{0.20}Co_{0.08}Fe_2O_4$)," *Phys. Rev.*, vol. 107, no. 5, pp. 1246–1249, 1957.

[19]   J. C. Slonczewski, "Origin of magnetic anisotropy in cobalt-substituted magnetite," *Phys. Rev.*, vol. 110, no. 6, pp. 1341–1348, 1958.

[20]   M. Tachiki, "Origin of the Magnetic Anisotropy Energy of Cobalt Ferrite," *Prog. Theor. Phys.*, vol. 23, no. 6, pp. 1055–1072, 1960.

[21]   V. K. Chakradhary, A. Ansari, and M. J. Akhtar, "Design, synthesis, and testing of high coercivity

cobalt doped nickel ferrite nanoparticles for magnetic applications," *J. Magn. Magn. Mater.*, vol. 469, pp. 674–680, Jan. 2019.

[22] L. Néel, "Anisotropie magnétique superficielle et surstructures d'orientation," *J. Phys. le Radium*, vol. 15, no. 4, pp. 225–239, Apr. 1954.

[23] L. Néel, "Directional Order and Diffusion Aftereffect," *J. Appl. Phys.*, vol. 30, no. 4, pp. S3–S8, Apr. 1959.

[24] R. M. Bozorth, E. F. Tilden, and A. J. Williams, "Anisotropy and magnetostriction of some ferrites," *Phys. Rev.*, vol. 99, no. 6, pp. 1788–1798, 1955.

[25] S. Iida, H. Sekizawa, and Y. Aiyama, "Uniaxial Anisotropy in Iron-Cobalt Ferrites," *J. Phys. Soc. Japan*, vol. 13, no. 1, pp. 58–71, Jan. 1958.

[26] J. D. Dunitz and L. E. Orgel, "Electronic properties of transition-metal oxides—I: Distortions from cubic symmetry," *J. Phys. Chem. Solids*, vol. 3, no. 1–2, pp. 20–29, Jan. 1957.

[27] H. Ohnishi and T. Teranishi, *Jisei Buturi no Shinpo (in Japanese)*. Agune, 1964.

[28] S. Miyahara, K. Muramori, and N. Tokuda, "Tetragonal Distortion in Copper Manganite-Chromite System," *J. Phys. Soc. Japan*, vol. 16, no. 7, pp. 1490–1490, Jul. 1961.

[29] X. X. Tang, A. Manthiram, and J. B. Goodenough, "Copper ferrite revisited," *J. Solid State Chem.*, vol. 79, no. 2, pp. 250–262, Apr. 1989.

[30] I. Onyszkiewicz, N. T. Malafaev, A. A. Murakhovskii, and J. Pietrzak, "Magnetic and FMR Investigation of the Structural Phase Transition in Cu-Ferrite with Cooperative Jahn-Teller Effect," *Phys. status solidi*, vol. 73, no. 2, pp. K243–K247, Oct. 1982.

[31] L. Weil, F. Bertaut, and L. Bochirol, "Propriétés magnétiques et structure de la phase quadratique du ferrite de cuivre," *J. Phys. le Radium*, vol. 11, no. 5, pp. 208–212, May 1950.

[32] E. F. Bertaut, "Sur quelques progrès récents dans la cristallographie des spinelles, en particulier des ferrites," *J. Phys. le Radium*, vol. 12, no. 3, pp. 252–255, Mar. 1951.

[33] H. Ohnishi, T. Teranishi, and S. Miyahara, "On the Transition Temperature of Copper Ferrite," *J. Phys. Soc. Japan*, vol. 14, no. 1, pp. 106–106, Jan. 1959.

[34] S. Miyahara and H. Ohnishi, "Cation Arrangement and Magnetic Properties of Copper Ferrite-Chromite Series," *J. Phys. Soc. Japan*, vol. 11, no. 12, pp. 1296–1297, 1956.

[35] H. Ohnishi and T. Teranishi, "Crystal Distortion in Copper Ferrite-Chromite Series," *J. Phys. Soc. Japan*, vol. 16, no. 1, pp. 35–43, 1961.

[36] A. Lisfi *et al.*, "Reorientation of magnetic anisotropy in epitaxial cobalt ferrite thin films," *Phys. Rev. B*, vol. 76, no. 5, p. 054405, 2007.

[37] E. C. Stoner and E. P. Wohlfarth, "A Mechanism of Magnetic Hysteresis in Heterogeneous Alloys," *Philos. Trans. R. Soc. A Math. Phys. Eng. Sci.*, vol. 240, no. 826, pp. 599–642, May 1948.

[38] J. Hu, X. C. Kou, and H. Kronmüller, "The low-temperature dependence of coercivity in NdFeB magnets," *Phys. Status Solidi*, vol. 188, no. 2, pp. 807–811, 1995.

[39] F. Kools, "Factors Governing the Coercivity of Sintered Anisotropic M Type Ferrite," *J. Phys. Colloq.*, vol. C6, no. C6, pp. 349–354, Sep. 1985.

[40] M. Sagawa and S. Hirosawa, "COERCIVITY AND MICROSTRUCTURE OF R-Fe-B SINTERED PERMANENT MAGNETS," *J. Phys. Colloq.*, vol. 49, no. C8, pp. 617–622, Dec. 1988.

[41] H. Kronmüller, "Theory of Nucleation Fields in Inhomogeneous Ferromagnets," *Phys. status solidi*, vol. 144, no. 1, pp. 385–396, Nov. 1987.

[42] H. Kronmüller, K. D. Durst, and M. Sagawa, "Analysis of the magnetic hardening mechanism in RE-FeB permanent magnets," *J. Magn. Magn. Mater.*, vol. 74, no. 3, pp. 291–302, 1988.

[43] V. T. M. S. Barthem, D. Givord, M. F. Rossignol, and P. Tenaud, "An approach to coercivity relating coercive field and activation volume," *Phys. B Condens. Matter*, vol. 319, no. 1–4, pp. 127–132, 2002.

[44] D. Givord, M. Rossignol, and D. Taylor, "Coercivity mechanisms in hard magnetic materials," *J. Phys. IV Fr.*, vol. 02, no. C3, pp. 95–104, 1992.

[45] R. Street and J. C. Woolley, "A Study of Magnetic Viscosity," *Proc. Phys. Soc. Sect. A*, vol. 62, no. 9, pp. 562–572, Sep. 1949.

[46] R. Street and S. D. Brown, "Magnetic viscosity, fluctuation fields, and activation energies (invited)," *J. Appl. Phys.*, vol. 76, no. 10, pp. 6386–6390, 1994.

[47] L. Néel, "Théorie du traînage magnétique de diffusion," *J. Phys. le Radium*, vol. 13, no. 5, pp. 249–264, May 1952.

[48] P. Gaunt, "Magnetic viscosity and thermal activation energy," *J. Appl. Phys.*, vol. 59, no. 12, pp. 4129–4132, Jun. 1986.

[49] IUPAC, "coprecipitation," in *Compendium of Chemical Terminology*, 2nd ed., A. D. McNaught and A. Wilkinson, Eds. Blackwell Scientific Publications, Oxford, 1997.

[50] T. Sugimoto and E. Matijević, "Formation of uniform spherical magnetite particles by crystallization from ferrous hydroxide gels," *J. Colloid Interface Sci.*, vol. 74, no. 1, pp. 227–243, Mar. 1980.

[51] R. T. Olsson, G. Salazar-Alvarez, M. S. Hedenqvist, U. W. Gedde, F. Lindberg, and S. J. Savage, "Controlled synthesis of near-stoichiometric cobalt ferrite nanoparticles," *Chem. Mater.*, vol. 17, no. 20, pp. 5109–5118, 2005.

[52] F. Huixia, C. Baiyi, Z. Deyi, Z. Jianqiang, and T. Lin, "Preparation and characterization of the cobalt ferrite nano-particles by reverse coprecipitation," *J. Magn. Magn. Mater.*, vol. 356, pp. 68–72, Apr. 2014.

[53] M. A. Augustyniak and M. Krupski, "The temperature dependence of the pressure switching of Jahn–Teller deformation in the deuterated ammonium copper Tutton salt," *Chem. Phys. Lett.*, vol. 311, no. 3–4, pp. 126–130, Sep. 1999.

[54] S. Kimura *et al.*, "Effect of heat treatment on Jahn-Teller distortion and magnetization in Cu ferrite nanoparticles," in *Thermochimica Acta*, 2012, vol. 532, pp. 119–122.

[55] N. N. Greenwood and T. C. Gibb, *Mössbauer Spectroscopy*. Springer Netherlands, 1971.

[56] C. E. Violet and D. N. Pipkorn, "Mössbauer Line Positions and Hyperfine Interactions in α Iron," *J. Appl. Phys.*, vol. 42, no. 11, pp. 4339–4342, Oct. 1971.

[57] B. D. Cullity, *Introduction to Magnetic Materials*. Reading MA, USA: Addison-Wesley, 1972.

[58] D. Paige, S. Hoon, B. Tanner, and K. O'Grady, "High precision torque hysteresis measurements on fine particle systems," *IEEE Trans. Magn.*, vol. 20, no. 5, pp. 1852–1854, Sep. 1984.

[59] M. Suekane, M. Miyamura, T. Shimatsu, and M. Takahashi, "Study on the Magnetic Microstructures for CoNiPt Thin Film Media by Rotational Hysteresis Loss Analysis," *J. Magn. Soc. Japan*, vol. 16, no. 4, pp. 655–660, Aug. 1992.

[60] M. Igarashi, T. Kambe, K. Yoshida, Y. Hosoe, and Y. Sugita, "A method of measuring anisotropy field of polycrystalline thin-film media," *J. Appl. Phys.*, vol. 85, no. 8, pp. 4720–4722, 1999.

[61] Z. Klencsár, E. Kuzmann, and A. Vértes, "User-friendly software for Mössbauer spectrum analysis," *J. Radioanal. Nucl. Chem.*, vol. 210, no. 1, pp. 105–118, 1996.

[62] J. S. J.Janicki, J. Pietrzak, A.Porebska, "Mossbauer study of copper ferrite," *Phys. Status Solidi*, vol. 95, pp. 95–98, 1982.

[63] J. Chappert and R. B. Frankel, "Mössbauer Study of Ferrimagnetic Ordering in Nickel Ferrite and Chromium-Substituted Nickel Ferrite," *Phys. Rev. Lett.*, vol. 19, no. 10, pp. 570–572, Sep. 1967.

[64] A. Malats i Riera, G. Pourroy, and P. Poix, "High coercivity of a cobalt doped magnetite $Fe_{2.38}Co_{0.62}O_4$," *J. Magn. Magn. Mater.*, vol. 134, no. 1, pp. 195–198, May 1994.

[65] D. H. Han, J. P. Wang, and H. L. Luo, "The induced effective uniaxial anisotropy of Mn and Co volume-doped acicular γ-Fe_2O_3 particles," *J. Magn. Magn. Mater.*, vol. 145, no. 1–2, pp. 199–204, Mar.

1995.

[66] K. I. Arai and N. Tsuya, "Observation of Magnetostriction in Cu Ferrite Single Crystals," *Phys. status solidi*, vol. 66, no. 2, pp. 547–552, Dec. 1974.

[67] N. T. Malafaev, A. A. Murakhovskii, J. A. Popkov, and I. Onyszkiewicz, "A study on magnetocrystalline anisotropy in tetragonal copper ferrite," *J. Magn. Magn. Mater.*, vol. 89, no. 1–2, pp. 8–12, 1990.

[68] M. D. Sturge, E. M. Gyorgy, R. C. Lecraw, and J. P. Remeika, "Magnetic behavior of cobalt in garnets. II. Magnetocrystalline anisotropy and ferrimagnetic resonance of cobalt-doped yttrium iron garnet," *Phys. Rev.*, vol. 180, no. 2, pp. 413–423, Apr. 1969.

[69] Y. Suzuki, G. Hu, R. B. B. van Dover, and R. J. J. Cava, "Magnetic anisotropy of epitaxial cobalt ferrite thin films," *J. Magn. Magn. Mater.*, vol. 191, no. 1–2, pp. 1–8, Jan. 1999.

[70] R. C. O'Handley and S.-W. Sun, "Strained layers and magnetoelastic coupling," *J. Magn. Magn. Mater.*, vol. 104–107, pp. 1717–1720, Feb. 1992.

[71] G. Bochi, O. Song, and R. C. O'Handley, "Surface magnetoelastic coupling coefficients of single-crystal fcc Co thin films," *Phys. Rev. B*, vol. 50, no. 3, pp. 2043–2046, Jul. 1994.

[72] U. Gradmann, "Surface magnetism," *J. Magn. Magn. Mater.*, vol. 100, no. 1–3, pp. 481–496, Nov. 1991.

[73] J. M. D. Coey, *Rare-earth iron permanent magnets*. Clarendon Press, 1996.

[74] E. F. Westrum and F. Gronvold, "Magnetite Heat capacity and thermodynamic properties from 5 to 350 K, low temperature transition," *J. Chem. Thermodyn.*, vol. 1, pp. 543–557, 1969.

[75] Y. Otani, J. M. D. Coey, B. Barbara, H. Miyajima, S. Chikazumi, and M. Uehara, "Anomalous demagnetization process at very low temperature in Nd-Fe-B magnets," *J. Appl. Phys.*, vol. 67, no. 9, pp. 4619–4621, 1990.

[76] D. S. Neznakhin, A. S. Bolyachkin, A. S. Volegov, P. E. Markin, S. V. Andreev, and N. V. Kudrevatykh, "Magnetization jumps in nanostructured Nd-Fe-B alloy at low temperatures," *J. Magn. Magn. Mater.*, vol. 377, pp. 477–479, 2015.

[77] Q. Dai *et al.*, "Monodisperse cobalt ferrite nanomagnets with uniform silica coatings," *Langmuir*, vol. 26, no. 22, pp. 17546–17551, Nov. 2010.

[78] Z. Sharafi, B. Bakhshi, J. Javidi, and S. Adrangi, "Synthesis of Silica-coated Iron Oxide Nanoparticles: Preventing Aggregation without Using Additives or Seed Pretreatment.," *Iran. J. Pharm. Res. IJPR*, vol. 17, no. 1, pp. 386–395, 2018.

[79] L. Zhao, H. Yang, Y. Cui, X. Zhao, and S. Feng, "Study of preparation and magnetic properties of silica-coated cobalt ferrite nanocomposites," *J. Mater. Sci.*, vol. 42, no. 11, pp. 4110–4114, May 2007.

[80] W. Stober, A. Fink, and D. Ernst Bohn, "Controlled Growth of Monodisperse Silica Spheres in the Micron Size Range 1," 1968.

Annex 1: $M(H_{app})$ curves analysis

One of the main challenges in characterizing polycrystalline and/or powdered samples is to determine the magnetic anisotropy of the sample. The problem arises as the easy axis of magnetization of different grains point in different directions. To simplify the problem, we applied a stochastic method and developed a model to estimate the intrinsic magnetic properties (spontaneous magnetization M_s and magnetic anisotropy energy K). In the analysis, we calculate the applied field H_{app} dependence of the magnetization M and compared the calculated results with experimental MH curves taken at different temperatures. The following fundamental hypotheses are assumed:

1. Coherent rotation of a classical single domain of magnetic moment M having (first-order) uniaxial anisotropy energy K_1
2. We consider only moment rotation and disregard any domain wall processes and the demagnetizing field is neglected.
3. We assume a certain texture parameter n described by a distribution function $pK(\theta) = \frac{n+1}{2\pi} cos^n(\theta)$.

The model description of the $M(H_{app})$ curves analysis is divided into two. First, the texture (grain orientation) parameter n is defined using a distribution function. Using the probability function of the grain distribution for n in a given applied field H_{app}, the magnetization M calculation follows by analyzing the energy minimum function of the total free energy of the system. The total free energy of the system is first treated with a classical approach by summing the magnetic anisotropy and the dipolar (Zeeman) energies. To refine the calculation results with the experimental curves, we then add a phenomenological exchange energy (similar to the Ising model) to the total energy of the system.

1.1 Texture analysis

The texture parameter n is defined using the distribution function $pK(\theta) = \frac{n+1}{2\pi} cos^n(\theta)$ where $n = 0$ for non-textured (isotropic) samples and $n = 10^5$ for highly textured (aligned) samples. Consider a grain the axis of which makes angles θ and φ with respect to the texture axis (**Fig. A1-1** (a)). The cosine directions of the easy axis in a reference frame defined by the texture axis (TexZ) and the applied field (B) are:

$\alpha_1 = sin\theta cos\varphi$
$\beta_1 = sin\theta sin\varphi$
$\gamma_1 = cos\theta$

(A1.1).

Those associated with the applied magnetic field are:
   field (B) are:

$\alpha_2 = sin\theta_{TexZ}$
$\beta_2 = 0$
$\gamma_2 = cos\theta_{TexZ}$

(A1.2).
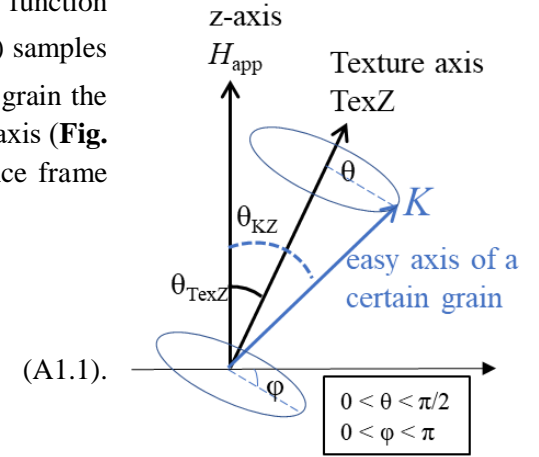
Fig. A1-1 (a) Diagram of the texture axis with respect to the anisotropy and applied field.

Next, we project the angles θ, φ and θ_{TexZ} with respect to the applied field (z-axis). The cosine of the associated easy axis with respect to the applied field is given as:

$$cos\theta_{KZ} = sin\theta cos\varphi sin\theta_{TexZ} + cos\theta cos\theta_{TexZ}$$

(A1.3).

For a given value of θ_{KZ}, there are various θ involved, each contribution makes a distribution function proportional to the texture $pK(\theta)$. By summing and normalizing these distribution functions, we derive the probability distribution function of the texture, $ppKZ(\theta_{KZ})$. This probability function estimates the number of grains affected by the applied field as described in the next step.

1.2 Calculation of $M(H_{app})$

The direction of magnetization is defined by the competing torques between the applied field and the magnetization energy K. The magnetization of the grain M rotates in the plane defined by the field, H_{app} and the easy axis, K (which makes the angle θ_{KZ} with respect to H_{app}, see **Fig. A1-1** (b). Note that the angle φ in the first part is no longer relevant to obtain the projection of M along H. The cosine directions of the anisotropy axis are:

$$\alpha K_1 = \cos\theta_K;$$
$$\alpha K_2 = \sin\theta_K$$

(A1.4).

And those of the magnetization are:

$$\alpha M_1 = \cos\theta_M;$$
$$\alpha M_2 = \sin\theta_M \tag{A1.5}.$$

Fig. A1-1 (b) Rotation of M within H_{app} and K axes.

For each K_1 value, the energy minimum condition of θ_{KZ} is determined and from the probability distribution function $ppKZ(\theta_{KZ})$ described above, the calculation of magnetization follows as

$$M(H_{app}) = M_s ppKZ(\theta_{KZ})$$

1.3 Calculation results

Using the *classical approach*, the total free energy of the system per unit volume E_{tot} is given by

$$E_{tot} = K_1\sin^2\theta - \mu_0 M_s H_{app}\cos\varphi_1$$

(A1.6)

where θ is the angle of the magnetic moment with respect to the easy axis and φ_1 is the angle between the magnetization and the applied field given as

$$\varphi_1 = \theta_{KZ} - \theta$$

(A1.7)

Figure A1-2 (a) shows the 10 K experimental curve and the calculated curves from the $M(H_{app})$ analysis, with texture ($n = 1$) and without texture ($n = 0$). The calculated results suggest that the particles are textured. However, by measuring $M(H)$ for different applied field orientations, it was demonstrated that the grain orientation is fully isotropic ($n = 0$). In such a case, one expects that the ratio of the remnant magnetization M_r to M_s is equal to 0.5, in contrast with the $M_r/M_s > 0.5$ that was systematically found. This can be explained either by a highly textured grain orientation, or by intergranular exchange interactions. Since we have confirmed that $n = 0$, the remaining possibility is the latter.

To describe the remanence enhancement of the isotropic particles, we added a third term into the classical model by assuming a phenomenological exchange field proportional to M_s,

$$H_{exch} = w_{exch} M_s$$

where w_{exch} is the exchange field constant. The total free energy in eq. (A1.6) now becomes

$$E_{tot} = K_1\sin^2\theta - \mu_0 M_s(H_{app} + H_{exch})\cos\varphi_1$$

(A1.6)

The calculation is revised by using the values $n = 0$, and $w_{exch} = 2.5$. **Fig. A1-2 (b)** shows the renewed calculated results with the added exchange field factor. Adding the phenomenological exchange field permitted an excellent description of the experimental data. The analysis was performed with the $T = 10 – 300$ K curves and the fitting parameters are plotted as a function of temperature (**Fig. A1-2** (c)). While M_s is almost temperature independent, K_1 decreases with increasing temperature, which agrees with the expected behavior. At 10 K, the anisotropy field was determined to be 2.8 M A/m and the value decreases to 1.9 M A/m at 300 K. The room temperature value is in fair agreement with the value estimated from rotational hysteresis measurement, $H_k = 1.6$ MA/m.
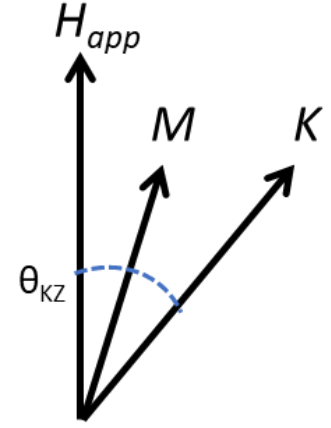
To explain exchange interactions between nanograins, we performed high-resolution TEM imaging on the sample. **Fig. A1-3** (a) shows several individual primary nanograins of 20 – 100 nm in size which are closely packed. Crystal lattice planes observed in the high-resolution TEM image shown in **Fig. A1-3** (b) showed that these nanograins consist of highly crystalline single crystals. In **Fig. A1-3** (c), one can clearly see that the nanograins are connected through a thin amorphous layer of ~1 nm in thickness, which could explain the observed remanence enhancement.
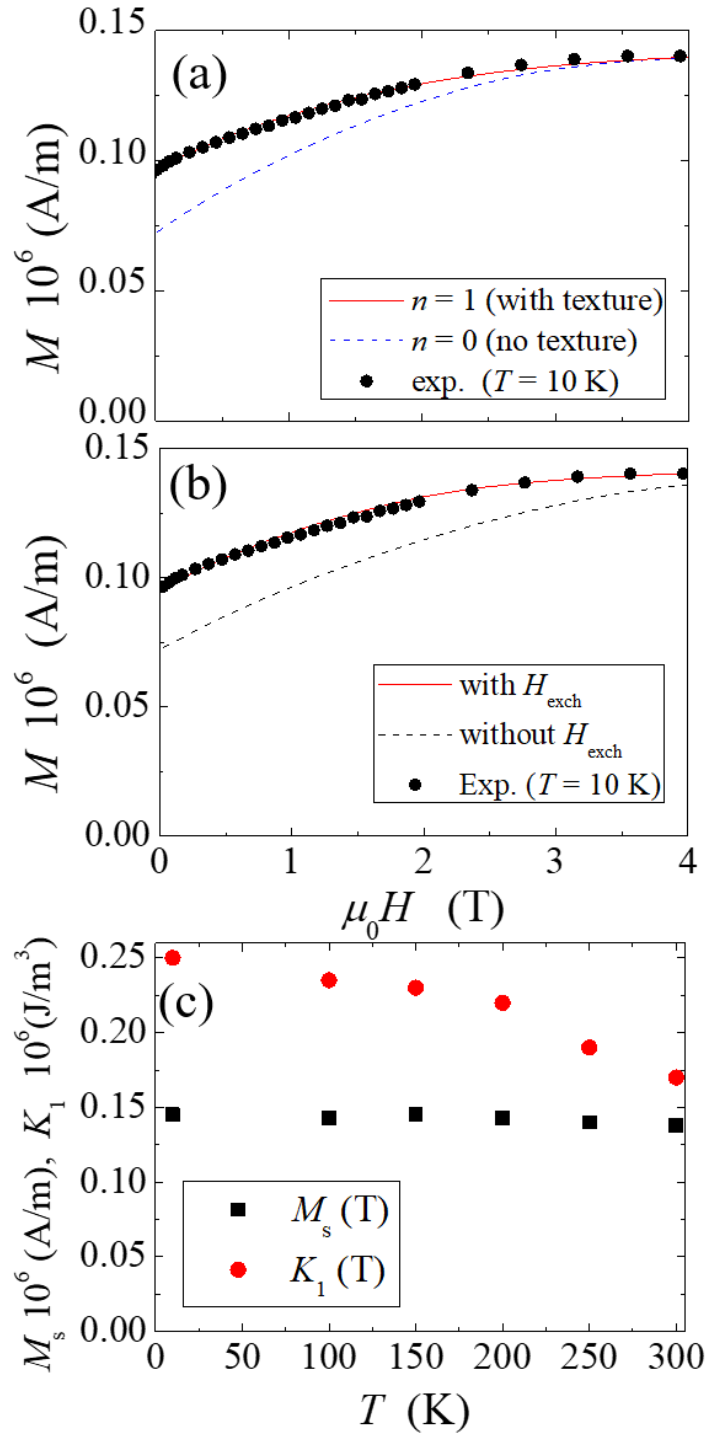

Fig. A1-2 The calculated $M(H_{app})$ curves with and without the parameters (a) n and (b) H_{exch}. (c) The evaluated $M_s(T)$ and $K_1(T)$ parameters.
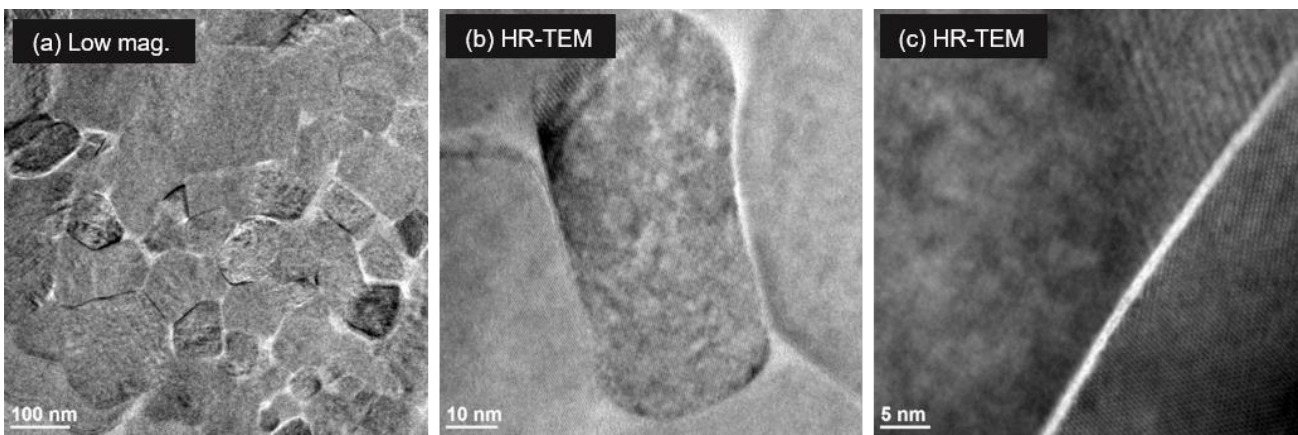
Fig. A1-3. TEM images of tetragonal $Cu_{0.9}Co_{0.1}Fe_2O_4$ particles. (a) An assembly of individual nanograins (50 – 100 nm), (b) a single nanograin and parts of adjacent nanograins, (c) an amorphous 1 nm thick layer between nanograins.

Annex 2: Estimation of the specific heat of (Cu,Co)-ferrite

For reversal in a single grain of volume V_{grain}, the conversion of magnetic energy (in Joules) into thermal energy can be expressed approximately by eq. (7.3)

$$2\mu_0 M_s H_c V_{grain} = V_{grain} \int_{T_{init}}^{T_{fin}} C_V(T)dT$$

(7.3)

To estimate the rise in temperature via heat dissipation (ΔT) from the Zeeman energy, we used the following protocol to estimate the specific heat of the spinel $(Cu,Co)Fe_2O_4$ particles. We assume that the specific heat at low temperature is similar to that of magnetite.

In general, the specific heat of magnetic materials is the summation of the electronic C_e, lattice C_l and magnetic C_m terms and can be written as

$$C_p = C_e + C_l + C_m$$

Considering the temperature dependency of each terms, $C_p(T)$ is expressed as

$$C_p(T) = \gamma T + \beta T^3 + \alpha T^m$$

where α, β, and γ are the specific heat coefficients respective to each term. If the material is a non-magnetic insulator, the term C_e and C_m can be disregarded so that the value of the Debye temperature can be estimated by fitting the data to $C_p(T) = \beta T^3$. For non-magnetic conductors, the term C_m can be disregarded and the values of γ and β are estimated from the plot of $C_p/2$ versus T^2, where the intercept with the y-axis represents the electronic specific heat coefficient γ and the slope is taken as β. For magnetic materials, the value of m depends on the magnetic state of the considered sample; e.g. for ferromagnetic magnetite (Fe_3O_4) and most spinel ferrites, the value of m is 3/2.

From the experimental data measured at low temperature (5–50 K) by Westrum et al. [74], the volume specific heat of magnetite at low temperature can be estimated by fitting the data to

$$C_v(T) = \beta T^3 + \alpha T^{\frac{3}{2}}$$

(A2.1)

Since the goal is to estimate the value of ΔT in the integral in eq. (7.3), the experimental data were approximated to a simple polynomial function to simplify the integral (see **Fig. A2**)

$$C_v(T) = 8.6T^{2.7}$$

(A2.2)

The temperature dependency is close to T^3, suggesting that the lattice contribution (C_l) is the main contribution of the specific heat. Substituting the following expression into the integrals in eq. (7.3), one can estimate the value of T_{fin} by solving the integral equation.
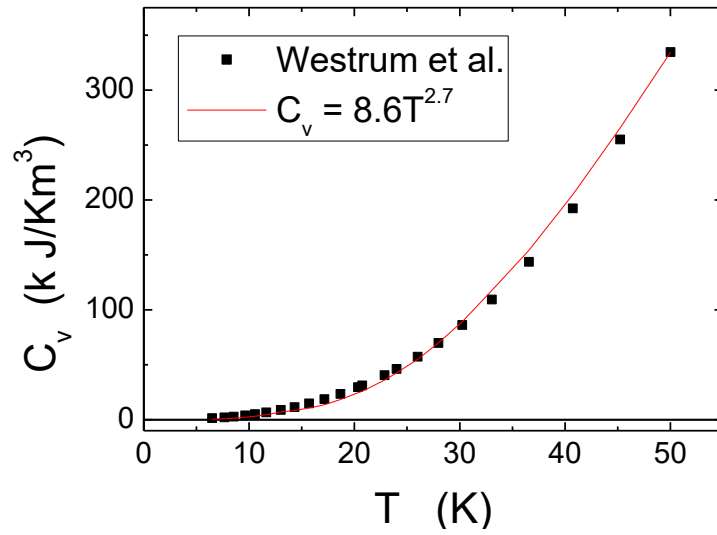
Fig. A2. The specific heat (per unit volume) plotted as a function of temperature. The black squares represent the experimental data measured by Westrum et al.

List of related presentations and publications

International conferences

1. <u>H. Latiff</u>, M. Kishimoto, J. Inoue, E. Kita, H. Yanagihara, *"Jahn-Teller distortion and magnetoelastic coupling in tetragonal (Cu,Co)Fe$_2$O$_4$ particles",* International Conference on Magnetism 2018, San Francisco, July 2018. (Oral)

2. <u>H. Latiff</u>, T. Devillers, H. Yanagihara, N. M. Dempsey, and D. Givord, *"Anisotropy and coercivity analysis in tetragonal (Cu,Co)Fe$_2$O$_4$ particles",* IEEE International Magnetic Conference INTERMAG 2018, Singapore, April 2018. (Oral)

3. <u>H. Latiff</u>, M. Kishimoto, S. Sharmin, E. Kita, H. Yanagihara, *"Tetragonalization of (Cu,Co)Fe$_2$O$_4$ particles via the Jahn-Teller effect induced by Cu^{2+} ions",* IEEE International Magnetic Conference INTERMAG 2017, Dublin, April 2017. (Poster)

4. <u>H. Latiff</u>, M. Kishimoto, S. Sharmin, E. Kita, H. Yanagihara, "*Synthesis and physical properties of single phase cubic and tetragonal CuFe$_2$O$_4$ particles*", The 9th International Conference on Fine Particle Magnetism (ICFPM 2016), Maryland, June 2016. (Oral)

Publications

1. <u>H. Latiff</u>, M. Kishimoto, J. Inoue, E. Kita, H. Yanagihara, T. Devillers, "*Strain-induced magnetic anisotropy via the Jahn-Teller effect and the magnetoelastic coupling of tetragonally distorted (Cu,Co)Fe$_2$O$_4$ particles*", submitted, 2018.

2. <u>H. Latiff</u>, M. Kishimoto, S. Sharmin, E. Kita, H. Yanagihara, "*Enhanced anisotropy in tetragonalized (Cu,Co)Fe$_2$O$_4$ particles via the Jahn-Teller effect of Cu^{2+} ions*", *IEEE Transactions on Magnetics*, 53 (11), 9402304, 2017.

3. <u>H. Latiff</u>, M. Kishimoto, S. Sharmin, E. Kita, H. Yanagihara, "*Effect of copper substitution on Fe$_3$O$_4$ particles prepared via coprecipitation and flux methods*", *IEEE Transactions on Magnetics*, 53 (1), 9400104, 2017.